



저작자표시-비영리-변경금지 2.0 대한민국

이용자는 아래의 조건을 따르는 경우에 한하여 자유롭게

- 이 저작물을 복제, 배포, 전송, 전시, 공연 및 방송할 수 있습니다.

다음과 같은 조건을 따라야 합니다:



저작자표시. 귀하는 원저작자를 표시하여야 합니다.



비영리. 귀하는 이 저작물을 영리 목적으로 이용할 수 없습니다.



변경금지. 귀하는 이 저작물을 개작, 변형 또는 가공할 수 없습니다.

- 귀하는, 이 저작물의 재이용이나 배포의 경우, 이 저작물에 적용된 이용허락조건을 명확하게 나타내어야 합니다.
- 저작권자로부터 별도의 허가를 받으면 이러한 조건들은 적용되지 않습니다.

저작권법에 따른 이용자의 권리는 위의 내용에 의하여 영향을 받지 않습니다.

이것은 [이용허락규약\(Legal Code\)](#)을 이해하기 쉽게 요약한 것입니다.

[Disclaimer](#)

이학박사학위논문

**Turbulence Coherent Structures and Scalar  
Dispersion over Heated Urban Surfaces**

가열된 도시 표면 위에서의 난류 고유 구조와  
스칼라 분산

2013년 8월

서울대학교 대학원

지구환경과학부

박 승 부

**Turbulence Coherent Structures and Scalar  
Dispersion over Heated Urban Surfaces**

**가열된 도시 표면 위에서의 난류 고유 구조와  
스칼라 분산**

지도교수 백 종 진

이 논문을 이학박사 학위논문으로 제출함

2013년 4월

서울대학교 대학원

지구환경과학부

박 승 부

박승부의 이학박사 학위논문을 인준함

2013년 6월

위 원 장 \_\_\_\_\_ (인)

부위원장 \_\_\_\_\_ (인)

위 원 \_\_\_\_\_ (인)

위 원 \_\_\_\_\_ (인)

위 원 \_\_\_\_\_ (인)

# **Turbulence Coherent Structures and Scalar Dispersion over Heated Urban Surfaces**

**By  
Seung-Bu Park**

**A Dissertation Submitted to the Faculty of the Graduate  
School of Seoul National University in Partial Fulfillment  
of the Requirements for the Degree of Doctor of  
Philosophy**

**August 2013**

**Advisory Committee:**

**Professor In-Sik Kang, Chair  
Professor Jong-Jin Baik, Advisor  
Professor Yign Noh  
Professor Rokjin Park  
Doctor Young-San Park**

## **Abstract**

Turbulent flow and scalar dispersion over heated urban surfaces are numerically investigated using the parallelized large-eddy simulation model (PALM). To investigate thermal effects of urban surface heating on turbulent flow and scalar dispersion, a method that calculates heat fluxes at building wall surfaces based on the Monin-Obukhov (MO) similarity is developed and validated.

Thermal effects on turbulent flow and dispersion in and above an idealized street canyon with a street aspect ratio of one are examined when each of upwind building wall, street bottom, and downwind building wall is heated. Compared with the neutral (no heating) case, the upwind building wall or street bottom heating strengthens a primary vortex in the street canyon, while the downwind building wall heating induces a shrunken primary vortex and a winding flow between the vortex and the downwind building wall. Heating also induces higher turbulent kinetic energy and stronger turbulent fluxes at the rooftop height. In the neutral case, turbulent eddies generated by shear instability dominate mixing at the rooftop height and appear as band-shaped perturbations in the time–space plots of instantaneous turbulent momentum and scalar fluxes. In all the heating cases, buoyancy-generated turbulent eddies as well as shear-

generated turbulent eddies contribute to vertical turbulent momentum and scalar fluxes and they appear as band-shaped and lump-shaped perturbations at the rooftop height. A quadrant analysis shows that sweeps are less frequent but contribute more to turbulent momentum flux than ejections at the rooftop height in the neutral and upwind building wall heating cases. In contrast, in the street bottom and downwind building wall heating cases, the frequency of sweeps is similar to that of ejections and the contribution of ejections to turbulent momentum flux is comparable to that of sweeps.

Turbulent flow and scalar dispersion over an idealized building array are investigated using the LES model. Two cases (no heating and bottom heating) are simulated and compared to each other. Above the building array, streaky structures of low-speed regions appear and ejections on the regions play a dominant role in transporting momentum downward. When the bottom is heated, plume-shaped structures appear with the streaky structures and the magnitude of vertical turbulent momentum flux, averaged over the low-speed regions, increases. Elliptical structures of negative streamwise velocity perturbation and vortical structures similar to hairpin vortices appear in the conditionally averaged fields and the vortical structure above the bottom-heated building array expands in the vertical direction. At the rooftop height and in the intersections, sweeps, induced by downward extending high-speed regions, are dominant and they

transport momentum into the building array. Below the rooftop height, momentum is actively transported by the spanwise turbulent motions, especially from the intersections to the street canyons. The spanwise turbulent motions are induced by sweeps passing through the intersections or by the large secondary circulation strengthened by the bottom heating.

Large-scale turbulent motions play a dominant role in vertical transport of scalar in and above the building array. Above the building array, most scalar transport events appear on the low-speed regions where ejections are dominant. Coherent structures of scalar concentration perturbation are tilted downstream and strong spanwise converging flow appears around them especially when the bottom is heated. At the rooftop height, both ejection and sweep are important to the vertical transport of scalar. Ejections pull scalar out of the street canyons and sweeps put above-canyon air into the street canyons and the coherent structures related with sweeps are quite dependent on the adjacent buildings. In the building array, time-averaged scalar concentration is high below the upper low-speed regions and it is low below the upper high-speed regions, confirming the dominant influence of upper turbulence coherent structures on scalar dispersion in the urban canopy.

The effects of urban-like surface with a block array on the dry convective boundary layer (CBL) are investigated using the LES model. Four cases

representing a free CBL, a sheared CBL, and a strongly sheared CBL over flat surfaces and a sheared CBL over a block array are simulated and compared to each other. In the sheared CBL over a block array, the mean flow in the mixed layer is quite decelerated due to the increased surface shear and horizontal convective rolls appear in the mixed layer. In contrast, convection cells and intermediate structures between cells and rolls occur in the free and sheared CBLs over flat surfaces, respectively. Convective rolls and the traces of block-induced turbulent eddies are detected in the spectrum density fields of vertical velocity and the vertical profiles of vertical velocity skewness in the sheared CBL over a block array. Decelerated mixed-layer flow in the sheared CBL over a block array leads to stronger wind shear in the entrainment zone than in the other cases, resulting in streamwise-alternating updrafts and downdrafts there. Due to the enhanced turbulence activity and wave-like motions in the entrainment zone, the magnitude of the entrainment heat flux in the CBL over a block array is larger than that in the other cases.

Turbulent flow in a densely built-up area of Seoul, South Korea, is numerically investigated using the LES model. Based on the analysis of column-averaged vertical turbulent momentum flux, three areas of interest are selected: a downstream area of an apartment complex, an area behind high-rise buildings, and a park area. In the downstream area of the apartment complex, a large wake

develops and a region of strong vertical turbulent momentum flux appears above the wake. In the area behind the high-rise buildings, fluctuating wakes and vortices are distinct flow structures around the top height of the tallest building and updrafts induced by the flow structures appear as strong ejections just behind the high-rise buildings or farther downstream. While strong ejections are dominant at building-top heights, downdrafts along the windward walls of high-rise buildings are distinct below building-top heights and they induce high turbulent kinetic energy and winding flow around the high-rise buildings near the ground surface, transporting momentum downward and intermittently into nearby streets. In the park area located downstream in the main domain, turbulent eddies exist quite above the ground surface, and the thickness of the interfacial region between low-speed air and high-speed air increases and complex turbulent flow appears in the interfacial region.

Turbulent flow in a densely built-up area of Seoul for 0900–1500 LST 31 May 2008 is simulated using the LES model coupled to a mesoscale model (WRF). Time-varying turbulent inflow data (including mesoscale wind) drives quite different turbulence structures depending on time. While upper flow induces strong sweeps for 0900–0910 LST, weaker sweeps and strong ejections are dominant for 1450–1500 LST at  $z = 200$  m and the ejections seem to be induced by buildings or building-induced flow structures. The velocity ratio of

pedestrian wind speed to ambient wind speed indicates ventilation in the urban area, and it is high on broad streets and intersections. While the velocity ratio shows a distinct spatial variation, the temporal variation of the velocity ratio is quite complex, partially depending on mesoscale wind.

**Keywords:** turbulent flow, scalar dispersion, heating, large-eddy simulation, coherent structures, ejection, sweep, convective boundary layer, mesoscale wind

**Student Number:** 2007-30101

# Contents

|  |            |
|--|------------|
| <b>Abstract .....</b>  | <b>i</b>   |
| <b>Contents.....</b>   | <b>vii</b> |
| <b>List of Figures .....</b>   | <b>x</b>   |
| <b>List of Tables.....</b>   | <b>xx</b>  |
| <b>1 Introduction .....</b>  | <b>1</b>   |
| <b>1.1 Review of previous studies .....</b>                          | <b>1</b>   |
| <b>1.1.1 Turbulence coherent structures over urban surfaces.....</b> | <b>1</b>   |
| <b>1.1.2 Thermal effects on flow over urban surfaces .....</b>       | <b>4</b>   |
| <b>1.1.3 Turbulent flow over an actual urban morphology .....</b>    | <b>6</b>   |
| <b>1.2 Objectives of this study.....</b>                             | <b>7</b>   |
| <b>2 Model description.....</b>                                      | <b>10</b>  |
| <b>2.1 Large-eddy simulation model .....</b>                         | <b>10</b>  |
| <b>2.2 Validations .....</b>   | <b>14</b>  |
| <b>2.2.1 Flow over a heated building array .....</b>                 | <b>14</b>  |
| <b>2.2.2 Scalar dispersion in a street canyon.....</b>               | <b>15</b>  |
| <b>3 Turbulent flow and dispersion in and above a street canyon</b>  | <b>19</b>  |
| <b>3.1 Experimental design .....</b>                                 | <b>19</b>  |
| <b>3.2 Mean flow and vertical profiles .....</b>                     | <b>23</b>  |
| <b>3.3 Turbulence structures .....</b>                               | <b>32</b>  |
| <b>4 Turbulent flow in and above a heated building array .....</b>   | <b>42</b>  |

|          |   |            |
|----------|---|------------|
| 4.1      | Experimental design .....   | 42         |
| 4.2      | Vertical profiles .....   | 44         |
| 4.3      | Flow structures above a building array .....                        | 48         |
| 4.4      | Flow structures in a building array.....                            | 65         |
| <b>5</b> | <b>Scalar dispersion in and above a heated building array ..</b>    | <b>86</b>  |
| 5.1      | Vertical turbulent scalar flux.....                                 | 86         |
| 5.2      | Scalar dispersion above a building array .....                      | 90         |
| 5.3      | Scalar dispersion in a building array .....                         | 99         |
| <b>6</b> | <b>Convective boundary layers over flat and urban-like surfaces</b> |            |
|          | .....   | <b>110</b> |
| 6.1      | Experimental design .....   | 110        |
| 6.2      | Turbulence structures .....   | 112        |
| 6.3      | Effects of blocks on the entrainment heat flux.....                 | 122        |
| <b>7</b> | <b>Turbulent flow in a densely built-up urban area .....</b>        | <b>131</b> |
| 7.1      | Experimental design .....   | 131        |
| 7.2      | Turbulence statistics .....   | 134        |
| 7.3      | Turbulent flow behind an apartment complex .....                    | 142        |
| 7.4      | Turbulent flow behind high-rise buildings.....                      | 146        |
| 7.5      | Turbulent flow in a park area.....                                  | 152        |
| <b>8</b> | <b>Impact of mesoscale wind on turbulent flow in a densely</b>      |            |
|          | <b>built-up urban area .....</b>                                    | <b>155</b> |
| 8.1      | Experimental design .....   | 155        |
| 8.2      | Turbulent flow in a densely built-up urban area.....                | 161        |

|  |            |
|--|------------|
| 8.3 Ventilation .....                  | 166        |
| <b>9 Summary and conclusions .....</b> | <b>170</b> |
| <b>References .....</b>                | <b>177</b> |
| <b>초 록.....</b>                        | <b>187</b> |

## List of Figures

|  |    |
|--|----|
| Figure 2.1. Vertical profiles of (a) normalized streamwise velocity and (b) normalized temperature at the center of a street canyon in the present numerical simulation and in the wind-tunnel experiment of Uehara et al. (2000). Here, $U_{2H}$ is the streamwise velocity at $z/H = 2$ , $T_{2H}$ is the temperature at $z/H = 2$ , and $T_0$ is the temperature at $z/H = 0.002$ (very near the bottom surface)..... | 17 |
| Figure 2.2. Normalized mean scalar concentration fields at $z/H = 0.06$ in (a) the wind-tunnel experiment and (b) the present numerical simulation.....  | 18 |
| Figure 3.1. An illustration of the computational domain and building configuration. $H$ is the building height. ....   | 22 |
| Figure 3.2. Streamline fields obtained using time and spanwise averaged velocity components in the (a) NH, (b) UH, (c) BH, and (d) DH cases. ....  | 25 |
| Figure 3.3. Vertical profiles of spanwise-averaged (a) TKE, (b) streamwise velocity variance, and (c) vertical velocity variance at $x/H = 0$ . The variances are normalized by 2 times the value of TKE. ....   | 28 |
| Figure 3.4. Vertical profiles of spanwise-averaged (a) turbulent momentum flux, (b) turbulent scalar flux, and (c) turbulent heat flux at $x/H = 0$ .....  | 29 |
| Figure 3.5. Time- and area-averaged ( $-0.5 \leq x/H \leq 0.5$ ; $-1 \leq y/H \leq 1$ ) (a) mean and turbulent momentum fluxes and (b) mean and turbulent scalar fluxes at the rooftop height in the NH, UH, BH, and DH cases. ....  | 31 |
| Figure 3.6. Spatial-temporal pattern of normalized $\text{sgn}(w') \cdot \max(0, -u'w')$ at the rooftop height in the (a) NH, (b) UH, (c) BH, and (d) DH cases. The instantaneous downward momentum flux is normalized by the  |    |

|   |    |
|---|----|
| magnitude of time- and area-averaged turbulent momentum flux $\overline{ u'w' }$ at<br>the rooftop height. ....   | 34 |
| Figure 3.7. Spatial-temporal pattern of normalized $\text{sgn}(w') \cdot \max(0, c'w')$ at the<br>rooftop height in the (a) NH, (b) UH, (c) BH, and (d) DH cases. The<br>instantaneous upward scalar flux is normalized by the magnitude of<br>time- and area-averaged turbulent scalar flux $\overline{ c'w' }$ at the rooftop height. ....  | 37 |
| Figure 3.8. (a) Frequency $T_i$ and (b) stress fraction $S_i$ of the four quadrant<br>events at $(x, y, z) = (0, 0, H)$ and $(0, 0, 2.5H)$ . ....   | 41 |
| Figure 4.1. Illustrations of (a) the computational domain and building<br>configuration and (b) the sampling points of the vertical profiles in Fig.<br>4.2. $H$ is the building height. ....   | 43 |
| Figure 4.2. Vertical profiles of 12 points-averaged (a) mean streamwise<br>velocity, (b) vertical turbulent momentum flux, (c) RMS of streamwise<br>velocity perturbation, and (d) RMS of vertical velocity perturbation.<br>Sampling points are marked as hollow circles for CC and marked as<br>filled squares for IC in Fig. 4.1b. ....  | 47 |
| Figure 4.3. Instantaneous fields of (a) streamwise velocity, (b) $\max(0, Q)$ , and<br>(c) $\max(0, Q)$ and velocity perturbation vector $(u', w')$ in the $x$ - $z$ plane<br>( $y/H = 15$ ) at $t = 15480$ s in the NH case. The small rectangle in dashed<br>lines is the region of (c). Contours of the vertical gradient of streamwise<br>velocity ( $1.3 \text{ s}^{-1}$ ) are added in (a) and contours of streamwise velocity<br>magnitude ( $5.5 \text{ m s}^{-1}$ ) are added in (b) and (c). .... | 50 |
| Figure 4.4. Instantaneous fields of $\text{sgn}(w') \cdot \max(0, -u'w')$ with the contours of<br>equal streamwise velocity ( $5.5 \text{ m s}^{-1}$ ) at $t = 15480$ s in the (a) $y$ - $z$ plane<br>( $x/H = 16$ ), (b) $x$ - $y$ plane ( $z/H = 3$ ), and (c) $x$ - $y$ plane ( $z/H = 1.2$ ) in the   |    |

- NH case and the same fields at  $t = 19080$  s in the (d)  $y$ - $z$  plane ( $x/H = 10$ ), (e)  $x$ - $y$  plane ( $z/H = 3$ ), and (f)  $x$ - $y$  plane ( $z/H = 1.2$ ) in the BH case.54
- Figure 4.5. Fields of the joint probability density of  $u'$  and  $w'$  in the (a) NH and (b) BH cases and  $u'w'$  multiplied by the joint probability density in the (c) NH and (d) BH cases at  $z/H = 3$ . Dashed lines of equal  $|u'w'|$  ( $2.5 \text{ m}^2 \text{ s}^{-2}$ ) are added. ....60
- Figure 4.6. Conditionally averaged  $u'$  and velocity vector fields in the (a), (d)  $x'$ - $z$  plane ( $y'/H = 0$ ), (b), (e)  $y'$ - $z$  plane ( $x'/H = 0$ ), and (c), (f)  $x'$ - $y'$  plane ( $z/H = 3$ ) in the (left) NH case and (right) BH case. Conditionally averaged  $u'$  instead of  $u$  is used for plotting velocity vector fields, and the contours of equal conditionally averaged pressure perturbation ( $-1$  Pa in the NH case and  $-1.5$  Pa in the BH case) are added.....63
- Figure 4.7. Vertical turbulent momentum flux ( $\overline{u'w'}$ ) fields spanwise averaged over (a) the 12  $x$ - $z$  cross sections containing the CC points, (b) those containing the IC points, and (c) the 12 CC points-centered subregions at  $z/H = 1$  (Fig. 1b) in the NH case. Contours of equal absolute value of the vertical gradient of shear production of turbulent kinetic energy ( $0.06 \text{ m s}^{-3}$ ) are added in (a). The dotted region in (a) indicates the region where the absolute value of the vertical gradient of shear production of turbulent kinetic energy is  $> 0.06 \text{ m s}^{-3}$ . Streamlines are also plotted.....67
- Figure 4.8. The  $u'$  and velocity vector fields in the (a)  $x'$ - $z$  plane ( $y'/H = 0$ ), (b)  $y'$ - $z$  plane ( $x'/H = 0$ ), and (c)  $x'$ - $y'$  plane ( $z/H = 3$ ) conditionally averaged at the tops of the cavity spaces, and the same fields in the (d)  $x'$ - $z$  plane ( $y'/H = 0$ ), (e)  $y'$ - $z$  plane ( $x'/H = 0$ ), and (f)  $x'$ - $y'$  plane ( $z/H = 3$ ) conditionally averaged at the tops of the intersection spaces in the NH

case. Conditionally averaged  $u'$  instead of  $u$  is used for plotting velocity vector fields, and the contours of equal conditionally averaged pressure perturbation ( $-0.95$  Pa) are added. The hatched areas indicate the regions where conditionally averaged pressure perturbation is lower than  $-0.95$  Pa. ....71

Figure 4.9. Fields of (a) vertical turbulent momentum flux ( $\overline{u'w'}$ ) spanwise averaged over the 12  $x$ - $z$  cross sections containing the CC points and (b) correlation coefficient of temperature and  $u'w'$  averaged over the same cross sections in the BH case. Streamlines and contours of equal absolute value of the vertical gradient of shear production of turbulent kinetic energy ( $0.06 \text{ m s}^{-3}$ ) are added in (a). The dotted region in (a) indicates the region where the absolute value of the vertical gradient of shear production of turbulent kinetic energy is larger than  $0.06 \text{ m s}^{-3}$ . ....72

Figure 4.10. Fields of (a) vertical turbulent momentum flux ( $\overline{u'w'}$ ) and (b) spanwise turbulent momentum flux ( $\overline{u'v'}$ ) spanwise averaged over the 12 CC-centered subregions at  $z/H = 0.5$  in the NH case. Streamlines are also plotted. ....75

Figure 4.11. Streamwise velocity perturbation and velocity vector fields in the  $x'$ - $y'$  plane ( $z/H = 0.5$ ) conditionally averaged at  $z/H = 0.5$  in the intersection spaces in the (a) NH and (b) BH cases. Conditionally averaged  $u'$  instead of  $u$  is used for plotting velocity vector fields and the contours of equal conditionally averaged vertical velocity ( $-0.23 \text{ m s}^{-1}$ ) are added. The hatched areas indicate the regions where conditionally averaged downward vertical velocity is higher than  $0.23 \text{ m s}^{-1}$ . ....79

- Figure 4.12. Vertical profiles of 12 points-averaged (a) streamwise length scale of streamwise velocity, (b) spanwise length scale of spanwise velocity, and (c) streamwise length scale of vertical velocity over the IC points in the NH and BH cases. ....81
- Figure 4.13. Time-averaged spanwise velocity fields at  $z/H = 0.1$  and the contours of equal streamwise velocity magnitude ( $6.0 \text{ m s}^{-1}$  in the NH case and  $5.5 \text{ m s}^{-1}$  in the BH case) at  $z/H = 3$  and the contours of equal streamwise velocity magnitude ( $4.4 \text{ m s}^{-1}$  in the NH case and  $4.9 \text{ m s}^{-1}$  in the BH case) at  $z/H = 1.2$  in the (a) NH and (b) BH cases. The dotted and hatched areas indicate low-speed regions at  $z/H = 3$  and high-speed regions at  $z/H = 1.2$ . ....84
- Figure 5.1. Vertical profiles of 12 points-averaged (a) mean scalar concentration, (b) vertical turbulent scalar flux, (c) standard deviation of vertical velocity (based on Park and Baik 2012), and (d) ratio of scalar sweep to scalar ejection in the NH and BH cases. Sampling points are marked as hollow circles for cavity centers (CC) and marked as filled squares for intersection centers (IC) in Fig. 1b. Note that the vertical axis ( $z/H$ ) is on a log scale. ....89
- Figure 5.2. Instantaneous fields of  $\text{sgn}(w') \cdot \max(0, c'w')$  and the contours of equal streamwise velocity ( $5.5 \text{ m s}^{-1}$ ) at  $t = 15480 \text{ s}$  in the (a)  $y-z$  plane ( $x/H = 12$ ), (b)  $y-z$  plane ( $x/H = 19$ ), and (c)  $x-y$  plane ( $z/H = 3$ ) in the NH case and same fields at  $t = 19080 \text{ s}$  in the (d)  $y-z$  plane ( $x/H = 13$ ), (e)  $y-z$  plane ( $x/H = 20$ ), and (h)  $x-y$  plane ( $z/H = 3$ ) in the BH case. ....93
- Figure 5.3. Conditionally averaged  $c'$  and velocity vector fields in the (a)  $x'-z$  plane ( $y'/H = 0$ ), (b)  $y'-z$  plane ( $x'/H = 0$ ), and (c)  $x'-y'$  plane ( $z/H = 3$ ) in the NH case and those in the (d)  $x'-z$  plane ( $y'/H = 0$ ), (e)  $y'-z$  plane

( $x'/H = 0$ ), and (f)  $x'-y'$  plane ( $z/H = 3$ ) in the BH case. Conditionally averaged  $u'$  instead of  $u$  is used for plotting velocity vector fields, and the contours of equal conditionally averaged vertical velocity ( $0.7 \text{ m s}^{-1}$ ) are added. The hatched areas indicate the regions where the conditionally averaged vertical velocity is higher than  $0.7 \text{ m s}^{-1}$  .....94

Figure 5.4. Conditionally averaged  $c'$  and velocity vector fields in the (a)  $x'-z$  plane ( $y'/H = 0$ ), (b)  $y'-z$  plane ( $x'/H = 0$ ), and (c)  $x'-y'$  plane ( $z/H = 3$ ) below upper low-speed regions and those in the (d)  $x'-z$  plane ( $y'/H = 0$ ), (e)  $y'-z$  plane ( $x'/H = 0$ ), and (f)  $x'-y'$  plane ( $z/H = 3$ ) below upper high-speed regions in the BH case. Conditionally averaged  $u'$  instead of  $u$  is used for plotting velocity vector fields, and the contours of equal conditionally averaged vertical velocity ( $0.7 \text{ m s}^{-1}$ ) are added. The hatched areas indicate the regions where the conditionally averaged vertical velocity is higher than  $0.7 \text{ m s}^{-1}$ . .....97

Figure 5.5. Scalar fluxes summed over the surfaces of the virtual box (Fig. 1b) in the (a) NH and (b) BH cases. Positive sign and negative sign indicate influx into the box and efflux from the box, respectively.....102

Figure 5.6. Time-averaged scalar concentration fields at  $z/H = 0.1$  and the contours of equal streamwise velocity magnitude ( $6 \text{ m s}^{-1}$ ) at  $z/H = 3$  in the (a) NH and (b) BH cases. The dotted areas indicate the regions where the mean streamwise velocity is lower than  $6 \text{ m s}^{-1}$  at  $z/H = 3$ . ...105

Figure 5.7. Conditionally averaged  $c'$  and velocity vector fields in the (a),(d)  $x'-z$  plane ( $y'/H = 0$ ), (b),(e)  $y'-z$  plane ( $x'/H = 0$ ), and (c),(f)  $x'-y'$  plane ( $z/H = 1$ ) for (left) scalar ejection and (right) scalar sweep in the NH case. Conditionally averaged  $u'$  instead of  $u$  is used for plotting velocity vector fields, and the contours of equal conditionally averaged

|   |     |
|---|-----|
| streamwise velocity perturbation are added. ( $-0.4 \text{ m s}^{-1}$ for scalar ejection and $1 \text{ m s}^{-1}$ for scalar sweep). .....   | 108 |
| Figure 6.1. Illustrations of the computational domain and block configuration in the SB case.....   | 111 |
| Figure 6.2. Vertical profiles of horizontally averaged (a) vertical turbulent heat flux, (b) potential temperature, (c) vertical turbulent momentum flux, and (d) streamwise velocity in the FF, SF, and SB cases. ....                       | 114 |
| Figure 6.3 Vertical velocity fields at $z = 500 \text{ m}$ in the (a) FF, (b) SF, and (c) SB cases and the same fields at $z = 1000 \text{ m}$ in the (d) FF, (e) SF, and (f) SB cases at $t = 6900 \text{ s}$ . ....                         | 117 |
| Figure 6.4. Spectrum density fields of vertical velocity in the $\lambda_y$ - $z$ plane at $t = 6900 \text{ s}$ in the (a) SF and (b) SB cases. ....  | 120 |
| Figure 6.5. Vertical profiles of spanwise averaged (at $x = 7680 \text{ m}$ ) (a) TKE, (b) skewness of streamwise velocity, and (c) skewness of vertical velocity in the FF, SF, SB, and SSF cases. ....                                      | 121 |
| Figure 6.6. Probability density distributions of streamwise velocity at (a) $z = 500 \text{ m}$ and (b) $z = 1000 \text{ m}$ in the SF, SB, and SSF cases.....  | 123 |
| Figure 6.7. Vertical profiles of spanwise averaged (at $x = 7680 \text{ m}$ ) vertical turbulent heat flux contributed by the four quadrants in the (a) FF, (b) SF, and (c) SB cases.....   | 125 |
| Figure 6.8. Fields of instantaneous heat flux $\theta'w'$ at $z = 1000 \text{ m}$ and $t = 6900 \text{ s}$ in the (a) FF and (b) SB cases. The contours of vertical velocity ( $0.5 \text{ m s}^{-1}$ ) at $z = 500 \text{ m}$ are added..... | 126 |
| Figure 6.9. Cospectral density fields of vertical velocity and potential temperature in the $\lambda_y$ - $z$ plane at $t = 6900 \text{ s}$ in the (a) SF and (b) SB cases. ....  | 129 |

Figure 6.10. The ratio of entrainment heat flux to bottom heat flux  $(-\overline{\langle \theta'w' \rangle}_{z_i} / Q_0)$  with the difference in streamwise velocity between the upper and lower limits of the entrainment zone in all cases. .... 130

Figure 7.1. Elevation field of ground and building top surfaces in the computational domain. The main domain and the areas of interest are indicated by inner rectangle with a solid line and squares with solid lines, respectively. .... 133

Figure 7.2. Fields of (a) mean streamwise velocity at  $z = 100$  m and (b) column-averaged vertical turbulent momentum flux. The areas of interest are indicated by squares with solid lines. .... 136

Figure 7.3. Vertical profiles of area-averaged (a) mean streamwise velocity, (b) vertical velocity variance, and (c) vertical turbulent momentum flux in the four areas. .... 137

Figure 7.4. Fields of the joint probability density function of  $u'$  and  $w'$  at (a)  $z = 100$  m in the main domain, (b)  $z = 150$  m in area 1, and (c)  $z = 250$  m in area 2 and  $u'w'$  multiplied by the joint probability density function at (d)  $z = 100$  m in the main domain, (e)  $z = 150$  m in area 1, and (f)  $z = 250$  m in area 2. Dashed lines of equal  $|u'w'|$  ( $2 \text{ m}^2 \text{ s}^{-2}$ ) are added. .... 140

Figure 7.5. Fields of (a) vertical turbulent momentum flux, (b) instantaneous streamwise velocity at  $t = 1965$  s, and (c)  $\text{sgn}(w') \cdot \max(0, -u'w')$  at  $t = 1965$  s in the  $x$ - $z$  plane ( $y = 1257.5$  m). The contours of streamwise velocity ( $5 \text{ m s}^{-1}$ ) are added. .... 144

Figure 7.6. Conditionally averaged  $u'$  and velocity perturbation vector ( $u', v', w'$ ) fields of ejections in the (a)  $x'$ - $z$  plane ( $y' = 0$  m), (b)  $y'$ - $z$  plane ( $x' = 0$  m), and (c)  $x'$ - $y'$  plane ( $z = 150$  m) and the same fields of sweeps in

the (d)  $x'-z$  plane ( $y' = 0$  m), (e)  $y'-z$  plane ( $x' = 0$  m), and (f)  $x'-y'$  plane ( $z = 150$  m). These are for area 1. The contours of streamwise velocity ( $4 \text{ m s}^{-1}$  for ejections and  $6 \text{ m s}^{-1}$  for sweeps) are added.....145

Figure 7.7. Fields of (a) vertical turbulent momentum flux in the  $x-z$  plane ( $y = 552.5$  m), (b) instantaneous vertical velocity at  $t = 2385$  s in the  $x-y$  plane ( $z = 250$  m), (c) streamwise vorticity at  $t = 2385$  s in the  $x-y$  plane ( $z = 250$  m), and (d)  $\text{sgn}(w') \cdot \max(0, -u'w')$  at  $t = 2385$  s in the  $x-y$  plane ( $z = 250$  m). The contours of streamwise velocity ( $5 \text{ m s}^{-1}$ ) are added. ..148

Figure 7.8. Conditionally averaged  $w$  and velocity perturbation vector ( $u', v', w'$ ) fields in the (a)  $x'-z$  plane ( $y' = 0$  m), (b)  $y'-z$  plane ( $x' = 0$  m), and (c)  $x'-y'$  plane ( $z = 250$  m). These are for area 2. The contours of streamwise velocity ( $5 \text{ m s}^{-1}$ ) are added. ....149

Figure 7.9. Fields of (a) turbulent kinetic energy and mean velocity vector and (b) instantaneous wind speed and velocity vector ( $t = 2105$  s) at  $z = 90$  m. ....151

Figure 7.10. Fields of (a) vertical turbulent momentum flux, (b) instantaneous streamwise velocity at  $t = 2065$  s, and (c)  $\text{sgn}(w') \cdot \max(0, -u'w')$  at  $t = 2065$  s in the  $x-z$  plane ( $y = 1440$  m). The contours of streamwise velocity of  $5 \text{ m s}^{-1}$  (black) and those of  $8 \text{ m s}^{-1}$  (blue) are added. ....154

Figure 8.1. (a) Five domains and (b) innermost domain in the WRF-SNUUCM simulation with terrain height (shaded). (c) Elevation field of ground and building top surfaces in the LES domain. The main domain is indicated by inner rectangle with a solid line in (b) and (c), and the areas of interest are indicated by squares with solid lines in (c). ....157

Figure 8.2. Diurnal variations of observed and WRF-simulated (a) wind speed and (b) wind direction near the surface on 31 May 2008. The

|  |     |
|--|-----|
| observation was made at the Gangnam AWS station and the PALM-simulated data are added.....   | 160 |
| Figure 8.3. Vertical profiles of area-averaged (a) mean streamwise velocity, (b) mean spanwise velocity, and (c) vertical turbulent momentum flux in the main domain for 0900–0910 LST, 1100–1110 LST, 1300–1310 LST, and 1450–1500 LST 31 May 2008. ....  | 162 |
| Figure 8.4. Fields of the joint probability density function of $u'$ and $w'$ at $z = 200$ m in the main domain for (a) 0900–0910 LST and (b) 1450–1500 LST and $u'w'$ multiplied by the joint probability density function at $z = 100$ m in the main domain for (c) 0900–0910 LST and (d) 1450–1500 LST. Dashed lines of equal $ u'w' $ ( $2 \text{ m}^2 \text{ s}^{-2}$ ) are added.....                          | 163 |
| Figure 8.5. Conditionally averaged $w'$ and velocity perturbation vector ( $u'$ , $v'$ , $w'$ ) fields for 0900–0910 LST in the (a) $x'$ - $z$ plane ( $y' = 0$ m), (b) $y'$ - $z$ plane ( $x' = 0$ m), and (c) $x'$ - $y'$ plane ( $z = 200$ m) and the same fields for 1450–1500 LST in the (d) $x'$ - $z$ plane ( $y' = 0$ m), (e) $y'$ - $z$ plane ( $x' = 0$ m), and (f) $x'$ - $y'$ plane ( $z = 200$ m). .... | 165 |
| Figure 8.6. Field of time-averaged velocity ratio ( $V_p/V_{500\text{m}}$ ) in the main domain.....  | 167 |
| Figure 8.7. Area- and time-averaged (for 600 s) (a) velocity ratio ( $V_p/V_{500\text{m}}$ ), (b) TKE, (c) $\text{TKE}/(V_{500\text{m}})^2$ , and (d) $u_{\text{RMS}}/V_{500\text{m}}$ .....   | 169 |

## List of Tables

|  |     |
|--|-----|
| Table 3.1. Heating position, streamwise wind speed at $z = 2H$ , temperature difference between a heated surface and the air at $z = 2H$ , and the bulk Richardson number in the NH, UH, BH, and DH cases. ....  | 21  |
| Table 4.1. Areas occupied by low-speed regions (LSR) and high-speed regions (HSR) at $z/H = 3$ and time- and area-averaged streamwise velocity, vertical velocity, vertical turbulent momentum flux, ratio of vertical turbulent momentum flux by ejections ( $u'_-w'_+$ ) to that by sweeps ( $u'_+w'_-$ ), and $\max(0, Q)$ on the total horizontal domain, LSR, and HSR at $z/H = 3$ , 1.2, 1, and 0.5 in the NH and BH cases. Overbars and angle brackets represent time-average and area-average, respectively. . . . . | 56  |
| Table 5.1. Scalar fluxes summed over the three surfaces of the virtual box (unit: $\mu\text{g s}^{-1}$ ). Overbars represent time averages. . . . .  | 101 |
| Table 6.1. Bottom heat flux, geostrophic wind speed, friction velocity, convective velocity $(gz_i Q_0/T)^{1/3}$ where $g$ is the gravitational acceleration and $T$ is the temperature, the ratio of friction velocity to convective velocity, inversion height, the ratio of inversion height to the Monin-Obukhov length, the thickness of entrainment zone, difference in streamwise velocity between the upper and lower limits of entrainment  |     |

|  |     |
|--|-----|
| zone, turbulent heat flux at the inversion height, and the ratio of vertical<br>turbulent heat flux at the inversion height to bottom heat flux in the FF, SF,<br>SSF, and SB cases..... | 115 |
| Table 8.1. Experimental design in the WRF simulation. ....   | 158 |

# **1 Introduction**

## **1.1 Review of previous studies**

### **1.1.1 Turbulence coherent structures over urban surfaces**

Turbulent flow and scalar dispersion over urban surfaces have become an important issue in urban climate because of their impacts on wind environment and air quality in urban areas. However, turbulent flow and scalar dispersion therein are quite complex due to their turbulent nature (e.g., intermittency), the various shape and arrangement of buildings, building surface or street bottom heating, ambient wind speed and direction, and turbulence induced by vehicles. Many previous studies have focused on the mean and statistical features of turbulent flow and scalar dispersion in relatively simple urban morphologies (Brown et al. 2000; Cheng and Castro 2002; Kim and Baik 2004; Belcher et al. 2005; Li et al. 2006).

Even in a simplified urban morphology such as a street canyon, instantaneous flow and dispersion patterns are important but difficult to understand due to their intermittency. Several studies have stressed on intermittent features of turbulent flow and scalar dispersion in and above a street

canyon. For example, Louka et al. (2000) conducted a field experiment and found that the mean circulation within a street canyon is much weaker than the unsteady turbulent fluctuations. They also insisted that unsteady fluctuations in the shear layer, shedding from the upstream roof, force the unsteady recirculation within the street canyon and transport air into and out of the street canyon. Walton and Cheng (2002) illustrated intermittent features of scalar dispersion by showing the simulated scalar concentration fields in a street canyon at successive instants. Caton et al. (2003) also analyzed the turbulent exchange processes in the shear layer and emphasized the importance of intermittent transport processes.

Turbulent flow accompanying transport processes is intermittent but not always random. In actuality, particular structures known as (turbulence) coherent structures or organized structures appear repeatedly in turbulent flow and they play an important role in the transport processes, as reported by Robinson (1991) and Rossi et al. (2010). Thus, many investigators have tried to understand turbulent flow and scalar dispersion by analyzing coherent structures.

Rotach (1993) analyzed organized turbulence structure using measurement data and emphasized the importance of sweep events for the exchange of canyon air and air above the rooftop height. Rotach (1995) investigated turbulence statistics in and above a street canyon over a long period.

The turbulence statistics are shown to be strongly stability dependent. Cui et al. (2004) simulated turbulent flow in an isothermal street canyon of a unity street aspect ratio and analyzed turbulent events at the rooftop height by performing a quadrant analysis. They showed that weak ejection events are dominant in frequency of occurrence, but fewer strong sweep events contribute to most of the total momentum transport at the rooftop height. By analyzing measurement data, Christen et al. (2007) also emphasized the dominance of sweep events in the turbulent momentum and sensible heat fluxes in large parts of a street canyon and close to the roofs.

Coherent structures appearing above a building array have been investigated by some investigators. Kanda et al. (2004) and Kanda (2006) conducted large-eddy simulations (LES) of turbulent flow over building arrays and investigated characteristics of coherent structures. Both of these studies showed that the streaky structures of low-speed regions and streamwise vortices appear above the building arrays and that the coherent structures resemble those of smooth wall boundary layers. Coceal et al. (2007) proposed a conceptual model of unsteady flow in and above a staggered building array, based on their direct numerical simulation results. According to the conceptual model, coherent structures that appear above the building array resemble well-known structures (e.g., hairpin vortices) that occur in smooth wall boundary layers and they

interact with shear layer structures shed off the tops of buildings. Inagaki and Kanda (2010) analyzed observed data from an outdoor scale model experiment. They found that spatially filtered structures are composed of large streaks of low-speed regions and sub-structures on the streaks and that the substructures are a main cause of ejections. Recently, based on LES results, Inagaki et al. (2012) reported that the coherent structures of velocity and temperature fields in a building array are closely related to the turbulence organized structures above them such as low-speed streaks. They classified the instantaneous flow patterns in a cavity into cavity-eddy and flushing events, and flushing events occur frequently beneath the low-speed streaks.

### **1.1.2 Thermal effects on flow over urban surfaces**

Heating of urban surfaces is one of the main sources of turbulence in urban areas (Christen et al. 2009), and it can affect mean flow, turbulence coherent structures, and transport processes. Thermal effects on mean flow in simplified urban morphologies (e.g., a street canyon or a cubical building array) have been investigated through wind-tunnel experiments, field observations, and numerical simulations (Sini et al. 1996; Kim and Baik 1999; Uehara et al. 2000; Louka et al. 2002; Kovar-Panskus et al. 2002; Xie et al. 2006; Offerle et al. 2007). Mean flow and dispersion in unstably-stratified street canyons were

numerically investigated by Sini et al. (1996), Kim and Baik (1999) using two-dimensional Reynolds-averaged Navier-Stokes equations (RANS) models with the  $k-\varepsilon$  turbulent closure scheme. According to their results, changes in the thermal environment (e.g., heating position and heating intensity) alter mean flow in street canyons. For example, a primary vortex in an isothermal street canyon with the ambient wind perpendicular to the street axis can strengthen or weaken and more vortices can be induced when the building surface or street bottom is heated. Wind-tunnel experiment of Uehara et al. (2000) confirms that bottom heating intensifies a primary vortex in a street canyon. Kovar-Panskus et al. (2002) investigated thermal effects induced by downwind building wall heating through wind-tunnel experiment, and they concluded that downwind building wall heating induces two or more vortices depending on the stability and the strength of ambient flow. In contrast, Louka et al. (2002) compared the results of Nantes'99 campaign and numerical simulations, and they concluded that numerical model overestimates thermal effects on the street-canyon flow. Similarly, Offerle et al. (2007) analyzed wind and temperature measurements within a deep street canyon and concluded that thermal effects on street-canyon flow are not so obvious as shown in the numerical studies. Although thermal effects are not so distinct in field observations due to uncontrollable background meteorological conditions, heating certainly affects flow over urban surfaces to a

large or small degree and it also changes scalar dispersion there.

When the building surface or street bottom is heated, the turbulence structure can change significantly because of turbulent eddies generated by buoyancy as well as turbulent eddies generated by shear instability. There are few studies that focus on turbulence structure over heated urban surfaces. A turbulence study of plant canopies by Shen and Leclerc (1997) showed that the contribution of ejection events to turbulent momentum transport becomes large as the heating intensity just above and below the treetop height increases.

### **1.1.3 Turbulent flow over an actual urban morphology**

Nowadays, digital elevation models (DEM) enable the use of highly accurate urban morphology to simulate turbulent flow in a densely built-up urban area. Nakayama et al. (2011) conducted LES of turbulent flow in an area of Tokyo and proposed a method to estimate aerodynamic roughness parameters for actual urban areas. Nakayama et al. (2012) simulated turbulent flow in an urban area, with mesoscale model simulation data being used as turbulent inflows, and compared wind fluctuations and gust factors to observations. Kanda et al. (2013) conducted LES of fully developed turbulent flow around and above explicitly resolved buildings in Tokyo and Nagoya, and they proposed a new aerodynamic parameterization of roughness length and displacement height in densely built-up

urban areas. However, these studies focus more on estimating aerodynamic parameters and validating the LES model rather than investigating turbulence structures generated by buildings of various shapes and arrangements. Recently, Letzel et al. (2012) investigated pedestrian level ventilation in two neighborhoods in Hong Kong using an LES model. They showed that isolated tall building might have a pronounced impact on ventilation both locally and downstream.

## **1.2 Objectives of this study**

To understand turbulent flow and scalar dispersion over heated urban surfaces, turbulence coherent structures and relevant scalar dispersion patterns over several kinds of urban surfaces are investigated focusing on the effects of urban surface heating. To take into account the heat exchange between the ambient air and the building-wall surfaces, a method that calculates heat fluxes at the building-wall surfaces on the basis of the Monin-Obukhov similarity is developed and validated (Section 2).

Using an LES model that includes the temperature wall function, the effects of differential wall heating on turbulent flow and scalar dispersion in and above an idealized street canyon are investigated. This study attempts to investigate thermal effects on turbulence structure as well as mean flow in and

above a street canyon and to clarify the roles of shear-generated and buoyancy-generated turbulent eddies in momentum and scalar transport when each of upwind building wall, street bottom, and downwind building wall is heated (Section 3).

Turbulent flow and scalar dispersion over isothermal and bottom-heated building arrays are simulated. Turbulence coherent structures that appear above the building arrays are detected by visualizing instantaneous flow fields or extracting conditionally averaged flow structures. The difference between the coherent structures in the neutral case and those in the bottom-heated case is examined. Effects of the coherent structures on turbulent flow and momentum transport at and below the rooftop height are also examined (Section 4).

To understand the relationship of the turbulence coherent structures and scalar dispersion, the simulated scalar dispersion in the neutral and the bottom-heated cases are analyzed. Dominant scalar dispersion patterns and relevant coherent structures are detected by using conditional-averaging method. The effects of coherent structures on scalar dispersion in the neutral and bottom-heated building arrays are also examined (Section 5).

Using the LES model, the effects of urban-like surface with a block array on a dry convective boundary layer are numerically investigated. The turbulence structure of a dry convective boundary layer over an urban-like surface and that

over flat surfaces are compared and the effects of the block array on the entrainment process are examined (Section 6).

Turbulent flow over an actual urban morphology is simulated using the LES model with urban elevation data being used as bottom boundary data. This study aims to investigate characteristic turbulence structures that appear in a densely built-up urban area (Section 7).

Turbulent flow over an actual urban morphology is simulated using the LES model with a mesoscale model data being used as inflow boundary data. Based on the analysis of turbulence structures during the simulation period, turbulent flow and ventilation in a densely built-up urban area are investigated (Section 8).

## 2 Model description

### 2.1 Large-eddy simulation model

The numerical model used in this study is the parallelized large-eddy simulation model (PALM) developed at the Leibniz University of Hannover (Raasch and Schröter 2001; Letzel et al. 2008). PALM is based on the implicitly filtered Boussinesq equations (Letzel 2007). The governing equations are the momentum equation, thermodynamic energy equation, subgrid-scale (SGS) turbulent kinetic energy (TKE) equation, and passive scalar equation can be written as

$$\begin{aligned} \frac{\partial \bar{u}_i}{\partial t} = & -\frac{\partial \bar{u}_k \bar{u}_i}{\partial x_k} \\ & -\frac{1}{\rho_0} \frac{\partial \bar{p}^*}{\partial x_i} - (\varepsilon_{ijk} f_j \bar{u}_k - \varepsilon_{i3k} f_3 u_{gk}) + g \frac{\bar{\theta}^*}{\theta_0} \delta_{i3} - \frac{\partial \overline{u_k'' u_i''}}{\partial x_k} + \left( -\frac{1}{\rho_0} \frac{\partial p_{ext}}{\partial x_i} \right), \end{aligned} \quad (2.1)$$

$$\frac{\partial \bar{\theta}}{\partial t} = -\frac{\partial \bar{u}_k \bar{\theta}}{\partial x_k} - \frac{\partial \overline{u_k'' \theta''}}{\partial x_k}, \quad (2.2)$$

$$\frac{\partial \bar{e}}{\partial t} = -\frac{\partial \bar{u}_j \bar{e}}{\partial x_j} - \overline{u_k'' u_i''} \frac{\partial \bar{u}_i}{\partial x_j} + \frac{g}{\theta_0} \overline{u_3'' \theta''} - \frac{\partial}{\partial x_j} \left\{ \overline{u_j'' \left( e + \frac{p''}{\rho_0} \right)} \right\} - \varepsilon, \quad (2.3)$$

$$\frac{\partial \bar{s}}{\partial t} = -\frac{\partial \bar{u}_k \bar{s}}{\partial x_k} - \frac{\partial \overline{u_k'' s''}}{\partial x_k}, \quad (2.4)$$

where  $\overline{u_k}$  and  $u_k''$  represent filtered part and unresolved fluctuation of  $u$ , and the

SGS TKE is  $\bar{\epsilon} = \frac{1}{2} \overline{u_i'' u_i''}$ . The fourth term in the right-hand side of Eq. (2.3) and

dissipation rate of SGS TKE are parameterized as

$$\overline{u_j'' \left( e + \frac{p''}{\rho_0} \right)} = -2K_m \frac{\partial \bar{\epsilon}}{\partial x_j}, \quad (2.5)$$

$$\epsilon = \left( 0.19 + 0.74 \frac{l}{\Delta} \right) \cdot \frac{\bar{\epsilon}^{3/2}}{l}. \quad (2.6)$$

The governing equations are numerically solved using the third-order Runge–Kutta scheme for time integration and the second-order Piacsek and Williams (1970) scheme for advection. The SGS turbulent fluxes are parameterized using the 1.5 order Deardorff (1980) scheme, which uses SGS TKE to calculate eddy viscosity.

$$\overline{u_k'' u_i''} = -K_m \left( \frac{\partial \bar{u}_i}{\partial x_k} + \frac{\partial \bar{u}_k}{\partial x_i} \right), \quad (2.7)$$

$$\overline{u_k'' \theta''} = -K_h \frac{\partial \bar{\theta}}{\partial x_k}, \quad (2.8)$$

$$\overline{u_k s''} = -K_s \frac{\partial \bar{s}}{\partial x_k}, \quad (2.9)$$

$$K_m = c_m l \sqrt{\bar{e}}, \quad (2.10)$$

$$K_h = \left(1 + \frac{2l}{\Delta}\right) K_m. \quad (2.11)$$

At the grid points closest to all the solid surfaces, the Monin–Obukhov (MO) similarity is employed in the momentum equation and the passive scalar equation. In the previous version of PALM, heat fluxes that are based on the MO similarity or prescribed constant heat fluxes are applied at the bottom and building-top surfaces, whereas only prescribed constant heat fluxes are applied at the building-wall surfaces. To take into account the heat exchange between the ambient air and the building wall-surfaces, a method that calculates heat fluxes at the building-wall surfaces on the basis of the MO similarity is developed for this study. Because the resolved heat flux at the building-wall surfaces is usually negligible, the heat flux at the building-wall surfaces is nearly equal to the SGS heat flux (the product of friction velocity and friction temperature).

$$\overline{w'' T''_0} = -u_* T_*. \quad (2.12)$$

The gradient of  $u$  and  $T$  near the wall surface and the universal similarity function for momentum and heat can be given as

$$\frac{\partial \bar{u}}{\partial z} = \frac{u_*}{\kappa z} \Phi_m, \quad (2.13)$$

$$\frac{\partial \bar{T}}{\partial z} = \frac{T_*}{\kappa z} \Phi_h, \quad (2.14)$$

$$\Phi_m = \begin{cases} 1 + 5Ri_f & \text{stable} \\ 1 & \text{neutral} \\ (1 - 16Ri_f)^{-1/4} & \text{unstable} \end{cases}, \quad (2.15)$$

$$\Phi_h = \begin{cases} 1 + 5Ri_f & \text{stable} \\ 1 & \text{neutral} \\ (1 - 16Ri_f)^{-1/2} & \text{unstable} \end{cases}. \quad (2.16)$$

Integrating Eq. (2.13) and Eq. (2.14) from  $z_0$  to  $z_p$  (the grid point closest to the wall surface), the friction velocity and friction temperature are calculated as

$$u_* = \frac{\kappa [\bar{u}]_{z_0}^{z_p}}{\int_{z_0}^{z_p} \Phi_m d \ln z}, \quad (2.17)$$

$$T_* = \frac{\kappa [\bar{T}]_{z_0}^{z_p}}{\int_{z_0}^{z_p} \Phi_h d \ln z}. \quad (2.18)$$

Then, the heat flux at the building wall surface is obtained by calculating the product of the calculated friction velocity and friction temperature. In general, the applicability of the MO similarity (for heat fluxes at building scale) is not ensured. Nevertheless, the MO similarity showed good performance in the validation tests in this study (section 2.2.1), and therefore it was selected as a temperature wall function.

## 2.2 Validations

### 2.2.1 Flow over a heated building array

The LES model is validated using the wind-tunnel data of Uehara et al. (2000). Figure 2.1 shows the vertical profiles of normalized streamwise velocity and normalized temperature at the center of a street canyon in the numerical simulation and wind-tunnel experiment. As in the wind-tunnel experiment, an array of cubical buildings is considered in the numerical simulation and the street width in the  $x$  direction is equal to the building height and the street width in the  $y$  direction is equal to half the building height. Turbulent flow in and above the

building array for each of the isothermal (neutral) and bottom-heated (unstable) cases is simulated. In the unstable case, the temperature of the bottom is adjusted to be 13 K higher than that of the ambient air to set the bulk Richardson number of the numerical simulation similar to that of the wind-tunnel experiment ( $R_b = -0.21$ ). In the numerical simulation and wind-tunnel experiment, the magnitude of normalized streamwise velocity in the unstable case is larger than that in the neutral case in and above the building array. Although there are some discrepancies in the magnitude of normalized streamwise velocity, the LES model properly simulates the strengthened vortex circulation in the bottom-heated street canyon. Moreover, the vertical profile of normalized temperature in the numerical simulation is in good agreement with that in the wind-tunnel experiment.

### **2.2.2 Scalar dispersion in a street canyon**

The LES model is validated using the wind-tunnel data from the Compilation of Experimental Data for Validation of Microscale Dispersion Models (CEDVAL) database hosted at the University of Hamburg (online at <http://www.mi.uni-hamburg.de/cedval.html>). For this, a numerical simulation with a  $3 \times 7$  rectangular building array is conducted and the normalized scalar concentration field around the scalar sources (including the cavity spaces

between the fifth and sixth buildings) is compared with that of the wind-tunnel experiment. Figure 2.2 shows the normalized mean scalar concentration fields at  $z/H = 0.06$  in the wind-tunnel experiment and numerical simulation. The normalized mean scalar concentration in the numerical simulation is defined as  $K = U_{ref} H^2 C_m / A \overline{c'w'_0}$ , where  $U_{ref}$  is the mean streamwise velocity magnitude at  $z/H = 1$ ,  $H$  is the building height,  $C_m$  is the measured mean scalar concentration,  $A$  is the area of scalar sources, and  $\overline{c'w'_0}$  is the vertical scalar flux at the bottom ( $5 \mu\text{g m}^{-2} \text{s}^{-1}$ ). The ratio of block height in the wind-tunnel experiment and building height in the numerical simulation is 1:200, and the scales in the  $x$  and  $y$  directions in Fig. 2.2 are normalized by the block height or building height. In the wind-tunnel experiment and numerical simulation, the overall magnitudes of normalized mean scalar concentration are similar to each other. Although there are some discrepancies of mean scalar fields in the central region of cavity space that are due to strongly simulated double-eddy circulation there, overall the mean scalar distribution patterns are similar to each other.

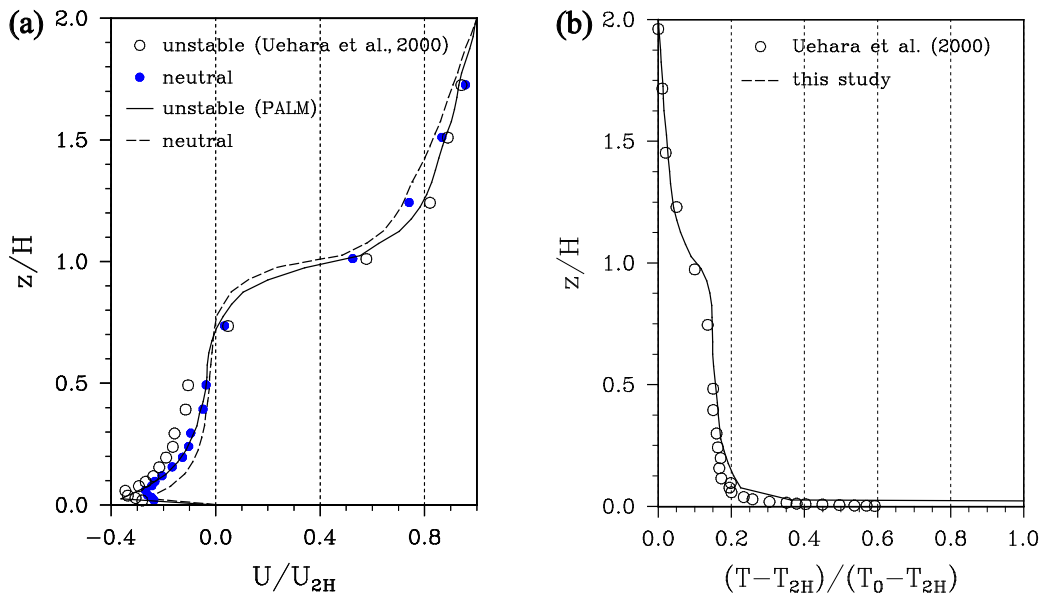


Figure 2.1. Vertical profiles of (a) normalized streamwise velocity and (b) normalized temperature at the center of a street canyon in the present numerical simulation and in the wind-tunnel experiment of Uehara et al. (2000). Here,  $U_{2H}$  is the streamwise velocity at  $z/H = 2$ ,  $T_{2H}$  is the temperature at  $z/H = 2$ , and  $T_0$  is the temperature at  $z/H = 0.002$  (very near the bottom surface).

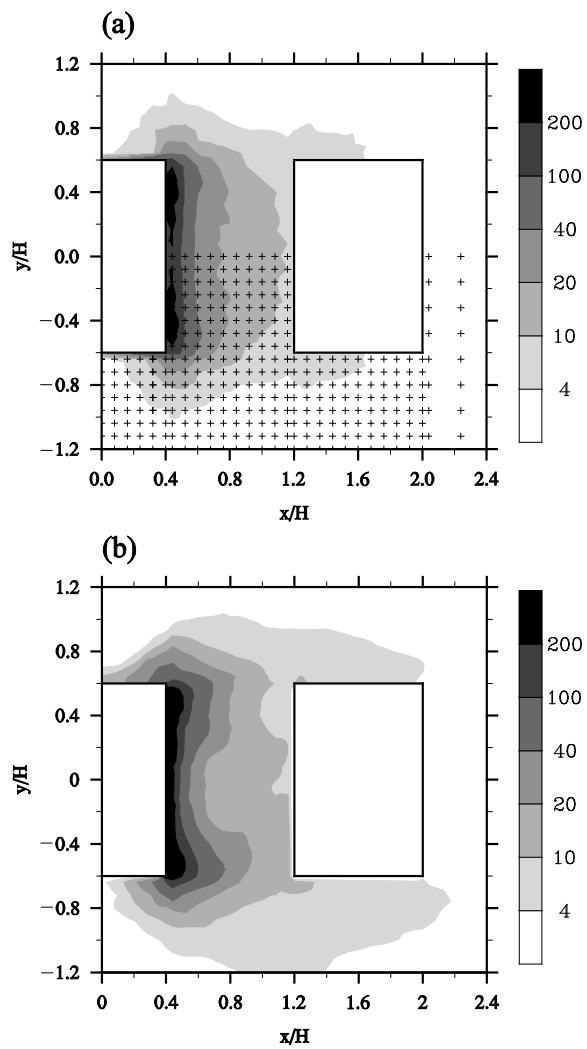


Figure 2.2. Normalized mean scalar concentration fields at  $z/H = 0.06$  in (a) the wind-tunnel experiment and (b) the present numerical simulation.

# 3 Turbulent flow and dispersion in and above a street canyon

## 3.1 Experimental design

A simple urban canopy with two buildings (20 m high) and a street canyon (20 m wide) is considered here (Fig. 3.1). The street aspect ratio, defined as the ratio of the building height to the distance between the two buildings, is one. The size of the computational domain is 40 m in the  $x$  (streamwise) direction, 40 m in the  $y$  (spanwise) direction, and 109 m in the  $z$  (vertical) direction. The grid size in both the  $x$  and  $y$  directions is 0.5 m. In the  $z$  direction, the grid size is uniform up to  $z = 50$  m and then gradually increases with an expansion ratio of 1.08. Considering that infinitely long street canyons are repeated in the  $x$  direction, the cyclic boundary condition is applied at the lateral boundaries for velocity components and SGS TKE. The zero-gradient boundary condition is applied at the top boundary. The initial ambient wind direction is perpendicular to the spanwise direction, and the initial vertical profile of the ambient wind speed is logarithmic. The initial volume flow rate at the inflow boundary is conserved to maintain quasi-steady mean flow in the model domain, and the Coriolis effect is not considered here.

At the grid points closest to all the solid surfaces, the MO similarity is

employed in the momentum equation, the thermodynamic energy equation and the passive scalar equation. Passive scalars are emitted at all grid points of the street bottom; the emitted passive scalar flux is  $5 \text{ kg m}^{-2} \text{ s}^{-1}$ . The passive scalar concentration is set equal to zero and the temperature is fixed at 300 K at the inflow boundary to maintain quasi-steady mean states of scalar and temperature fields. The situation of zero passive scalar concentration at the inflow boundary corresponds to a situation in which ambient fresh air continuously flows into the domain. PALM is integrated for 3 h, and the last 30-min simulation data are used for analysis.

To investigate thermal effects on turbulent flow and dispersion, four simulations are conducted with different heating positions: a no-heating (NH) case (control case), a case with upwind building-wall heating (UH), a case with street-bottom heating (BH), and a case with downwind building-wall heating (DH). Table 3.1 shows the heating position, streamwise wind speed at  $z = 2H$  (40 m), temperature difference between a heated surface and the air at  $z = 2H$ , and bulk Richardson number in the NH, UH, BH, and DH cases. Here, the bulk Richardson number is defined as  $R_b = [(g/T_{2H})(T_{2H} - T_w)/2H] / (U_{2H}/2H)^2$ , where  $H$  denotes the building height and  $T_{2H}$  and  $U_{2H}$  denote the temperature and streamwise wind speed at  $z = 2H$ , respectively.  $T_w$  is the temperature of heated building wall or street bottom, and  $g$  is the gravitational acceleration.

Table 3.1. Heating position, streamwise wind speed at  $z = 2H$ , temperature difference between a heated surface and the air at  $z = 2H$ , and the bulk Richardson number in the NH, UH, BH, and DH cases.

| cases | heating position       | $U_{2H}$ (m s <sup>-1</sup> ) | $T_w - T_{2H}$ (K) | $R_b$ |
|-------|------------------------|-------------------------------|--------------------|-------|
| NH    | no heating             | 2.6                           | 0                  | 0     |
| UH    | upwind building wall   | 2.4                           | 20                 | -4.54 |
| BH    | street bottom          | 2.3                           | 20                 | -4.94 |
| DH    | downwind building wall | 2.2                           | 20                 | -5.40 |

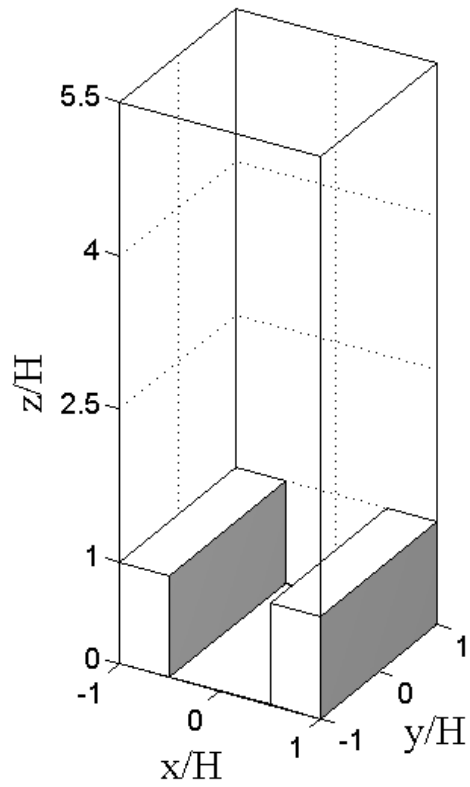


Figure 3.1. An illustration of the computational domain and building configuration.  $H$  is the building height.

Streamwise wind speeds at  $z = 2H$  ( $2.2 - 2.6 \text{ m s}^{-1}$ ) are strong enough to induce a primary vortex and corner vortices in the street canyon, and the temperature of a heated surface (320 K) is high enough to affect flow therein.

## 3.2 Mean flow and vertical profiles

Figure 3.2 shows streamline fields obtained using time- and spanwise-averaged velocity components in the NH, UH, BH, and DH cases. In the NH case, a primary vortex and small corner vortices appear in the street canyon (Fig. 3.2a). In the UH case, updraft near the heated upwind building wall strengthens the primary vortex and the primary vortex expands above the rooftop height (Fig. 3.2b). The street-bottom heating also reinforces the primary vortex, but the streamline pattern is similar to that of the NH case without any noticeable expansion above the rooftop height. When compared with the UH and BH cases, the downwind building-wall heating results in considerably different mean flow patterns (Fig. 3.2d). In the DH case, the primary vortex shrinks and a winding flow appears between the primary vortex and the downwind building wall. Because of the downwind building-wall heating, strong updrafts are generated along the downwind building wall, and these updrafts block incoming ambient flow. As a result, the ambient air descends not along the downwind building wall but across the region between  $x/H = 0.1$  and  $x/H = 0.4$  at the rooftop height. The

incoming flow and thermally induced updrafts near the downwind building wall form the winding flow. With the winding flow, the streamlines in the street canyon are no longer completely closed. A similar flow pattern is also observed in the wind-tunnel experiment of Kovar-Panskus et al. (2002). This winding flow is a unique flow pattern that can appear when the mechanical and thermal forcings act together but in opposite ways in a narrow region, and its spatial scale is sensitive to the ambient wind speed and heating intensity.

Figure 3.3 shows the vertical profiles of spanwise-averaged TKE, streamwise velocity variance  $\overline{u'^2}$ , and vertical velocity variance  $\overline{w'^2}$  at  $x/H = 0$ . The variances are normalized by 2 times the value of TKE. Here,  $u'$  and  $w'$  denote deviations from the time- and spanwise-averaged velocity components  $\overline{U}$  and  $\overline{W}$ , respectively. The maximum TKE of each case appears at the rooftop height in all cases except the BH case. The maximum TKE at the rooftop height is attributed to the activity of turbulent eddies starting from the upwind building top and passing above the street canyon. The turbulent eddies are mainly generated by shear instability (see Letzel et al. 2008), and the shear production is the main source of TKE, not only in the NH case but also in the cases in which the building wall is heated (UH and DH). In the BH case, the maximum TKE appears at half the rooftop height, indicating high turbulence activity inside the street canyon. The street-bottom heating makes street-canyon flow highly

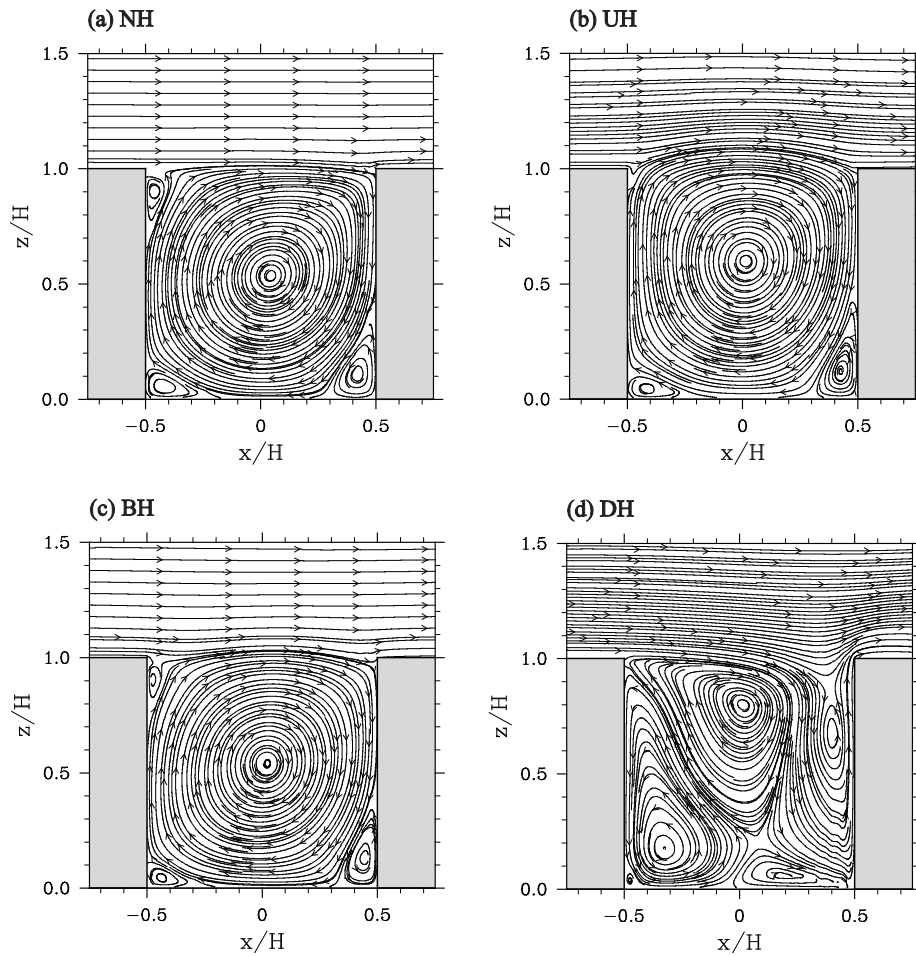


Figure 3.2. Streamline fields obtained using time and spanwise averaged velocity components in the (a) NH, (b) UH, (c) BH, and (d) DH cases.

turbulent, whereas the heating of the upwind or downwind building wall induces turbulent eddies that are locally concentrated near the heated building wall. In fact, snapshots of the instantaneous flow field demonstrate that the street-canyon flow is more intermittent and fluctuating in the BH case than in the UH and DH cases (not shown). The change of the heating position also modifies the variances of streamwise velocity and vertical velocity, leading to a modified turbulence structure. In the NH case, TKE at the rooftop height is mainly composed of the variance of streamwise velocity. In contrast to the NH case, heating increases the ratio of vertical velocity variance to TKE at the rooftop height (Fig. 3.3c), resulting in stronger turbulent fluxes in the vertical direction (see Fig. 3.4). It is analyzed that the mixing-layer analogy (Raupach et al. 1996) can be applied for the variance of streamwise velocity (normalized by the friction velocity) at the rooftop height in all cases, including the heating cases, but the variances of spanwise horizontal velocity and vertical velocity do not satisfy the mixing-layer analogy, even in the neutral case (not shown). Above  $z/H = 1.4$ , the magnitude of the streamwise velocity variance is larger than that of the vertical velocity variance in all cases. This is a typical characteristic of turbulence in the roughness sublayer influenced by outer-layer disturbances and as observed in the field observation results of Inagaki and Kanda (2008).

Figure 3.4 shows the vertical profiles of the spanwise-averaged turbulent

fluxes of momentum  $\overline{u'w'}$ , scalar  $\overline{c'w'}$ , and heat  $\overline{\theta'w'}$  at  $x/H = 0$ .  $c'$  and  $\theta'$  denote deviations from the time- and spanwise-averaged passive scalar concentration  $\overline{C}$  and potential temperature  $\overline{\Theta}$ , respectively. The turbulent fluxes include only resolved turbulent fluxes ( $\overline{x'w'}$ ) (here, the variable  $x$  can be  $u$ ,  $c$  or  $\theta$ ) because the magnitude of SGS flux is much smaller than that of resolved-scale flux. In the NH, UH, and BH cases, all of the vertical profiles have their maximum magnitudes at or near the rooftop height. The vertical profiles of turbulent scalar flux in the NH, UH, and BH cases have second maximum magnitudes near the street bottom due to the fluctuations of scalar concentration around the scalar source. In the DH case, the turbulent scalar flux has a maximum value at  $z/H = 0.2$  and not at the rooftop height because wind shear at the rooftop height is weak as a result of the modified flow pattern. The modified flow pattern in the DH case also affects turbulent heat flux in the street canyon. The modified flow pattern induces turbulent eddies concentrated near the downwind building wall, leading to greater heat exchange there. The modified flow pattern decreases the magnitude of turbulent heat flux at  $x/H = 0$  in the DH case when compared with the magnitude in other cases (UH and BH cases). The secondary maximum magnitude of  $\overline{\theta'w'}$  near the bottom in the BH case is due to the bottom heating.

Time- and area-averaged ( $-0.5 \leq x/H \leq 0.5$ ;  $-1 \leq y/H \leq 1$ ) mean

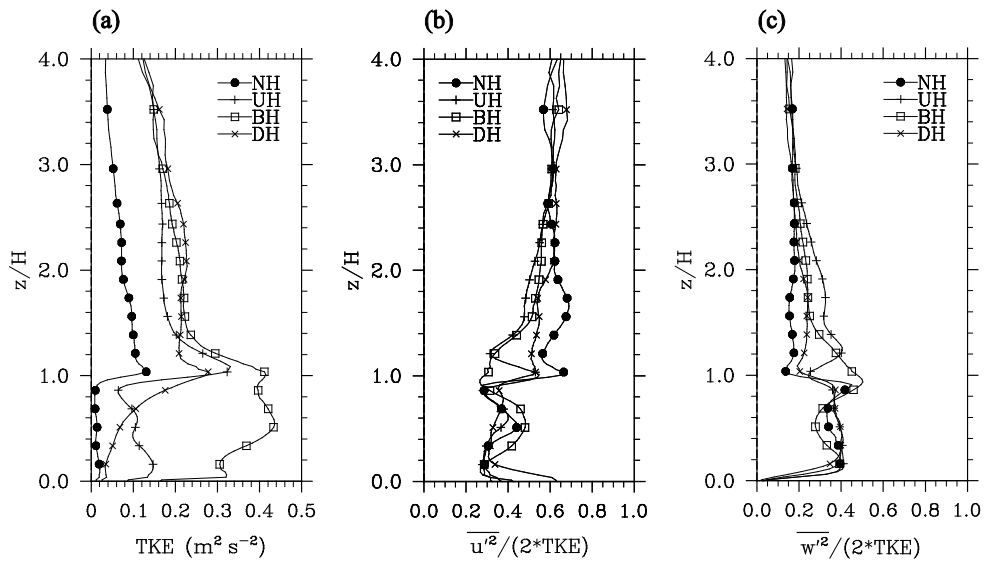


Figure 3.3. Vertical profiles of spanwise-averaged (a) TKE, (b) streamwise velocity variance, and (c) vertical velocity variance at  $x/H = 0$ . The variances are normalized by 2 times the value of TKE.

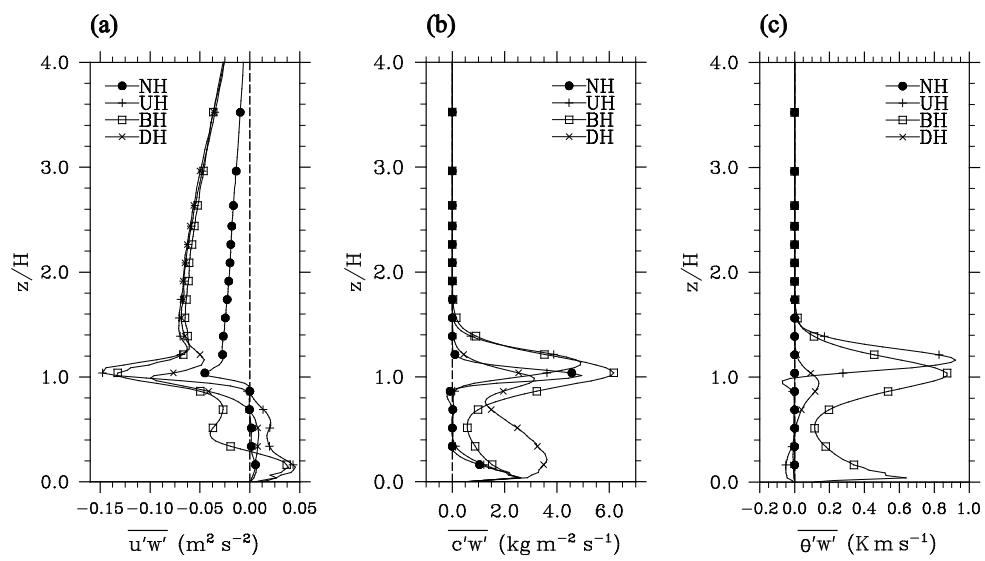


Figure 3.4. Vertical profiles of spanwise-averaged (a) turbulent momentum flux, (b) turbulent scalar flux, and (c) turbulent heat flux at  $x/H = 0$ .

momentum flux  $\overline{UW}$ , turbulent momentum flux  $\overline{u'w'}$ , mean scalar flux  $\overline{CW}$ , and turbulent scalar flux  $\overline{c'w'}$  at the rooftop height in the NH, UH, BH, and DH cases are shown in Fig. 3.5. In all cases, the mean and turbulent momentum fluxes at the rooftop height are negative (downward) and the magnitude of turbulent momentum flux is much larger than that of mean momentum flux. The magnitude of turbulent momentum flux is much larger in the UH, BH, and DH cases than in the NH case. The enhancement of turbulent momentum flux due to the street-bottom or building-wall heating can be explained by stronger turbulence activity at the rooftop height caused by the intensified in-canyon circulation (UH and BH cases) and the winding flow (DH case). As already mentioned, both the intensified in-canyon circulation and the winding flow induce strong fluctuations of vertical velocity at the rooftop height, and therefore the turbulent momentum flux dominates over the mean momentum flux. In all cases, the mean and turbulent scalar fluxes at the rooftop height are positive (upward) except the mean scalar flux in the NH case, and the magnitude of turbulent scalar flux is larger than that of mean scalar flux. Note that the magnitude of turbulent momentum flux (also turbulent scalar flux) is largest in the BH case. However, the magnitude of mean momentum flux (and also mean scalar flux) is smallest in the BH case, although the difference between the NH and BH cases is small.

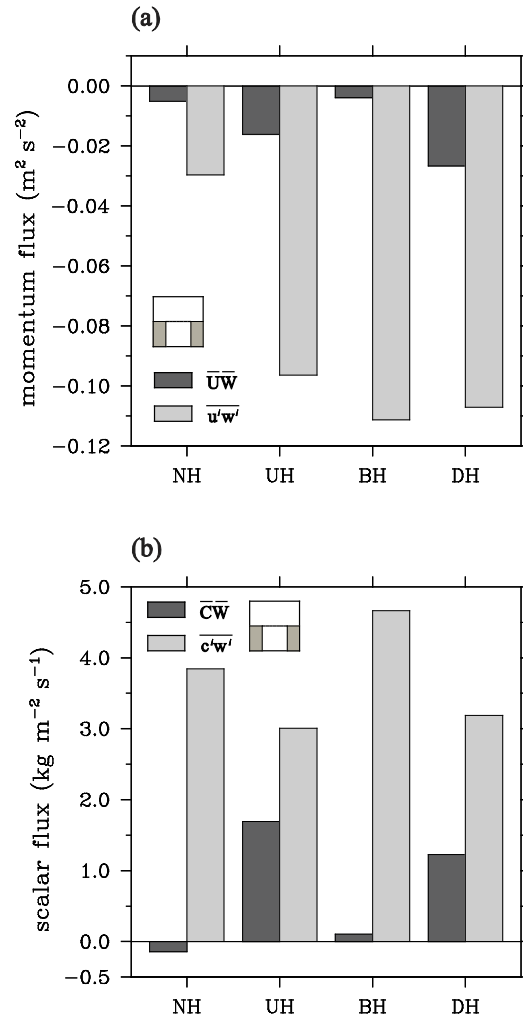


Figure 3.5. Time- and area-averaged ( $-0.5 \leq x/H \leq 0.5$ ;  $-1 \leq y/H \leq 1$ ) (a) mean and turbulent momentum fluxes and (b) mean and turbulent scalar fluxes at the rooftop height in the NH, UH, BH, and DH cases.

The area-averaged mean momentum flux is actually the sum of dispersive momentum flux and the product of time- and area-averaged streamwise velocity and vertical velocity. Below the rooftop height, the magnitude of the product is negligible in comparison with that of the dispersive momentum flux. While the dispersive momentum flux is negative at the rooftop height the dispersive momentum flux below the rooftop height is positive, and its magnitude is comparable to the magnitude of turbulent momentum flux in all cases except the DH case (not shown). The positive dispersive momentum flux is attributed to the existence of the primary vortex in the street canyon, and this is consistent with the results of Martilli and Santiago (2007).

### 3.3 Turbulence structures

To examine thermal effects on instantaneous momentum transport events, the spatial-temporal pattern of normalized  $\text{sgn}(w') \cdot \max(0, -u'w')$  for the last 300 s (from 10500 s to 10800 s) at the rooftop height is plotted in Fig. 3.6. The quantity  $\text{sgn}(w') \cdot \max(0, -u'w')$  is the product of the sign of vertical velocity perturbation and the magnitude of downward turbulent momentum flux (0 for upward turbulent momentum flux). Thus, the spatial-temporal fields of  $\text{sgn}(w') \cdot \max(0, -u'w')$  clearly visualize the distribution of downward momentum

transport events accompanying updrafts (ejections) and those accompanying downdrafts (sweeps). In the figure,  $\text{sgn}(w') \cdot \max(0, -u'w')$  is normalized by the magnitude of time- and area-averaged turbulent momentum flux  $|\overline{u'w'}|$  at the rooftop height to emphasize intermittent and dominant turbulent events. In the NH case, the perturbation patterns are band shaped with a constant slope, corresponding to a reciprocal of transfer velocity. This indicates that momentum is mostly transported by turbulent eddies that move with a constant velocity ( $\sim 0.7 \text{ m s}^{-1}$ ). The slope of perturbations in the UH and BH cases is gentler than that in the NH case, corresponding to a faster transfer velocity ( $\sim 1.5 \text{ m s}^{-1}$ ) at the rooftop height. The estimated transfer velocity is nearly identical to the mean streamwise velocity at the rooftop height in all cases. Strong turbulent events occur more frequently in the UH case due to the strong flow at the rooftop height. Although the band-shaped patterns are still maintained in the UH case, the magnitude of momentum transport by individual turbulent events increases, especially near the upwind building wall. Contrary to the UH case, the street-bottom heating induces more intermittent turbulent eddies, and the eddies sometimes have band-shaped and sometimes lump-shaped patterns in the  $x-t$  plane. In the BH case, heating is not localized but spreads throughout the entire street canyon, and this kind of heating induces more fluctuating flow therein and more intermittent turbulence signals at the rooftop height. The downwind

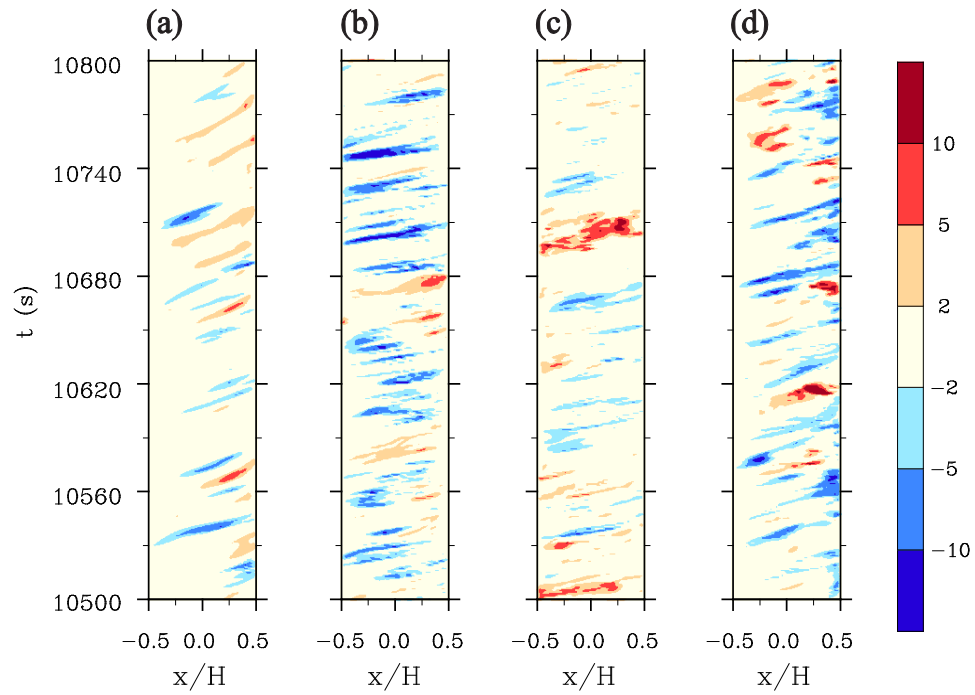


Figure 3.6. Spatial-temporal pattern of normalized  $\text{sgn}(w') \cdot \max(0, -u'w')$  at the rooftop height in the (a) NH, (b) UH, (c) BH, and (d) DH cases. The instantaneous downward momentum flux is normalized by the magnitude of time- and area-averaged turbulent momentum flux  $|\overline{u'w'}|$  at the rooftop height.

building-wall heating induces strong updrafts near the downwind building wall, and turbulent eddies related to the updrafts appear as lump-shaped perturbations in the  $x-t$  plane. Lump-shaped perturbations coexist with weaker band-shaped perturbations (Fig. 3.6d), and turbulent eddies corresponding to the two kinds of perturbations dominate mixing at the rooftop height.

Figure 3.7 shows the spatial-temporal pattern of normalized  $\text{sgn}(w') \cdot \max(0, c'w')$  for the last 300 s at the rooftop height. Also in this figure,  $\text{sgn}(w') \cdot \max(0, c'w')$  is normalized by the magnitude of time- and area-averaged turbulent scalar flux  $|\overline{c'w'}|$  at the rooftop height. As in momentum transport events, band-shaped scalar transport events appear in the NH case. This similarity indicates that turbulent eddies generated by shear instability dominate passive scalar transport at the rooftop height. At the rooftop height, sweep events draw ambient fresh air into the street canyon and ejection events get passive scalar out from the street canyon, resulting in a net upward scalar transport. In the UH case, both shear instability and heating generate turbulent eddies near the upwind building wall. Scalar-escaping events and above-canyon-air-incoming events are concentrated in the upwind region between  $x/H = -0.5$  and  $x/H = 0$ . In the BH case, distinctly intermittent transport patterns are repeated in the instantaneous turbulent scalar flux field. In the DH case, lump-shaped scalar transport events dominate scalar transport at the rooftop height, especially near

the downwind building wall. Near the heated downwind building wall, the scalar transport events induced by local downdrafts are lump shaped. When compared with the momentum transport events, thermal effects due to the change of the heating position are more distinct in the scalar transport events at the rooftop height because scalar transport events are more dependent on the fluctuations of vertical velocity and the intensity of updrafts. Overall, the timing of the momentum (scalar) transport seems to be determined by outer flow in the NH and UH cases where sweep events are dominant, whereas the timing seems to be dependent on both outer flow and in-canyon flow in the BH and DH cases where ejection events are comparable to sweep events.

To investigate thermal effects on the turbulence structure in the shear layer, a quadrant analysis is performed. Quadrant analyses have been used in numerous studies, including plant-canopy turbulence (Shaw et al. 1983) and urban surface-layer turbulence (Raupach 1981; Rotach 1993; Cui et al. 2004; Christen et al. 2007). The instantaneous turbulent momentum flux  $u'w'$  (or instantaneous Reynolds stress) at one position can be classified into four quadrants: outward interaction ( $u' > 0; w' > 0$ ), ejection ( $u' < 0; w' > 0$ ), inward interaction ( $u' < 0; w' < 0$ ), and sweep ( $u' > 0; w' < 0$ ). Following the method of Raupach (1981), the frequency (or time fraction) and the contribution to turbulent momentum flux of quadrant  $i$  are expressed by

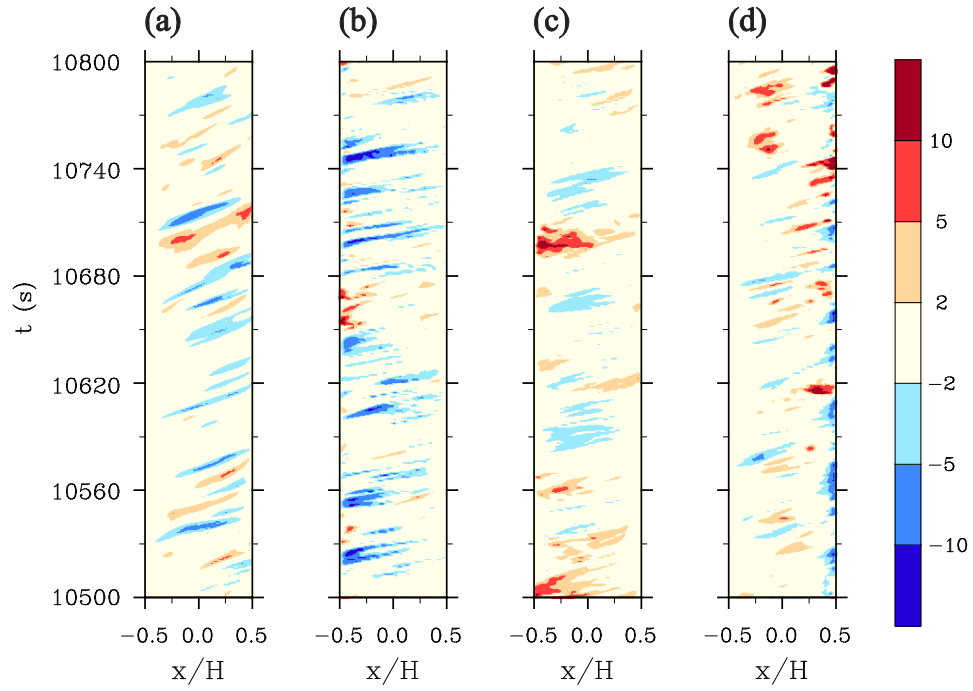


Figure 3.7. Spatial-temporal pattern of normalized  $\text{sgn}(w') \cdot \max(0, c'w')$  at the rooftop height in the (a) NH, (b) UH, (c) BH, and (d) DH cases. The instantaneous upward scalar flux is normalized by the magnitude of time- and area-averaged turbulent scalar flux  $\overline{|c'w'|}$  at the rooftop height.

$$T_i = T^{-1} \int_T I_i[u'(t), w'(t)] dt \quad \text{and} \quad (3.1)$$

$$\langle u'w' \rangle_i = T^{-1} \int_T u'(t)w'(t)I_i[u'(t), w'(t)] dt, \quad (3.2)$$

where the indicator function  $I_i$  is 1 if  $(u', w')$  is in quadrant  $i$  and is 0 if otherwise. The stress fraction, a ratio of the contribution of quadrant  $i$  to turbulent momentum flux (Reynolds stress), is

$$S_i = \langle u'w' \rangle_i / \overline{u'w'}. \quad (3.3)$$

Figure 3.8 shows the frequency  $T_i$  and the stress fraction  $S_i$  of turbulent events at  $(x, y, z) = (0, 0, H)$  and  $(0, 0, 2.5H)$ . In this study, the results at one point (not spanwise averaged) are presented because the spanwise variation of conditional statistics is negligible. At the rooftop height, ejection and sweep events occur most frequently and contribute to most of turbulent momentum flux. In the NH and UH cases, sweep events contribute more to turbulent momentum flux than do ejection events, although ejection events occur more frequently. This kind of trend is one of the typical turbulence structures at the top of the

canopy layer because of the dominance of turbulent eddies generated by shear instability. This result is consistent with the results of Cui et al. (2004). When the street bottom or downwind building wall is heated, the frequency of ejection events is close to that of sweep events and the difference in the stress fraction between the two events becomes smaller than the difference in the NH and UH cases. This emphasizes the important role ejection events play in momentum transport in the BH and DH cases. In the BH and DH cases, buoyancy-generated turbulent eddies appear as strong ejection events at the rooftop height (corresponding to the lump-shaped perturbations in Fig. 3.6) and change the turbulence structure in the shear layer (including the rooftop height). The frequency and stress fraction in the roughness sublayer ( $z/H = 2.5$ ) are also shown in Fig. 3.8 to compare the turbulence structure in the roughness sublayer with that in the shear layer. In the roughness sublayer, ejection events contribute more to turbulent momentum flux than do sweep events in the NH and DH cases and vice versa in the UH and BH cases. The dominance of sweep events over ejection events in the NH and UH cases in the shear layer does not appear any more in the roughness sublayer. In addition, the difference in stress fraction has less influence on turbulent momentum flux in the roughness sublayer than in the shear layer because the magnitude of turbulent momentum flux in the roughness sublayer is much smaller than that at the rooftop height. Thus, the only common

characteristic of turbulence structures at both heights is the dominance of ejection and sweep events over outward and inward interaction events in turbulent momentum flux. This indicates that the effects of differential heating positions are confined to the street canyon and the shear layer just above the rooftop height.

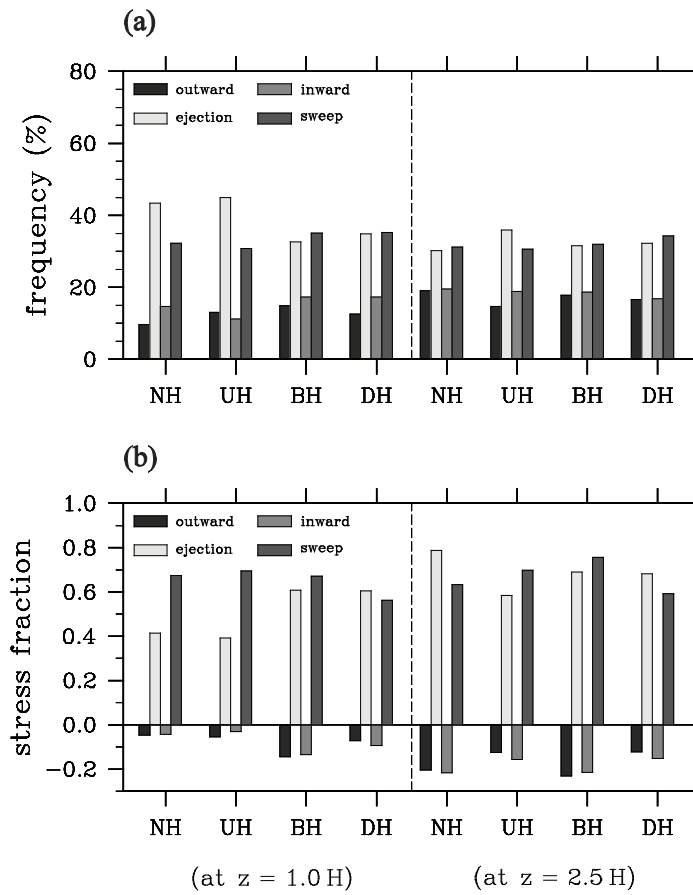


Figure 3.8. (a) Frequency  $T_i$  and (b) stress fraction  $S_i$  of the four quadrant events at  $(x, y, z) = (0, 0, H)$  and  $(0, 0, 2.5H)$ .

# 4 Turbulent flow in and above a heated building array

## 4.1 Experimental design

An idealized building array, which is composed of same-sized cubical buildings (20 m high), is considered (Fig. 4.1). The size of the computational domain is 480 m in the  $x$  direction, 480 m in the  $y$  direction, and 550 m in the  $z$  direction. The grid size in both the  $x$  and  $y$  directions is 1 m (much larger than the estimated Kolmogorov scale  $\sim 1$  mm). The grid size in the  $z$  direction is 1 m up to  $z = 100$  m and then gradually increases with an expansion ratio of 1.08. The cubical buildings are arranged in lines with a constant spacing of 20 m in both the  $x$  and  $y$  directions. Therefore, the plan area density of the building array is 25% and the aspect ratio of street canyon is one, with a skimming flow regime occurring in the building array (Macdonald et al. 1997).

Considering that the building arrays with the same geometry are repeated in both the  $x$  and  $y$  directions, the cyclic boundary condition is applied at the lateral boundaries for velocity components, SGS TKE, and temperature. The zero-gradient boundary condition is applied at the top boundary. The initial ambient wind blows in the  $x$  direction, and its vertical profile is logarithmic. Flow in the computational domain is driven by a constant external pressure

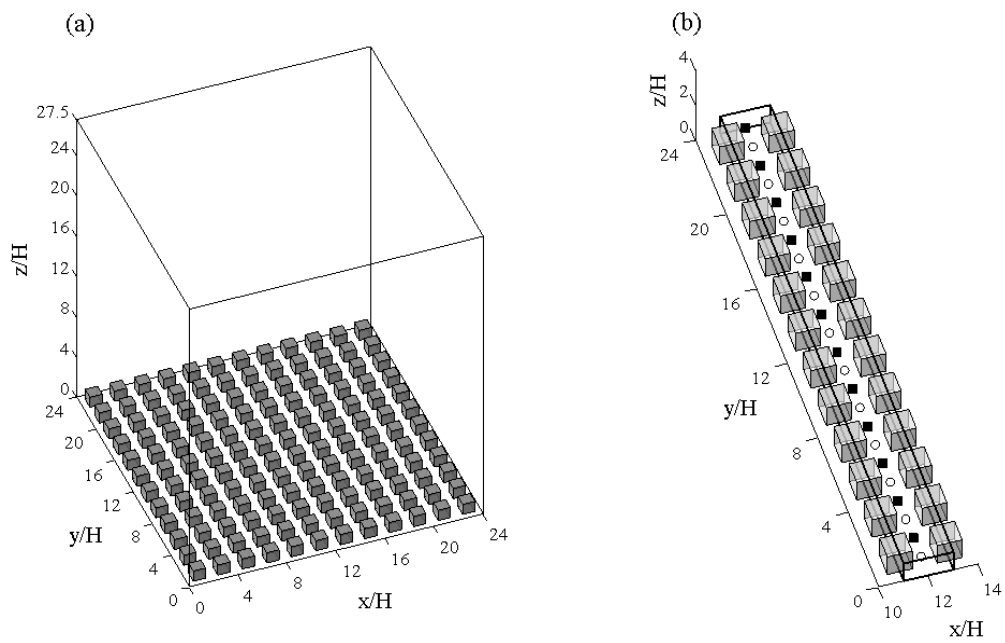


Figure 4.1. Illustrations of (a) the computational domain and building configuration and (b) the sampling points of the vertical profiles in Fig. 4.2.  $H$  is the building height.

gradient in the  $x$  direction ( $-0.001 \text{ Pa m}^{-1}$ ), and the Coriolis effect is not included here. At the grid points closest to all the solid surfaces, the MO similarity is employed in the momentum equation, thermodynamic energy equation, and passive scalar equation. Passive scalars are continuously emitted from all of the streets ( $5 \mu\text{g m}^{-2} \text{ s}^{-1}$ ), and the passive scalar concentration is set equal to zero at the inflow boundary. The results of scalar dispersion are presented in section 5.

Two simulations are conducted to investigate thermal effects on turbulent flow: no-heating (NH) case and street bottom-heating (BH) case. The temperature of the street bottom is set to be 10 K higher than that of the initial ambient air, and the bulk Richardson number in the BH case is  $-0.31$ . PALM is integrated for 4.5 h in the NH case, and the last 30-min simulation data are used for analysis. Then, PALM is integrated for 1 h more with the street bottom being heated. Also in the BH case, the last 30-min simulation data are analyzed.

## 4.2 Vertical profiles

Figure 4.2 shows the vertical profiles of 12 points-averaged mean streamwise velocity  $\bar{u}$ , vertical turbulent momentum flux  $\overline{u'w'}$ , root mean square (RMS) of streamwise velocity perturbation  $\sqrt{\overline{u'^2}}$ , and RMS of vertical velocity perturbation  $\sqrt{\overline{w'^2}}$ . Here,  $u'$  and  $w'$  denote deviations from the time-averaged

velocity components  $\bar{u}$  and  $\bar{w}$ , respectively. SGS parts are not included in the calculated turbulence statistics because their magnitudes are much smaller than the magnitudes of resolved parts. For example, the ratio of SGS TKE to resolved TKE is smaller than  $\sim 0.12$ . To investigate the positional dependency of turbulence statistics, we divide the space ( $11.5 \leq x/H \leq 12.5$ ,  $0 \leq y/H \leq 24$ ,  $0 \leq z/H \leq 1$ ) into cavity and intersection spaces and the vertical profiles averaged over the 12 cavity center (CC) points and those averaged over the 12 intersection center (IC) points (Fig. 4.1b) are compared in the NH and BH cases.

In the NH case, the vertical profiles of streamwise velocity over the CC and IC points have a logarithmic shape between  $z/H = 1.5$  and 5. In both the NH and BH cases, below  $z/H = 1.5$ , the streamwise velocity over the IC points increases almost linearly with height and that over the CC points increases from negative to positive values with an inflection point at  $z/H \sim 1$  (indicating a canyon vortex and a shear layer above the vortex). When compared with the NH case, flow just above the rooftop height ( $z/H = 1$ ) is slightly accelerated and that above  $z/H = 3$  is decelerated due to strengthened vertical mixing in the BH case. Bottom-heating effects are distinct in the vertical profiles of vertical turbulent momentum flux. Below  $z/H = 2$ , the magnitude of vertical turbulent momentum flux in the BH case is larger than that in the NH case over the CC and IC points. At the rooftop height, there are local peaks due to shear instability over the CC

points in both the NH and BH cases. Below the rooftop height, the difference in the magnitude of vertical turbulent momentum flux between the CC points and IC points is more pronounced than the difference between the NH and BH cases (Fig. 4.2b).

In both the NH and BH cases, the vertical profile of  $\sqrt{u'^2}$  averaged over the CC points has one peak at the rooftop height and that averaged over the IC points has two local peaks (one above the rooftop height and the other close to the bottom surface) (Fig. 4.2c). The vertical profiles of  $\sqrt{w'^2}$  illustrate distinct thermal effects. Below  $z/H = 2$  and above  $z/H = 4$ ,  $\sqrt{w'^2}$  in the BH case is larger than that in the NH case over the CC and IC points (Fig. 4.2d). While the difference below  $z/H = 2$  is attributed to the increased shear and buoyancy production of TKE in the BH case, the difference above  $z/H = 4$  is attributed to the existence of large-scale updrafts and downdrafts above the bottom-heated building array. In the BH case,  $\sqrt{w'^2}$  increases with height above  $z/H = 4$  and reaches its maximum at  $z/H \sim 15$  (a little higher than half the domain height). This is because large-scale vertical motions (comparable in size to the domain height) exist in the BH case, and they might affect flow structures in and above the building array.

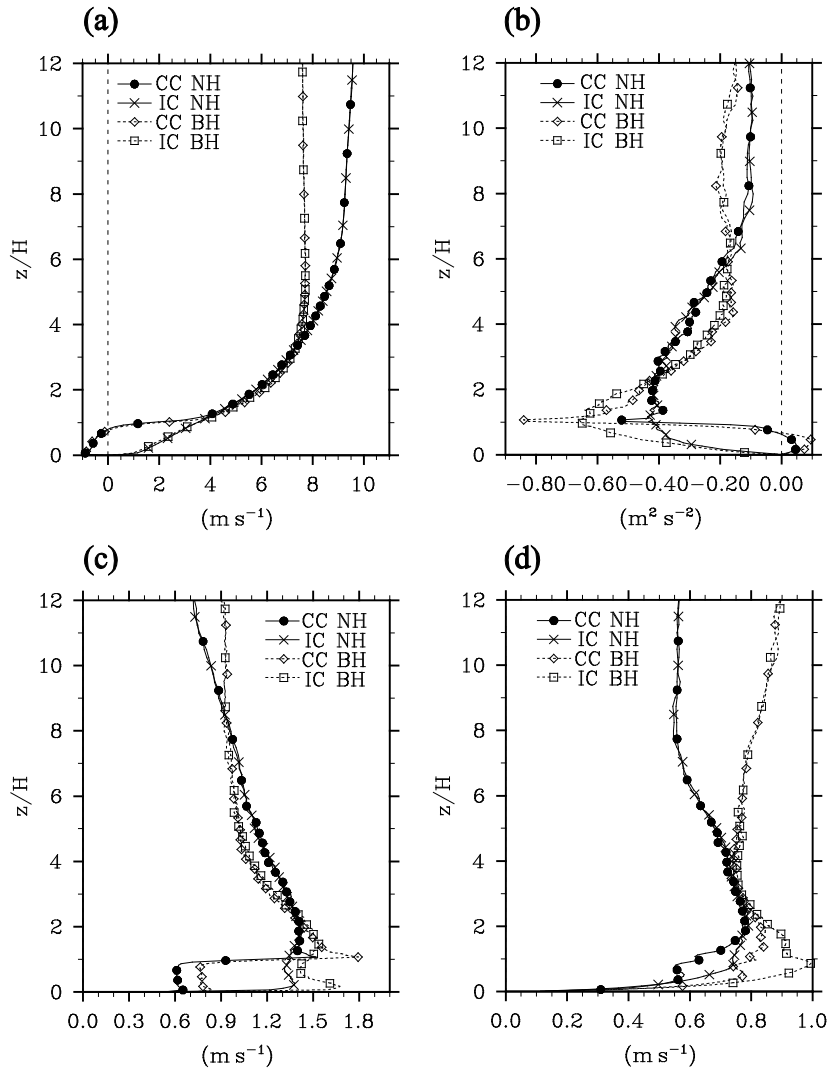


Figure 4.2. Vertical profiles of 12 points-averaged (a) mean streamwise velocity, (b) vertical turbulent momentum flux, (c) RMS of streamwise velocity perturbation, and (d) RMS of vertical velocity perturbation. Sampling points are marked as hollow circles for CC and marked as filled squares for IC in Fig. 4.1b.

### 4.3 Flow structures above a building array

Figure 4.3 shows the instantaneous fields of streamwise velocity and  $Q$  criterion at  $y/H = 15$  and  $t = 15480$  s in the NH case.  $Q$  criterion is defined as the second invariant of the velocity gradient tensor (or half the difference between squared rotation rate and squared strain rate) and a positive value of  $Q$  criterion is widely used for detecting vortical flow structures (Dubief and Delcayre 2000). The instantaneous field of streamwise velocity in the  $x$ - $z$  plane ( $y/H = 15$ ) shows the large-scale structures of streamwise velocity, while that of  $Q$  criterion shows small-scale vortical structures induced by buildings or turbulent flow itself (Figs. 4.3a,b). In the streamwise velocity field, two kinds of characteristic interfaces appear in the regions where the vertical gradient of streamwise velocity is large. One is a local shear layer between the air in the cavity spaces and the air outside the cavities. The other is the interface between low- and high-speed air above the building array. Across the interface between low- and high-speed air, sinking of high-speed air and bursting of low-speed air occur continuously at a variety of scales. Sinking and bursting at the interface induce small-scale vortical structures (Fig. 4.3c), and they even squeeze or lift the interface itself when they grow in scale. In fact, the interface can be divided into two parts depending on the slope of the interface in the  $x$ - $z$  plane. For example, part of the interface between  $x/H = 6.5$  and  $10.5$  is upslope and another part between  $x/H = 12.5$  and  $15$  is downslope.

While the sinking high-speed air squeezes low-speed air downstream across the upslope interface, the squeezed low-speed air and small-scale vortical structures in the squeezed low-speed air are burst upward, lifting the downslope interface and transporting momentum above the interface.

The turbulent motions related to the squeezing and lifting of the interface are repeated continuously in both the NH and BH cases, and this kind of turbulence coherent structure is similar to very large-scale motions reported by Kim and Adrian (1999), Guala et al. (2006), and Hutchins and Marusic (2007). Although the generation mechanism of the large-scale coherent structures has not been clarified, it is clear that they play an important role in momentum transport (Guala et al. 2006) and affect velocity and scalar fields below them (Marusic et al. 2010; Inagaki et al. 2012). The interface that effectively describes the large-scale turbulent motions can be identified by plotting the vertical gradient of streamwise velocity or simply by plotting streamwise velocity (Figs. 4.3a,b). The latter method is selected in this study, and the contours of equal streamwise velocity magnitude ( $5.5 \text{ m s}^{-1}$ ) successfully depict turbulence coherent structures above the building array.

To investigate the detailed structures of large-scale turbulent motions above the building array and their role in momentum transport, two analysis heights are selected:  $z/H = 1.2$  adjacent to the building tops and  $z/H = 3$  in the

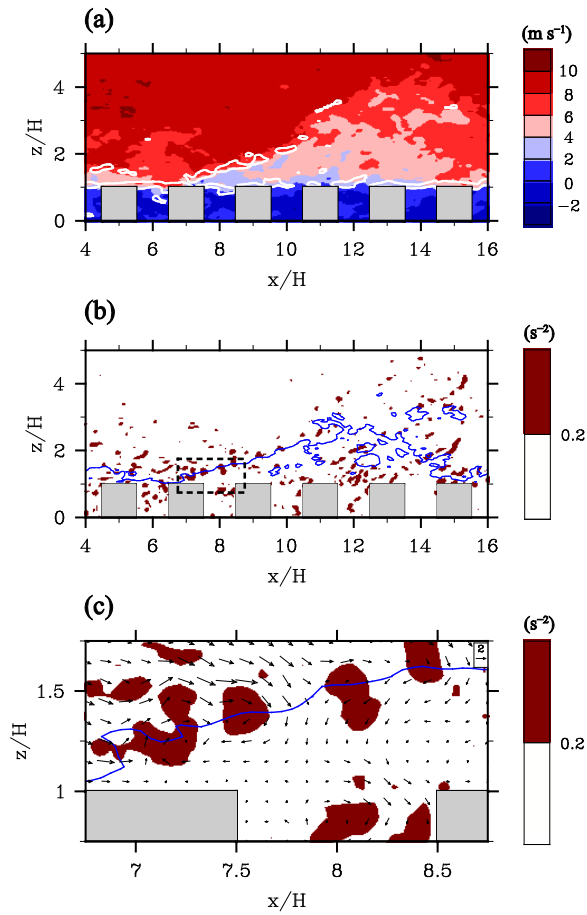


Figure 4.3. Instantaneous fields of (a) streamwise velocity, (b)  $\max(0, Q)$ , and (c)  $\max(0, Q)$  and velocity perturbation vector  $(u', w')$  in the  $x$ - $z$  plane ( $y/H = 15$ ) at  $t = 15480$  s in the NH case. The small rectangle in dashed lines is the region of (c). Contours of the vertical gradient of streamwise velocity ( $1.3 \text{ s}^{-1}$ ) are added in (a) and contours of streamwise velocity magnitude ( $5.5 \text{ m s}^{-1}$ ) are added in (b) and (c).

inertial sublayer where flow is weakly or not affected by each individual roughness element. Figure 4.4 shows the fields of  $\text{sgn}(w') \cdot \max(0, -u'w')$  at  $t = 15480$  s in the NH case and the same fields at  $t = 19080$  s in the BH case with equal streamwise velocity magnitude ( $5.5 \text{ m s}^{-1}$ ) being contoured. The  $\max(0, -u'w')$  returns the magnitude of  $u'w'$  only when  $u'w'$  is negative (when momentum is transported downward), and  $\text{sgn}(w')$  returns the sign of vertical velocity perturbation. Therefore, a positive value of  $\text{sgn}(w') \cdot \max(0, -u'w')$  indicates an ejection event (a combination of negative  $u'$  and positive  $w'$ ) and a negative value indicates a sweep event (a combination of positive  $u'$  and negative  $w'$ ) following a typical definition used in the quadrant analysis (Raupach 1981).

In both the NH and BH cases, the contours of equal streamwise velocity magnitude ( $5.5 \text{ m s}^{-1}$ ) represent the interfaces of low- and high-speed air. In the  $y$ - $z$  plane ( $x/H = 16$ ) in the NH case, ejections on the lifted parts of the interface and sweeps on the sunken parts of the interface are distinct (Fig. 4.4a). The lifted and sunken parts of the interface are represented by dotted regions at  $z/H = 3$  and hatched regions at  $z/H = 1.2$ , respectively (Figs. 4.4b,c). At  $z/H = 3$  and  $t = 15480$  s, the low-speed air lifted by successive ejections forms streamwise elongated low-speed regions (at  $y/H \sim 5$ ) and a group of low-speed streaks (at  $y/H \sim 17$ ) (Fig. 4.4b). Usually two or three, and sometimes one row of low-speed

flow structures appear and the spanwise scales of the rows are sensitive to the upper flow above  $z/H = 3$ . Actually, large-scale secondary circular flow covers the whole  $x$ - $y$  plane above  $z/H \sim 7$  (not shown) and it affects the relative magnitude of turbulent motions below it. Low-speed upper flow induces stronger ejections and wider low-speed regions at  $y/H \sim 5$  compared with the flow structures at  $y/H \sim 17$ . At  $z/H = 1.2$ , the high-speed air sunk by sweeps forms high-speed streaks and their spanwise scales are smaller than those at  $z/H = 3$  due to the influence of buildings (Fig. 5c). Some of the high-speed streaks penetrate into cavity and intersection spaces and affect flow therein. Above the building array, momentum is transported always downward by ejections and sweeps. Strong ejections and weaker sweeps transport momentum downward at  $z/H = 3$  (Fig. 4.4b), while strong sweeps and weaker ejections transport momentum downward at  $z/H = 1.2$  (Fig. 4.4c). Although the area occupied by ejections is smaller than the area occupied by sweeps at  $z/H = 3$ , the magnitude of vertical turbulent momentum flux by ejections ( $\overline{u'_- w'_+}$ ) is larger than that by sweeps ( $\overline{u'_+ w'_-}$ ) in the NH case, indicating the effectiveness of ejections in momentum transport at  $z/H = 3$  (Table 4.1). By contrast, the vertical turbulent momentum flux by sweeps and that by ejections are similar in magnitude at  $z/H = 1.2$  (Table 4.1).

At  $z/H = 3$  and  $t = 19080$  s in the BH case, there exist a streamwise-

elongated low-speed region at  $y/H \sim 1$  that expands vertically up to  $z/H = 5$  and several plume-shaped low-speed flow structures between  $y/H = 6$  and 20 (Figs. 4.4d,e). In the BH case, large-scale secondary circular flow (stronger than that in the NH case) dominates the whole model domain with updrafts intensified by bottom heating. In fact, this study mainly focuses on flow structures in the surface layer. Thus, the vertical scale of the simulated large secondary circular flow in the BH case might be limited by the model domain height and it could be smaller than the vertical scale of flow in a typical convective boundary layer (approximately inversion height). Although the thermal secondary circular flow is not fully simulated, characteristic features such as streamwise-elongated flow structures are well simulated. Above  $z/H \sim 2$ , the strengthened secondary circular flow induces low-speed regions ( $23 < y/H < 24$  and  $0 < y/H < 3$ ) and wide high-speed regions ( $4 < y/H < 20$ ) and the low- and high-speed regions are stable enough to be detected in the time-averaged fields. At  $z/H = 3$ , successive ejections occur in the existing low-speed regions, while ejections in the high-speed regions occur occasionally forming the plume-shaped low-speed flow structures (Fig. 4.4e). At  $z/H = 1.2$  in the BH case, ejections that are stronger and larger than those in the NH case appear with sweeps, and these ejections and sweeps together play an important role in momentum transport (Fig. 4.4f).

Compared with the NH case, it seems that stronger ejections appear in

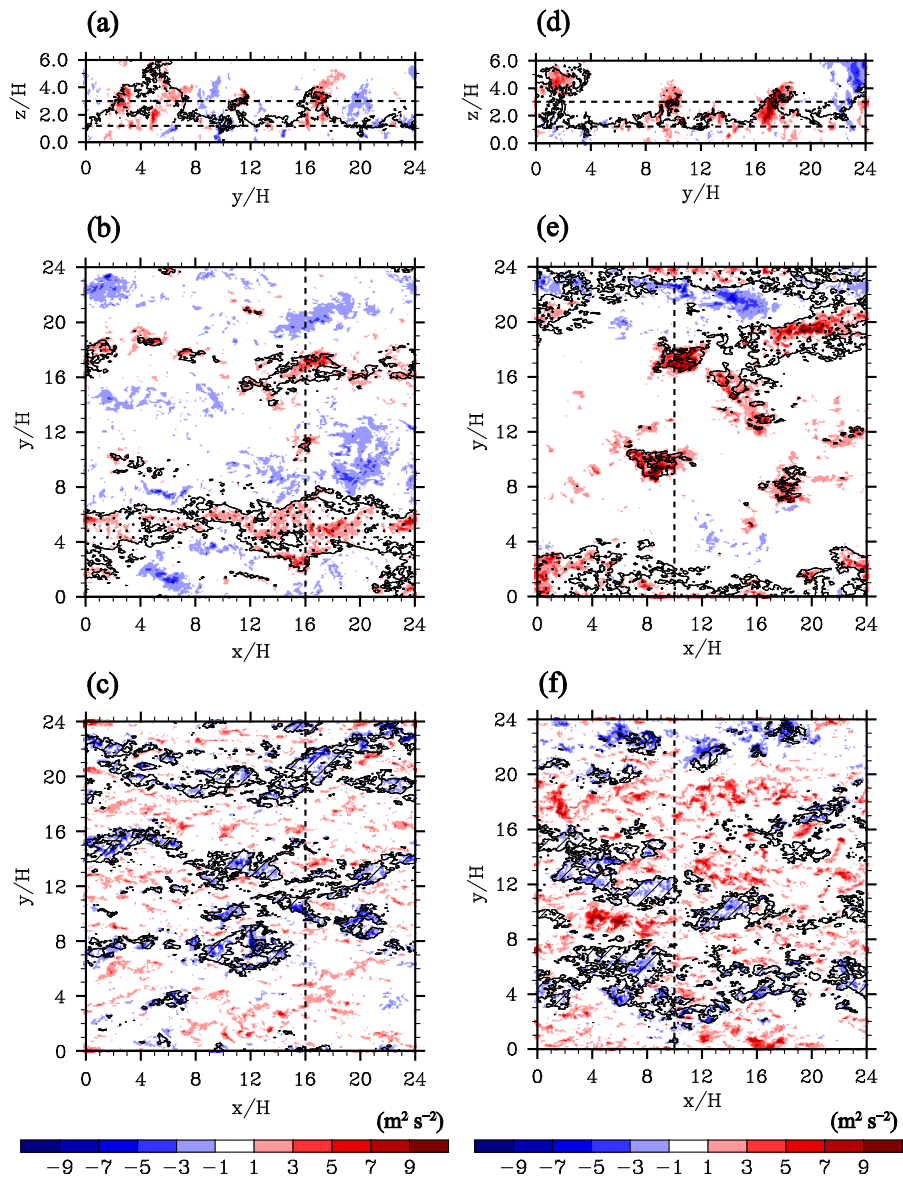


Figure 4.4. Instantaneous fields of  $\text{sgn}(w') \cdot \max(0, -u'w')$  with the contours of equal streamwise velocity ( $5.5 \text{ m s}^{-1}$ ) at  $t = 15480 \text{ s}$  in the (a)  $y$ - $z$  plane ( $x/H =$

16), (b)  $x$ - $y$  plane ( $z/H = 3$ ), and (c)  $x$ - $y$  plane ( $z/H = 1.2$ ) in the NH case and the same fields at  $t = 19080$  s in the (d)  $y$ - $z$  plane ( $x/H = 10$ ), (e)  $x$ - $y$  plane ( $z/H = 3$ ), and (f)  $x$ - $y$  plane ( $z/H = 1.2$ ) in the BH case.

Table 4.1. Areas occupied by low-speed regions (LSR) and high-speed regions (HSR) at  $z/H = 3$  and time- and area-averaged streamwise velocity, vertical velocity, vertical turbulent momentum flux, ratio of vertical turbulent momentum flux by ejections ( $u'_-w'_+$ ) to that by sweeps ( $u'_+w'_-$ ), and  $\max(0, Q)$  on the total horizontal domain, LSR, and HSR at  $z/H = 3, 1.2, 1,$  and  $0.5$  in the NH and BH cases. Overbars and angle brackets represent time-average and area-average, respectively.

| cases<br>region  | NH    |       |       | BH    |       |       |
|--|-------|-------|-------|-------|-------|-------|
|  | total | LSR   | HSR   | total | LSR   | HSR   |
| area (%)   | 100   | 30.8  | 33.3  | 100   | 23.9  | 35.8  |
| $\overline{\langle u \rangle}_{3H}$ (m s <sup>-1</sup> )                                   | 7.05  | 5.33  | 8.62  | 7.13  | 4.84  | 8.49  |
| $\overline{\langle w \rangle}_{3H}$ (m s <sup>-1</sup> )                                   | 0.00  | 0.35  | -0.32 | 0.00  | 0.71  | -0.33 |
| $\overline{\langle u'w' \rangle}_{3H}$ (m <sup>2</sup> s <sup>-2</sup> )                   | -0.37 | -0.60 | -0.47 | -0.32 | -0.83 | -0.18 |
| $\overline{\left( \frac{\langle u'_-w'_+ \rangle}{\langle u'_+w'_- \rangle} \right)_{3H}}$ | 1.11  | 92.14 | 0.01  | 1.47  | 16.92 | 0.04  |
| $\overline{\langle \max(0, Q) \rangle}_{3H}$ (s <sup>-2</sup> )                            | 0.03  | 0.04  | 0.03  | 0.03  | 0.06  | 0.02  |
| $\overline{\langle u \rangle}_{1.2H}$ (m s <sup>-1</sup> )                                 | 3.80  | 3.20  | 4.30  | 4.08  | 2.88  | 4.67  |
| $\overline{\langle w \rangle}_{1.2H}$ (m s <sup>-1</sup> )                                 | 0.00  | 0.06  | -0.05 | 0.00  | 0.16  | -0.06 |
| $\overline{\langle u'w' \rangle}_{1.2H}$ (m <sup>2</sup> s <sup>-2</sup> )                 | -0.42 | -0.36 | -0.48 | -0.60 | -0.58 | -0.61 |

|   |       |       |       |       |       |       |
|---|-------|-------|-------|-------|-------|-------|
| $\left(\overline{\langle u'_- w'_+ \rangle} / \overline{\langle u'_+ w'_- \rangle}\right)_{1.2H}$ | 0.98  | 2.27  | 0.55  | 1.07  | 2.03  | 0.82  |
| $\overline{\langle \max(0, Q) \rangle}_{1.2H} (\text{s}^{-2})$                                    | 0.08  | 0.07  | 0.09  | 0.10  | 0.09  | 0.11  |
| $\overline{\langle u \rangle}_H (\text{m s}^{-1})$  | 2.58  | 2.16  | 2.92  | 2.70  | 1.85  | 3.11  |
| $\overline{\langle w \rangle}_H (\text{m s}^{-1})$  | 0.00  | 0.04  | -0.05 | 0.00  | 0.15  | -0.06 |
| $\overline{\langle u' w' \rangle}_H (\text{m}^2 \text{s}^{-2})$                                   | -0.40 | -0.35 | -0.45 | -0.63 | -0.58 | -0.63 |
| $\left(\overline{\langle u'_- w'_+ \rangle} / \overline{\langle u'_+ w'_- \rangle}\right)_H$      | 0.80  | 1.55  | 0.50  | 0.85  | 1.39  | 0.71  |
| $\overline{\langle \max(0, Q) \rangle}_H (\text{s}^{-2})$   | 0.09  | 0.07  | 0.10  | 0.12  | 0.10  | 0.13  |
| $\overline{\langle u \rangle}_{0.5H} (\text{m s}^{-1})$   | 1.32  | 1.05  | 1.53  | 1.26  | 0.66  | 1.58  |
| $\overline{\langle w \rangle}_{0.5H} (\text{m s}^{-1})$   | 0.00  | 0.02  | -0.02 | 0.00  | 0.09  | -0.03 |
| $\overline{\langle u' w' \rangle}_{0.5H} (\text{m}^2 \text{s}^{-2})$                              | -0.15 | -0.14 | -0.16 | -0.22 | -0.21 | -0.21 |
| $\left(\overline{\langle u'_- w'_+ \rangle} / \overline{\langle u'_+ w'_- \rangle}\right)_{0.5H}$ | 0.88  | 1.48  | 0.62  | 0.94  | 1.28  | 0.82  |
| $\overline{\langle \max(0, Q) \rangle}_{0.5H} (\text{s}^{-2})$                                    | 0.06  | 0.05  | 0.07  | 0.09  | 0.08  | 0.10  |

shrinking low-speed regions in the  $x$ - $y$  plane ( $z/H = 3$ ) in the BH case (Fig. 4.4e). This feature is quantified by comparing areas occupied by newly defined low-speed regions ( $u < \bar{u} - \sqrt{u'^2}$ ) and high-speed regions ( $u > \bar{u} + \sqrt{u'^2}$ ) at  $z/H = 3$  and by comparing vertical turbulent momentum fluxes averaged over the low- and high-speed regions for each case (Table 4.1). In the NH case, the area of low-speed regions is similar to that of high-speed regions and the magnitude of the averaged vertical turbulent momentum flux in the low-speed regions is larger than that in the high-speed regions. In the BH case, however, the area of low-speed regions is smaller than that of high-speed regions by 11.9% and the magnitude of the averaged vertical turbulent momentum flux in the low-speed regions is 4.6 times larger than that in the high-speed regions. This indicates that more momentum is transported through shrunken low-speed regions over the bottom-heated building array than in the NH case. Furthermore, the magnitude of the averaged vertical velocity in the low-speed regions increases by more than 2 times and that of the averaged streamwise velocity in the low-speed regions decreases significantly relative to the NH case (Table 4.1), highlighting the importance of low-speed flow structures in the BH case.

Figure 4.5 shows the fields of joint probability density of  $u'$  and  $w'$  and  $u'w'$  multiplied by the joint probability density at  $z/H = 3$  in the NH and BH cases. The joint probability density of  $u'$  and  $w'$  is calculated using the expression

$f_{u',w'}(a_i, a_j) = P(a_i - 0.5\Delta a < u' \leq a_i + 0.5\Delta a, a_j - 0.5\Delta a < w' \leq a_j + 0.5\Delta a)$ . The number in each direction  $N$  and spacing  $\Delta a$  of bins used to calculate the joint probability distribution are 50 and 0.2, respectively, and the sum of all joint probability densities  $\sum_{i=1}^N \sum_{j=1}^N f_{u',w'}(a_i, a_j)$  is 1. The joint probability density and  $u'w'$  multiplied by the joint probability density can easily illustrate the frequency of turbulent events ( $u', w'$ ) and their contribution to vertical turbulent momentum flux, respectively. In the NH case, ejections and sweeps are comparable in frequency. However, strong ejections ( $u'w' < -2.5 \text{ m}^2 \text{ s}^{-2}$ ) occur a little more frequently than strong sweeps, resulting in more contribution of ejections to vertical turbulent momentum flux. In the BH case, weak turbulent events (close to the origin in the  $u'-w'$  plane) occur more frequently than in the NH case and strong turbulent events are concentrated in the second quadrant (ejection). The thermally affected joint probability density distribution in the BH case induces more contribution to vertical turbulent momentum flux by ejections (Fig. 4.5d). As the height approaches  $z/H = 1$ , the joint probability density distribution becomes similar to that at  $z/H = 3$  in the NH case (Fig. 4.5a) and the difference between the NH and BH cases becomes smaller (not shown).

To examine the essential flow structures of large-scale turbulent motions such as low-speed streaks, conditionally averaged fields of streamwise velocity perturbation and velocity vector are plotted in Fig. 7. Conditional averages are

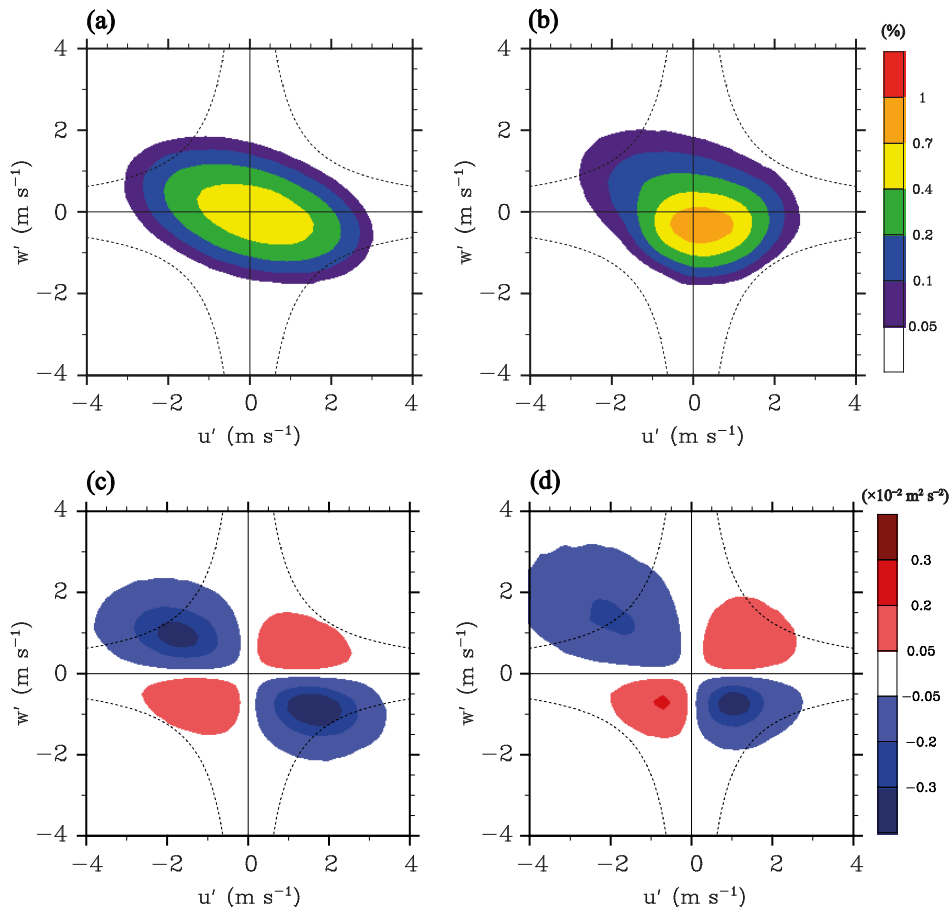


Figure 4.5. Fields of the joint probability density of  $u'$  and  $w'$  in the (a) NH and (b) BH cases and  $u'w'$  multiplied by the joint probability density in the (c) NH and (d) BH cases at  $z/H = 3$ . Dashed lines of equal  $|u'w'|$  ( $2.5 \text{ m}^2 \text{ s}^{-2}$ ) are added.

obtained using the following steps. First, local minimum points of  $u'w'$  in the regions satisfying a certain criterion (e.g.,  $u'w' < -2.5 \text{ m}^2 \text{ s}^{-2}$ ) are identified in the  $x$ - $y$  plane ( $z/H = 3$ ). Then, the three-dimensional data of a target variable are transformed to a coordinate  $(x', y', z)$  centered on each minimum point and the transformed data are collected. The identifying and collecting steps are repeated for successive instants. Finally, the collected three-dimensional data are averaged. Here, we apply the criterion based on the magnitude of turbulent momentum flux to extract the essential structures that are important to momentum transport. The criterion can be changed depending on the objective of conditional averaging. For all the velocity vector plots, conditionally averaged  $u'$  is used instead of  $u$  to emphasize the relative motion of coherent structures with respect to mean flow.

The conditionally averaged fields show the elliptical structures of negative streamwise velocity perturbation with low-pressure perturbation (represented by the contours in Fig. 4.6). In the NH case, the obtained elliptical structure is composed of low-speed and upward turbulent motions, indicating the dominance of ejections above the building array. The contours of low-pressure perturbation in Fig. 4.6 represent vortices (mostly streamwise vortices) around low-speed flow structures in the instantaneous flow fields (not shown), and their shape in the conditionally averaged fields resembles hairpin vortices (Adrian et al. 2000; Coceal et al. 2007). Although a positive  $Q$  criterion is known to be

more accurate for detecting small-scale vortical structures than low-pressure perturbation (Dubief and Delcayre 2000), low-pressure perturbation is used for plotting vortices because  $Q$  criterion cannot illustrate vortical structures larger than the building height. Actually, streamwise vortices frequently appear in and above the building array in the instantaneous pressure fields (not shown) and they play an important role in inducing strong ejections. The newly ejected low-speed air (by the streamwise vortices) forms low-speed streaks next to the existing low-speed flow structures, resulting in the horizontal meandering of low-speed regions in the NH case (Fig. 4.4b). However, the interaction of the streamwise vortices with turbulent motions in and above the building array is still not completely understood.

In the BH case, the magnitudes of velocity perturbation in the  $x$ - and  $z$ -direction increases and  $y$ -direction motions toward the center line ( $y/H = 0$ ) strengthen (Figs. 4.6d–f). The shape of conditionally averaged low-pressure perturbation in the BH case is different from that in the NH case. The head part of the hairpin vortex-like structure is expanded vertically, possibly because of ascending thermal plumes. In the instantaneous pressure fields in the BH case, more vertically slanted vortices are observed (not shown) and they are closely related to the plume-shaped low-speed flow structures (Fig. 4.4e). When compared with the NH case, bottom heating strengthens low-speed flow

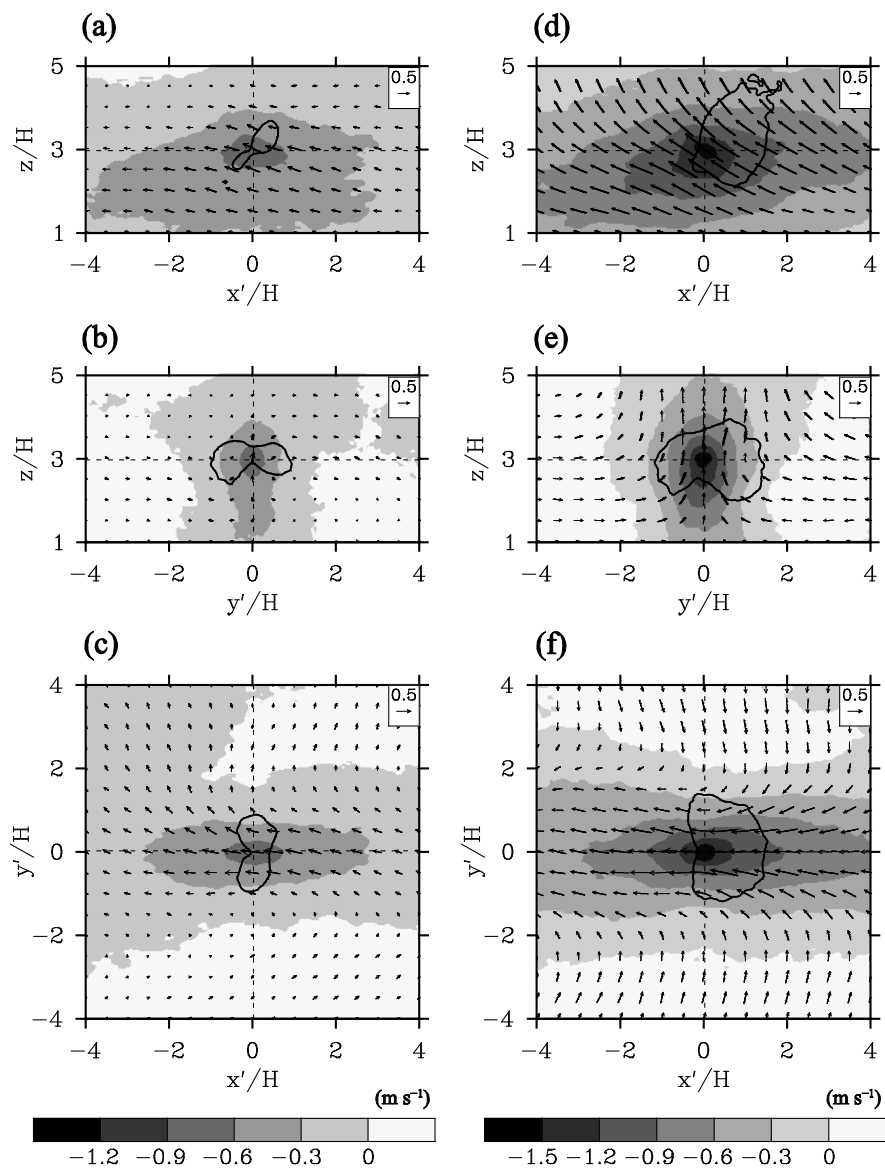


Figure 4.6. Conditionally averaged  $u'$  and velocity vector fields in the (a), (d)  $x'$ - $z$  plane ( $y'/H = 0$ ), (b), (e)  $y'$ - $z$  plane ( $x'/H = 0$ ), and (c), (f)  $x'$ - $y'$  plane ( $z/H = 3$ )

in the (left) NH case and (right) BH case. Conditionally averaged  $u'$  instead of  $u$  is used for plotting velocity vector fields, and the contours of equal conditionally averaged pressure perturbation ( $-1$  Pa in the NH case and  $-1.5$  Pa in the BH case) are added.

structures much above the building array (Fig. 4.6). The mean flow above  $z/H = 3$  is weaker in the BH case than in the NH case (Fig. 4.2a).

## 4.4 Flow structures in a building array

Figure 4.7 shows vertical turbulent momentum flux ( $\overline{u'w'}$ ) fields spanwise averaged over the 12  $x$ - $z$  cross sections containing the CC points, those containing the IC points, and the 12 CC-centered subregions at the rooftop height in the NH case. In the NH case, a shear layer develops around the tops of cavity spaces and the shear layer can be identified by the vertical gradient of shear production (Salizzoni et al. 2011). In the  $x$ - $z$  cross sections containing the CC points, the vertical gradient of shear production is calculated and contours of absolute value  $0.06 \text{ m s}^{-3}$  are plotted in Fig. 4.7a. Going downstream from the upper corner of upwind buildings, the shear layer develops and its thickness reaches a maximum in front of downwind buildings. Near the upper corner of downwind buildings, the shear layer tends to develop downward following the primary vortex in the cavity spaces. In and around the shear layer, turbulent eddies generated by the upwind buildings or by flow structures passing over the building array grow and strengthen as they move downstream. Consequently, the maximum  $\overline{u'w'}$  appears near the upper corner of downwind buildings (Figs.

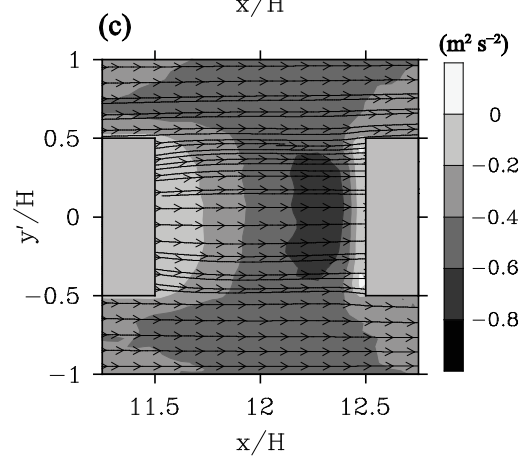
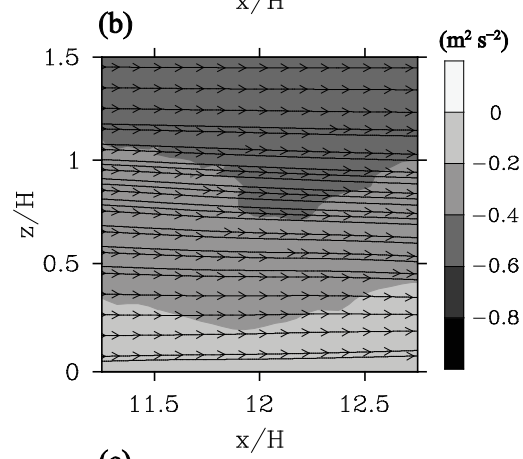
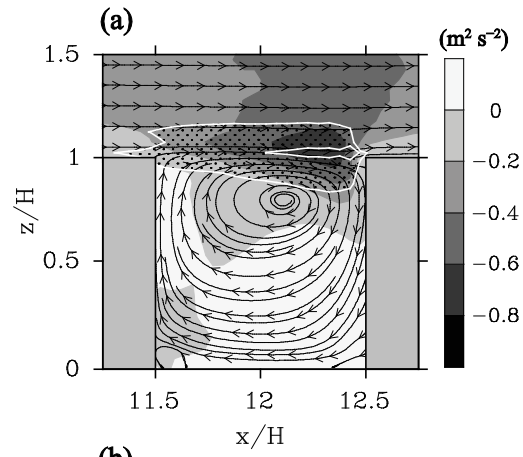


Figure 4.7. Vertical turbulent momentum flux ( $\overline{u'w'}$ ) fields spanwise averaged over (a) the 12  $x$ - $z$  cross sections containing the CC points, (b) those containing the IC points, and (c) the 12 CC points-centered subregions at  $z/H = 1$  (Fig. 1b) in the NH case. Contours of equal absolute value of the vertical gradient of shear production of turbulent kinetic energy ( $0.06 \text{ m s}^{-3}$ ) are added in (a). The dotted region in (a) indicates the region where the absolute value of the vertical gradient of shear production of turbulent kinetic energy is  $> 0.06 \text{ m s}^{-3}$ . Streamlines are also plotted.

4.7a,c). In the  $x$ - $z$  cross sections containing the IC points, the shear layer is not detected and the magnitude of  $\overline{u'w'}$  increases with height (Fig. 4.7b). This indicates that turbulent flow in the intersection spaces is closely related to the upper turbulent flow structures such as high-speed streaks.

Figure 4.8 shows streamwise velocity perturbation and velocity vector fields conditionally averaged over the tops of cavity spaces and those over the tops of intersection spaces in the NH case. Compared with the conditionally averaged fields at  $z/H = 3$ , sweeps are dominant at the rooftop height and their horizontal size is much smaller than that at  $z/H = 3$  in the NH case. At the tops of cavities, the structure of sweeps is circular in the  $x'$ - $y'$  plane and elliptical in the  $x'$ - $z$  and  $y'$ - $z$  planes, indicating a flat-disk shape in a three-dimensional space. At the tops of intersections, however, the structure of sweeps is streamwise elongated in the  $x'$ - $y'$  plane and the magnitude of streamwise velocity perturbation decreases compared with that at the tops of cavities. Sweep-dominant structures have also been found over plant canopies (Fitzmaurice et al. 2004; Watanabe 2004) although the detailed shape of the structures is different due to the difference in the criteria used for conditional averaging. As shown in Fig. 4.8, velocity fluctuations (represented by low-pressure perturbations) above the cavity spaces and those in and above the intersection spaces tend to appear upstream of the point  $(x', y', z) = (0, 0, H)$  because the structures induce sweeps

on their downstream sides. In the cavity spaces, vortex flow structures (also represented by low-pressure perturbations) appear and they are connected to the velocity fluctuations passing over the cavity spaces (Fig. 9a). This kind of connected structures might lead to the strong vertical turbulent momentum flux in front of downwind buildings (Figs. 4.7a,c). As in the NH case, same turbulence coherent structures with a flat-disk shape at the tops of cavity spaces and a streamwise-elongated shape at the tops of intersection spaces appear in the BH case due to the dominant influence of buildings at the rooftop height (not shown).

Figure 4.9 shows vertical turbulent momentum flux ( $\overline{u'w'}$ ) field spanwise averaged over the 12  $x$ - $z$  cross sections containing the CC points and correlation coefficient field of temperature and  $u'w'$  averaged over the same cross sections in the BH case. In the  $x$ - $z$  cross sections containing the CC points, bottom heating induces stronger vertical turbulent momentum flux and the shear layer becomes thicker (Fig. 4.9a) due to the increase of shear production there when compared with the NH case (Fig. 4.7a). As shown in Fig. 4.9b, the vertical turbulent momentum flux and temperature are well correlated in and around the shear layer, but the signs of correlation coefficients are opposite depending on the height. The correlation coefficient is negative in the upper part of the shear layer and positive in the lower part of the shear layer. Judging from the fact that

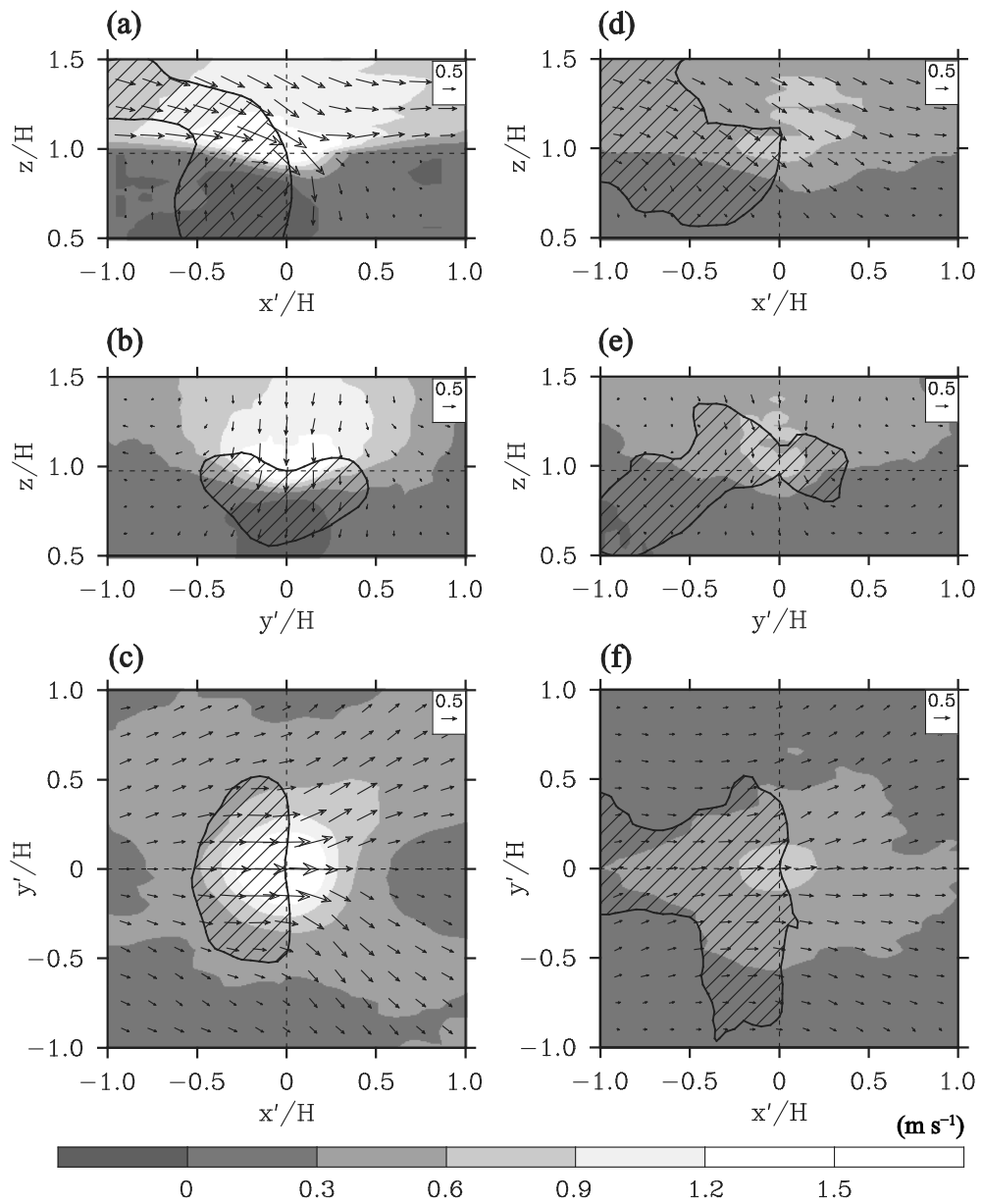


Figure 4.8. The  $u'$  and velocity vector fields in the (a)  $x'-z$  plane ( $y'/H = 0$ ), (b)  $y'-z$  plane ( $x'/H = 0$ ), and (c)  $x'-y'$  plane ( $z/H = 3$ ) conditionally averaged at the tops of the cavity spaces, and the same fields in the (d)  $x'-z$  plane ( $y'/H = 0$ ), (e)  $y'-z$  plane ( $x'/H = 0$ ), and (f)  $x'-y'$  plane ( $z/H = 3$ ) conditionally averaged at the tops of the intersection spaces in the NH case. Conditionally averaged  $u'$  instead of  $u$  is used for plotting velocity vector fields, and the contours of equal conditionally averaged pressure perturbation ( $-0.95$  Pa) are added. The hatched areas indicate the regions where conditionally averaged pressure perturbation is lower than  $-0.95$  Pa.

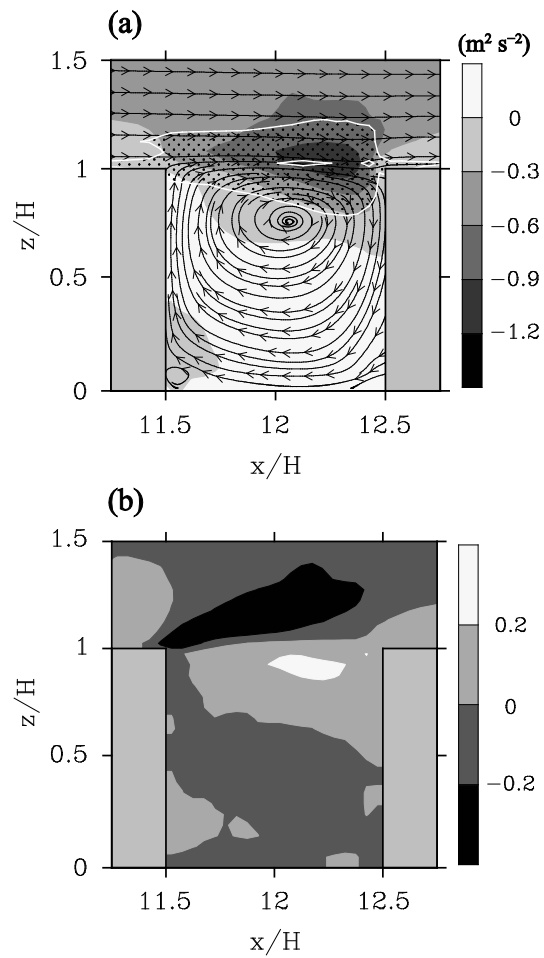


Figure 4.9. Fields of (a) vertical turbulent momentum flux ( $\overline{u'w'}$ ) spanwise averaged over the 12  $x$ - $z$  cross sections containing the CC points and (b) correlation coefficient of temperature and  $u'w'$  averaged over the same cross sections in the BH case. Streamlines and contours of equal absolute value of the vertical gradient of shear production of turbulent kinetic energy ( $0.06 \text{ m s}^{-3}$ ) are

added in (a). The dotted region in (a) indicates the region where the absolute value of the vertical gradient of shear production of turbulent kinetic energy is larger than  $0.06 \text{ m s}^{-3}$ .

the common turbulent events in the upper and lower parts of the shear layer are the bursting of cavity air (high-temperature perturbation) and the entrainment of ambient air (low-temperature perturbation), the negative and positive correlation coefficients are closely related to ejections in the upper part of the shear layer and sweeps in the lower part of the shear layer. In fact, both ejections and sweeps in the BH case have larger magnitudes than those in the NH case, resulting in stronger vertical turbulent momentum flux in the shear layer (Fig. 4.9a).

Figure 4.10 shows vertical turbulent momentum flux ( $\overline{u'w'}$ ) and spanwise turbulent momentum flux ( $\overline{u'v'}$ ) fields spanwise averaged over the 12 CC-centered subregions at  $z/H = 0.5$  in the NH case. The magnitude of vertical turbulent momentum flux is larger in the intersection spaces than in the cavity spaces because the high-speed upper air occasionally penetrates into the intersection spaces, transporting momentum downward. In the cavity spaces, however, the vortical flow structures such as a primary vortex in the  $x$ - $z$  plane (Fig. 4.7a) and a double-eddy circulation in the  $x$ - $y$  plane at  $z/H = 0.5$  (Fig. 4.10) interrupt the deep penetration of the high-speed upper air, resulting in weakly downward or upward turbulent transport of momentum. Spanwise turbulent motions appear around the boundaries between the cavity and intersection spaces, leading to strong spanwise turbulent momentum flux there (Fig. 4.10b). In the BH case, similar vertical and spanwise turbulent momentum flux fields appear at

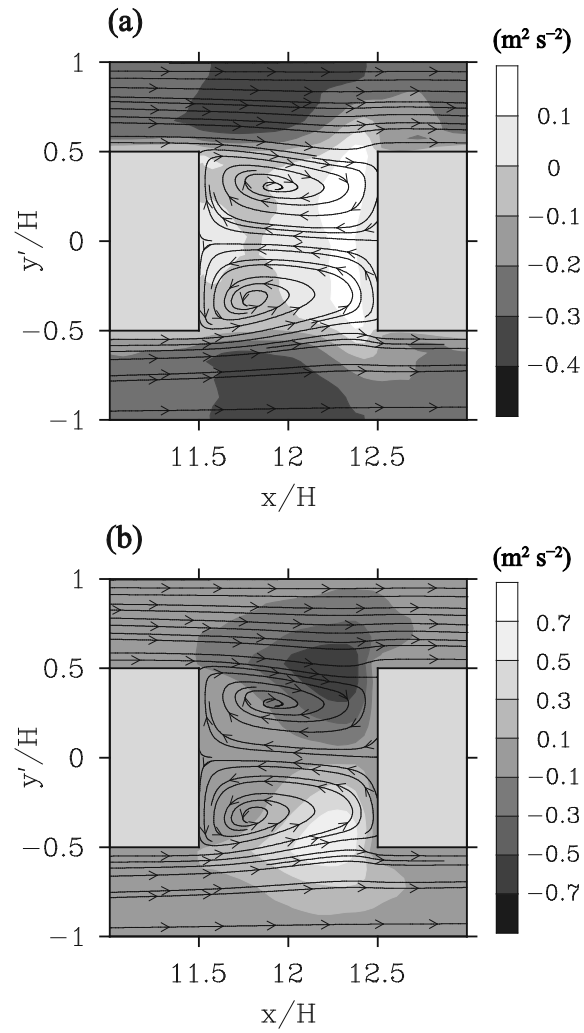


Figure 4.10. Fields of (a) vertical turbulent momentum flux  $(\overline{u'w'})$  and (b) spanwise turbulent momentum flux  $(\overline{u'v'})$  spanwise averaged over the 12 CC-centered subregions at  $z/H = 0.5$  in the NH case. Streamlines are also plotted.

$z/H = 0.5$ , indicating the momentum transport from above the rooftop height into the cavity spaces.

Streamwise velocity perturbation and velocity vector fields with the contours of equal vertical velocity ( $-0.23 \text{ m s}^{-1}$ ), all conditionally averaged at  $z/H = 0.5$  in the intersection spaces, are shown in Fig. 4.11. In both the NH and BH cases, the structure that is composed of positive streamwise velocity perturbation and downdraft ( $w < -0.23 \text{ m s}^{-1}$ ) appears with spanwise diverging flow. This again indicates that the high-speed upper air comes into the intersection spaces and induces spanwise motions heading for nearby cavity spaces. The structure of positive streamwise velocity perturbation in the NH case has a more elongated shape and larger magnitude than that in the BH case. As indicated by the contours around  $(x', y') = (0.5, -1.0)$  or  $(0.5, 1.0)$  (corresponding to the spaces in front of downwind buildings) in Fig. 4.11, sweeps tend to appear in the intersection spaces with downdrafts in the nearby cavity spaces in both cases. This is because overlying high-speed streaks (larger than the building height) induce sweeps in the intersection spaces and the streaks simultaneously induce downdrafts in the nearby cavity spaces.

As shown in Table 4.1, the magnitude of area-averaged vertical turbulent momentum flux at  $z/H = 1$  and  $1.2$  below the high-speed regions (defined at  $z/H = 3$ ) is larger than that below the low-speed regions in both the NH and BH cases,

and the signs of area-averaged vertical velocity are negative and positive below the high- and low-speed regions, respectively. Moreover, the time- and area-averaged  $\max(0, Q)$  at  $z/H = 1$  and  $1.2$  below the high-speed regions is larger than that below the low-speed regions in both the NH and BH cases. The averaged value of  $\max(0, Q)$  returns the averaged intensity of small-scale vortical structures, and it is closely related to the number of small-scale vortical structures. Thus, the larger magnitude of time- and area-averaged  $\max(0, Q)$  below the high-speed regions indicates that more small-scale vortical structures exist below the high-speed regions than below the low-speed regions. This implies that high-speed streaks passing over the building array induce downward-tilted flow impinging on buildings and more small-scale vortical structures appear around the buildings, leading to the stronger vertical turbulent momentum flux below the high-speed regions. On the contrary, low-speed streaks seem to induce updrafts and fewer small-scale structures below them in the building array. These findings are consistent with the conceptual model of turbulent flow over a flat plate (Marusic et al. 2010).

In contrast to the intersection spaces, the magnitude of vertical turbulent momentum flux in the cavity spaces is quite small. Therefore, conditionally averaged fields using the criterion based on turbulent kinetic energy are investigated. The conditionally averaged fields show a typical canyon vortex in

the  $x'-z$  plane and a double-eddy circulation in the  $x'-y'$  plane at  $z/H = 0.5$  (not shown), commonly observed in time-averaged velocity vector fields in a building array (Santiago et al. 2007).

Figure 4.12 shows the vertical profiles of 12 points-averaged streamwise length scale of streamwise velocity, spanwise length scale of spanwise velocity, and streamwise length scale of vertical velocity over the IC points in the NH and BH cases. All length scales are obtained by calculating maximum streamwise (or spanwise) distance between the points where the correlation coefficient of each variable is 0.5. The streamwise length scale of streamwise velocity increases with height above the rooftop height in both cases. Below  $z/H = 3$ , the streamwise length scale of streamwise velocity in the BH case is smaller than that in the NH case, indicating that bottom heating obstructs the passage of high-speed streaks. This corresponds to the shortened high-speed streaks in the BH case (Fig. 4.11b). The spanwise length scale of spanwise velocity below the rooftop height in the BH case is larger than that in the NH case. This indicates that bottom heating induces stronger spanwise motions in the building array. The streamwise (also spanwise) length scale of vertical velocity does not show any noticeable difference between the NH and BH cases.

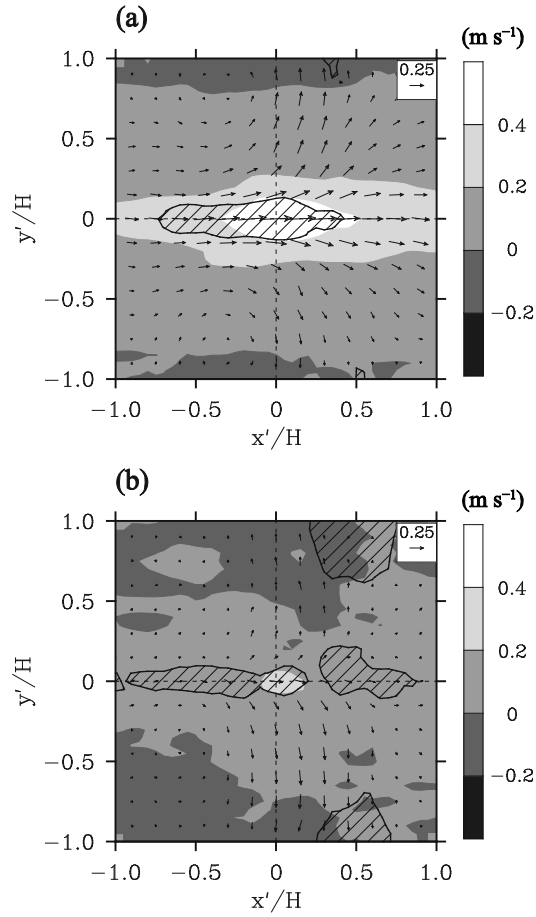


Figure 4.11. Streamwise velocity perturbation and velocity vector fields in the  $x'$ - $y'$  plane ( $z/H = 0.5$ ) conditionally averaged at  $z/H = 0.5$  in the intersection spaces in the (a) NH and (b) BH cases. Conditionally averaged  $u'$  instead of  $u$  is used for plotting velocity vector fields and the contours of equal conditionally averaged vertical velocity ( $-0.23 \text{ m s}^{-1}$ ) are added. The hatched areas indicate the regions where conditionally averaged downward vertical velocity is higher than  $0.23 \text{ m s}^{-1}$ .

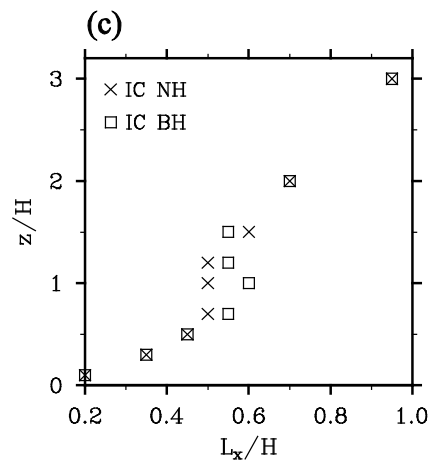
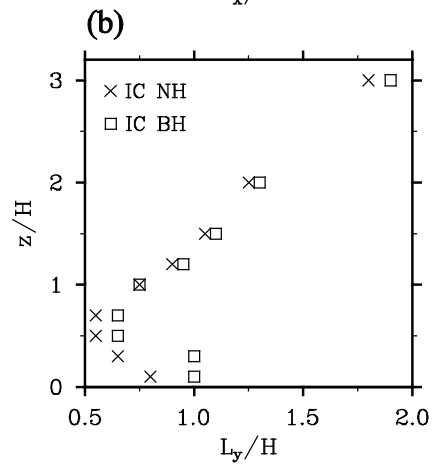
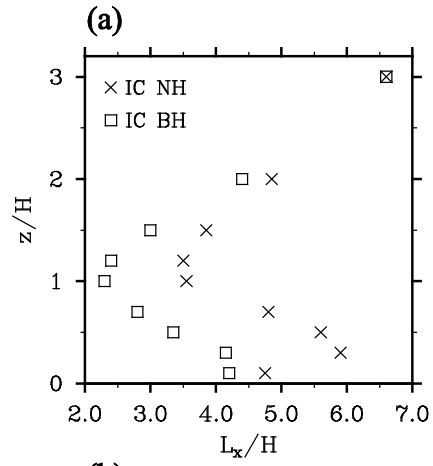


Figure 4.12. Vertical profiles of 12 points-averaged (a) streamwise length scale of streamwise velocity, (b) spanwise length scale of spanwise velocity, and (c) streamwise length scale of vertical velocity over the IC points in the NH and BH cases.

As shown in Fig. 4.11, high-speed streaks from above the building array induce spanwise flow in the building array. Actually, the spanwise range affected by the overlying turbulent flow structures is larger than the building height and sometimes equal to the horizontal domain size depending on the stability. Figure 4.13 shows time-averaged spanwise velocity fields at  $z/H = 0.1$  with the contours of equal streamwise velocity magnitude at  $z/H = 3$  and those at  $z/H = 1.2$  in the NH and BH cases. Dotted regions indicate the low-speed streaks or low-speed regions in the time-averaged streamwise velocity fields at  $z/H = 3$ , and hatched regions indicate the high-speed streaks in the time-averaged streamwise velocity fields at  $z/H = 1.2$ . In the NH case, high-speed regions ( $\bar{u} > 4.4 \text{ m s}^{-1}$  at  $z/H = 1.2$ ) and one low-speed region ( $\bar{u} < 6.0 \text{ m s}^{-1}$  at  $z/H = 3$ ) above the building array induce spanwise diverging and converging flow at  $z/H = 0.1$ , respectively (Fig. 14a). In fact, one more converging flow structure related to another low-speed region above the building array exists at  $y/H \sim 16$ , but this region is only detected by using a looser criterion (e.g.,  $\bar{u} = 7.5 \text{ m s}^{-1}$ ). In the NH case, the combination of low- and high-speed flow structures induces spanwise flow in the building array (detectable even in the time-averaged fields). In the BH case in which large-scale secondary circular flow dominates the whole model domain, one spanwise converging flow centered at  $y/H = 23$  develops in the building array. The spanwise converging flow in the BH case is stronger than that in the

NH case, and it corresponds to the lower part of the secondary circular flow intensified by thermal updrafts. This thermally well organized flow structure induces much stronger updrafts and much slower streamwise flow below the low-speed regions deep in the building array ( $z/H = 0.1$ ) than low-speed flow structures in the NH case (Table 4.1). It is also noticeable that low-speed regions are centered over the building and cavity spaces and high-speed regions are centered over the streamwise-directed streets in both the NH and BH cases.

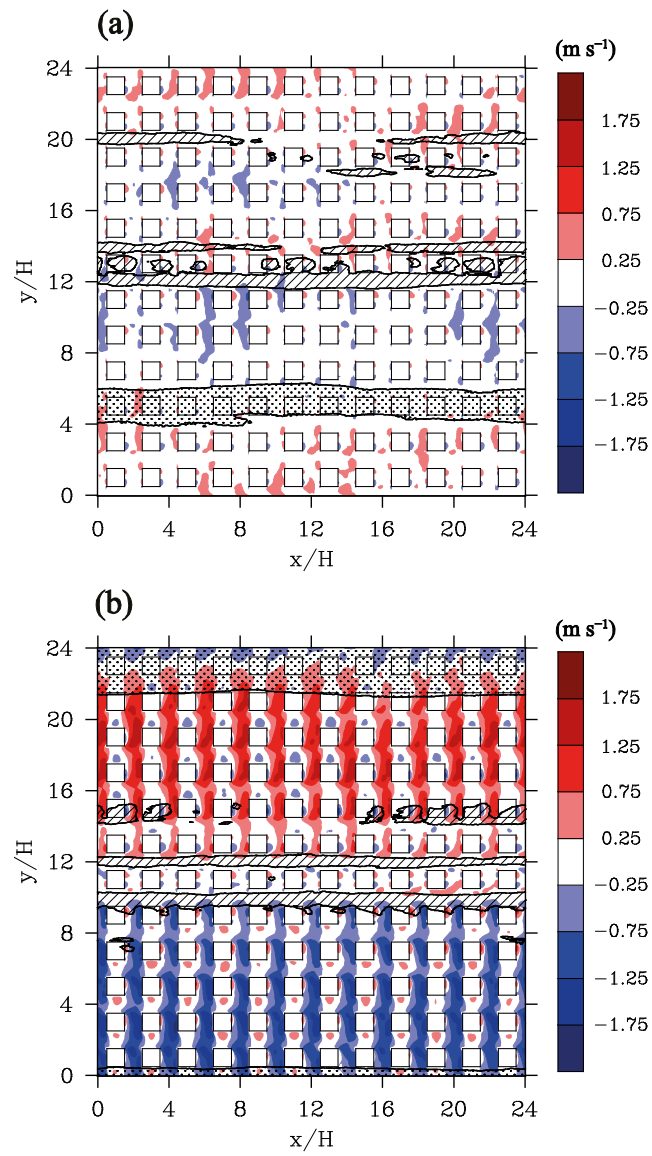


Figure 4.13. Time-averaged spanwise velocity fields at  $z/H = 0.1$  and the contours of equal streamwise velocity magnitude ( $6.0 \text{ m s}^{-1}$  in the NH case and

5.5 m s<sup>-1</sup> in the BH case) at  $z/H = 3$  and the contours of equal streamwise velocity magnitude (4.4 m s<sup>-1</sup> in the NH case and 4.9 m s<sup>-1</sup> in the BH case) at  $z/H = 1.2$  in the (a) NH and (b) BH cases. The dotted and hatched areas indicate low-speed regions at  $z/H = 3$  and high-speed regions at  $z/H = 1.2$ .

# 5 Scalar dispersion in and above a heated building array

## 5.1 Vertical turbulent scalar flux

Figure 5.1 shows the vertical profiles of 12 points-averaged mean scalar concentration  $\bar{c}$ , vertical turbulent scalar flux  $\overline{c'w'}$ , standard deviation of vertical velocity (or RMS of vertical velocity perturbation)  $\sqrt{\overline{w'^2}}$ , and ratio of scalar sweep to scalar ejection over the CC and IC points (Fig. 4.1b).  $c'$  and  $w'$  denote deviations from the time-averaged scalar concentration  $\bar{c}$  and vertical velocity  $\bar{w}$ , respectively. SGS parts are excluded in the calculated turbulence statistics because their magnitudes are much smaller than the magnitudes of resolved parts.

Over the IC points, the mean scalar concentration decreases monotonically with height in both the NH and BH cases (Fig. 5.1a), indicating that the scalar transport process over the IC points is similar to that over a flat surface. On the contrary, the mean scalar concentration abruptly decreases with height above an inflection point at  $z/H \sim 1$  over the CC points in both cases. Over the CC points, the mean scalar concentration within the canopy is higher than that over the IC points in both cases because plenty of scalars emitted from the bottom are trapped following the mean vortex flow (a canyon vortex in the  $x$ - $z$

plane and a double-eddy circulation in the  $x$ - $y$  plane) in the cavity spaces. Canyon vortices in the cavity spaces increase scalar concentration especially in the leeward upper part of cavity spaces, leading to active upward scalar transport. Over both the CC and IC points, the mean scalar concentration is lower in the BH case than in the NH case because more scalars are transported upward following thermally induced vertical turbulent motions in the BH case. However, actual magnitude of vertical turbulent scalar flux at the rooftop height in the BH case is slightly larger than that in the NH case over both the CC and IC points (Fig. 5.1b) because the standard deviation of vertical velocity in the BH case is larger than that in the NH case (Fig. 5.1c). Bottom heating induces stronger vertical turbulent scalar flux at the rooftop height without any noticeable change in mean vortex flow in cavity spaces (not shown). Over the CC points, in both the NH and BH cases, the vertical turbulent scalar flux has local peaks at the rooftop height (due to a large vertical gradient of scalar concentration) and at the lower part. Over the IC points, the vertical turbulent scalar flux has its maximum at  $z/H \sim 0.6$  in the NH case and at  $z/H \sim 1$  in the BH case.

Over both the CC and IC points,  $\sqrt{w'^2}$  tends to increase up to the rooftop height with its magnitude being larger in the BH case than in the NH case (Fig. 5.1c). While  $\sqrt{w'^2}$  decreases with height above  $z/H \sim 1.9$  (2.2) in the NH case,

$\sqrt{w'^2}$  in the BH case decreases with height above  $z/H \sim 1.4$  (0.9) and increases again with height above  $z/H \sim 3.5$  (3.7) over the CC points (IC points), reaching its maximum at  $z/H \sim 15$  (a little higher than half the domain height). This implies that large-scale vertical motions exist in the BH case as in the buoyancy-driven planetary boundary layer (Moeng and Sullivan 1994).

As in the quadrant analysis of vertical turbulent momentum flux, the instantaneous vertical turbulent scalar flux  $c'w'$  at one position can be classified into four quadrants: scalar ejection ( $c'_+w'_+$ ), scalar outward interaction ( $c'_-w'_+$ ), scalar sweep ( $c'_-w'_-$ ), and scalar inward interaction ( $c'_+w'_-$ ) (Katul et al. 1997). If a scalar source exists below the reference point, turbulent motions transport scalar upward by inducing scalar ejections and scalar sweeps and the ratio of the two events is sensitive to the type of turbulent flow. The vertical profiles of the scalar sweep-ejection ratio are plotted in Fig. 3d. Except for local peaks at the rooftop height, the ratio tends to decrease with height from the value larger than one near the bottom to the value less than one above the rooftop height in both the NH and BH cases. This indicates that turbulent motions transport scalar upward mostly by inducing scalar sweeps below the rooftop height and mostly by inducing scalar ejections above the rooftop height. The local peaks of the ratio at the rooftop height over the CC points indicate the dominance of scalar sweeps at the tops of cavity spaces in both the NH and BH cases.

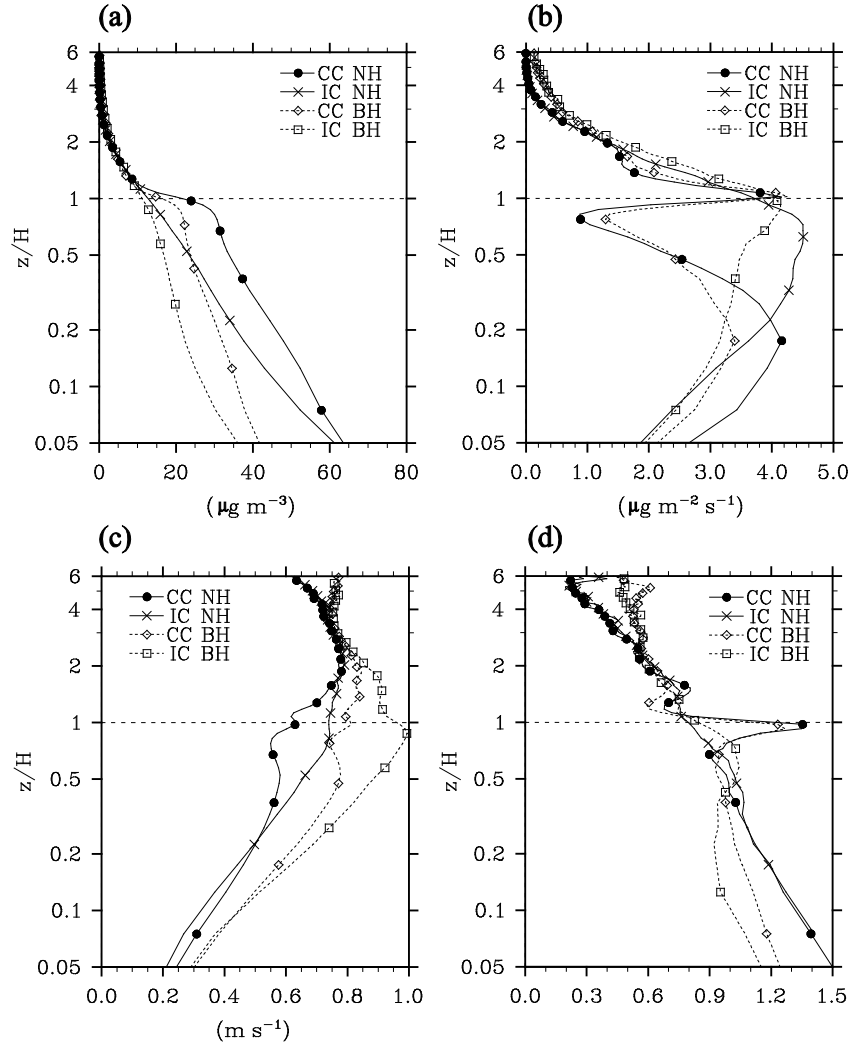


Figure 5.1. Vertical profiles of 12 points-averaged (a) mean scalar concentration, (b) vertical turbulent scalar flux, (c) standard deviation of vertical velocity, and (d) ratio of scalar sweep to scalar ejection in the NH and BH cases. Sampling points are marked as hollow circles for CC and marked as filled squares for IC in Fig. 4.1b. Note that the vertical axis ( $z/H$ ) is on a log scale.

## 5.2 Scalar dispersion above a building array

To investigate characteristic scalar dispersion patterns and their relationship with turbulence coherent structures (e.g., low-speed streaks), the fields of  $\text{sgn}(w') \cdot \max(0, c'w')$  with the contours of equal streamwise velocity ( $5.5 \text{ m s}^{-1}$ ) at  $t = 15480 \text{ s}$  in the NH case and those at  $t = 19080 \text{ s}$  in the BH case are shown in Fig. 5.2. The fields of  $\text{sgn}(w') \cdot \max(0, c'w')$  instead of  $c'w'$  are plotted to emphasize scalar ejections and scalar sweeps. The  $\max(0, c'w')$  returns the magnitude of  $c'w'$  only when  $c'w'$  is positive (when scalar is transported upward), and  $\text{sgn}(w')$  returns the sign of vertical velocity perturbation. Therefore, a positive value of  $\text{sgn}(w') \cdot \max(0, c'w')$  indicates a scalar ejection event (a combination of positive  $c'$  and positive  $w'$ ) and a negative value indicates a scalar sweep event (a combination of negative  $c'$  and negative  $w'$ ) following a typical definition used in the quadrant analysis of vertical turbulent scalar flux (Katul et al. 1997).

Above the building array, turbulence coherent structures such as low- and high-speed flow structures are actually lifted and sunken parts of the interface ( $u = 5.5 \text{ m s}^{-1}$ ) between the low- and high-speed air (Figs. 5.2a,d). Thus, low- and high-speed flow structures can be captured by just plotting the contours of equal streamwise velocity magnitude ( $5.5 \text{ m s}^{-1}$ ). In both the NH and BH cases, low-

speed streaks or streamwise elongated low-speed regions appear at  $z/H = 3$  (dotted) and high-speed streaks appear at  $z/H = 1.2$  (hatched). At  $z/H = 3$ , scalar ejections are concentrated on the low-speed regions in the NH and BH cases. Ejections of momentum occur successively (not shown), which induce streamwise elongated low-speed flow structures at  $z/H = 3$  (subsection 4.3). On the other hand, scalar ejections tend to occur in a plume-shape (not much streamwise elongated) in both the NH and BH cases. Especially in the BH case, scalar ejections following thermal updrafts appear at  $z/H = 3$  between  $y/H \sim 8$  and  $y/H \sim 18$ , showing more plume-like structures (Fig. 5.2e). It is also remarkable that one large secondary circular flow (stronger than that in the NH case) dominates the whole model domain with updrafts intensified by bottom heating in the BH case. Thus, the strengthened secondary circular flow induces streamwise elongated low-speed regions ( $22 < y/H < 24$  and  $0 < y/H < 3$ ) where scalar ejections occur frequently and wide high-speed regions ( $4 < y/H < 20$ ) where scalar ejections occur intermittently at  $z/H = 3$ . The low- and high-speed regions are stable enough to be detected even in the time-averaged fields above  $z/H \sim 2$  (not shown).

At  $z/H = 1.2$ , scalar transport events occur more frequently and both scalar ejection and scalar sweep play an important role in transporting scalar upward (Figs. 5.2c,f). In both the NH and BH cases, scalar sweeps tend to appear

in the high-speed regions and low scalar concentration air is entrained into the building array following scalar sweeps. Outside the high-speed regions, scalar ejections are dominant in the NH and BH cases.

Figure 5.3 shows conditionally averaged fields of scalar concentration perturbation and velocity vector fields with the contours of equal vertical velocity magnitude ( $0.7 \text{ m s}^{-1}$ ). Conditional averages are obtained by sampling data around local maximum points where  $c'w'$  is larger than  $3.0 \mu\text{g m}^{-2} \text{ s}^{-1}$ . In both the NH and BH cases, plume structures of positive perturbations of scalar concentration are tilted downstream in the  $x'-z$  planes and updrafts stronger than  $0.7 \text{ m s}^{-1}$  are located at the centers of perturbations. The combination of positive scalar concentration perturbation and updraft corresponds to scalar ejection, and this is the main scalar transport mechanism above the building array. Moreover, negative streamwise velocity perturbations coexist with updrafts in both the NH and BH cases (Fig. 5.3), implying that the momentum transport process and the scalar transport process are similar above the building array. While similar structures are detected in the NH and BH cases, bottom heating induces stronger updrafts and stronger spanwise converging flow in the BH case (partially due to the large-scale secondary circular flow). Especially in the BH case, intensified updrafts appear in the streamwise elongated low-speed region and the low-speed region itself could be part of the large-scale secondary circular flow.

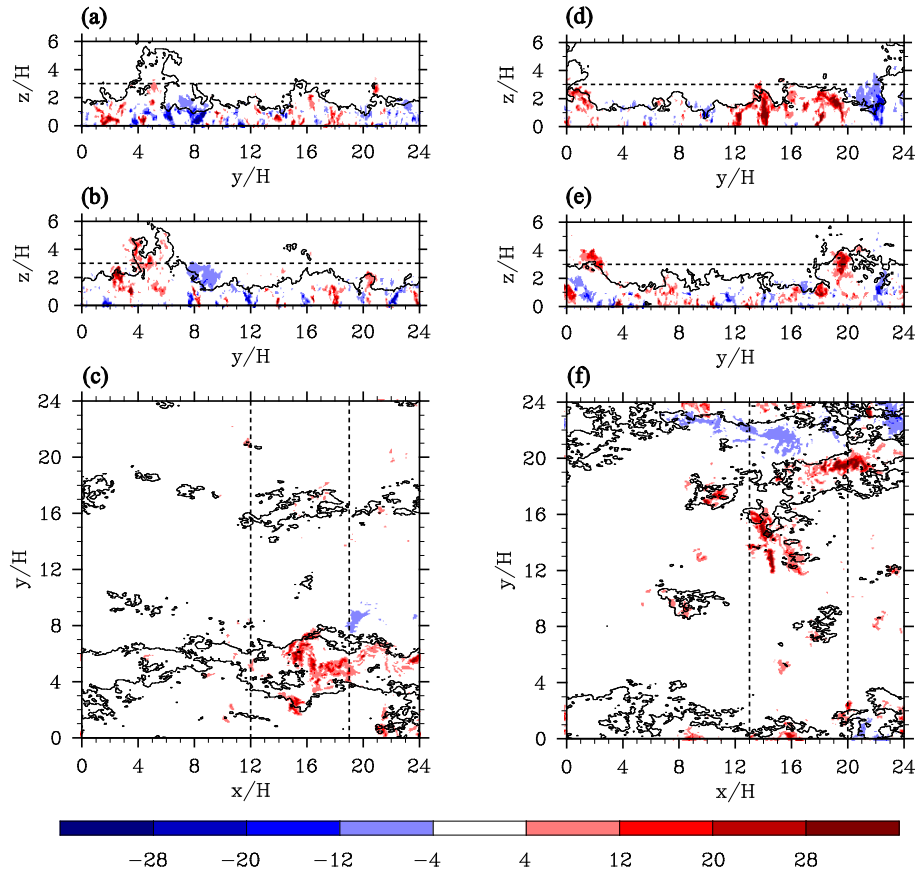


Figure 5.2. Instantaneous fields of  $\text{sgn}(w') \cdot \max(0, c'w')$  and the contours of equal streamwise velocity ( $5.5 \text{ m s}^{-1}$ ) at  $t = 15480 \text{ s}$  in the (a)  $y$ - $z$  plane ( $x/H = 12$ ), (b)  $y$ - $z$  plane ( $x/H = 19$ ), and (c)  $x$ - $y$  plane ( $z/H = 3$ ) in the NH case and same fields at  $t = 19080 \text{ s}$  in the (d)  $y$ - $z$  plane ( $x/H = 13$ ), (e)  $y$ - $z$  plane ( $x/H = 20$ ), and (h)  $x$ - $y$  plane ( $z/H = 3$ ) in the BH case.

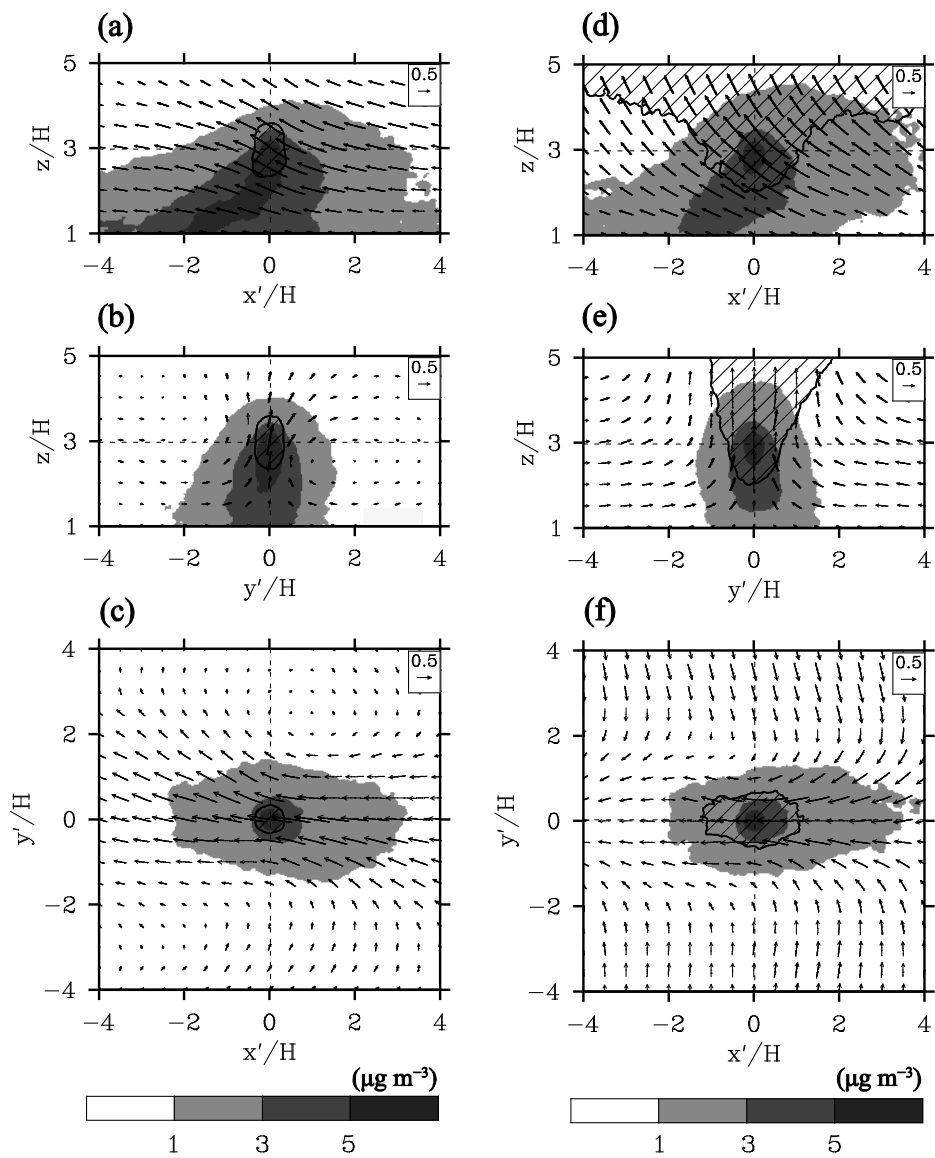


Figure 5.3. Conditionally averaged  $c'$  and velocity vector fields in the (a)  $x'$ - $z$  plane ( $y'/H = 0$ ), (b)  $y'$ - $z$  plane ( $x'/H = 0$ ), and (c)  $x'$ - $y'$  plane ( $z/H = 3$ ) in the NH case and those in the (d)  $x'$ - $z$  plane ( $y'/H = 0$ ), (e)  $y'$ - $z$  plane ( $x'/H = 0$ ), and (f)

$x'$ - $y'$  plane ( $z/H = 3$ ) in the BH case. Conditionally averaged  $u'$  instead of  $u$  is used for plotting velocity vector fields, and the contours of equal conditionally averaged vertical velocity ( $0.7 \text{ m s}^{-1}$ ) are added. The hatched areas indicate the regions where the conditionally averaged vertical velocity is higher than  $0.7 \text{ m s}^{-1}$ .

As shown in Fig. 5.2e, the patterns of scalar ejections are quite different depending on the spanwise position at  $z/H = 3$  in the BH case. To illustrate different patterns of scalar ejections, conditional averaging with additional criteria is conducted. First, the streamwise velocity perturbation from the horizontally averaged streamwise velocity at  $z/H = 5$  is calculated. The region where the streamwise velocity perturbation is smaller than  $-0.5 \text{ m s}^{-1}$  is defined as upper low-speed region and the region where the perturbation is larger than  $0.2 \text{ m s}^{-1}$  is defined as upper high-speed region. These values are chosen to guarantee sufficient samples for different patterns of scalar ejections. Figure 5.4 shows conditionally averaged fields of scalar concentration perturbation and velocity vector fields with the contours of equal vertical velocity magnitude ( $0.7 \text{ m s}^{-1}$ ) below the upper low-speed regions and those below the upper high-speed regions in the BH case. Below the upper low-speed regions, scalar ejections develop well in the streamwise and vertical directions. Actually, this kind of structure is part of the large-scale (covering the whole model domain) secondary circular flow and the secondary circular flow induces spanwise converging and diverging flow depending on the height. Even below the upper high-speed regions, bottom heating induces thermal updrafts and scalars are transported upward following the thermal updrafts. However, the thermal updrafts are not merged and not arranged in a line. Thus, the structure of the scalar ejections

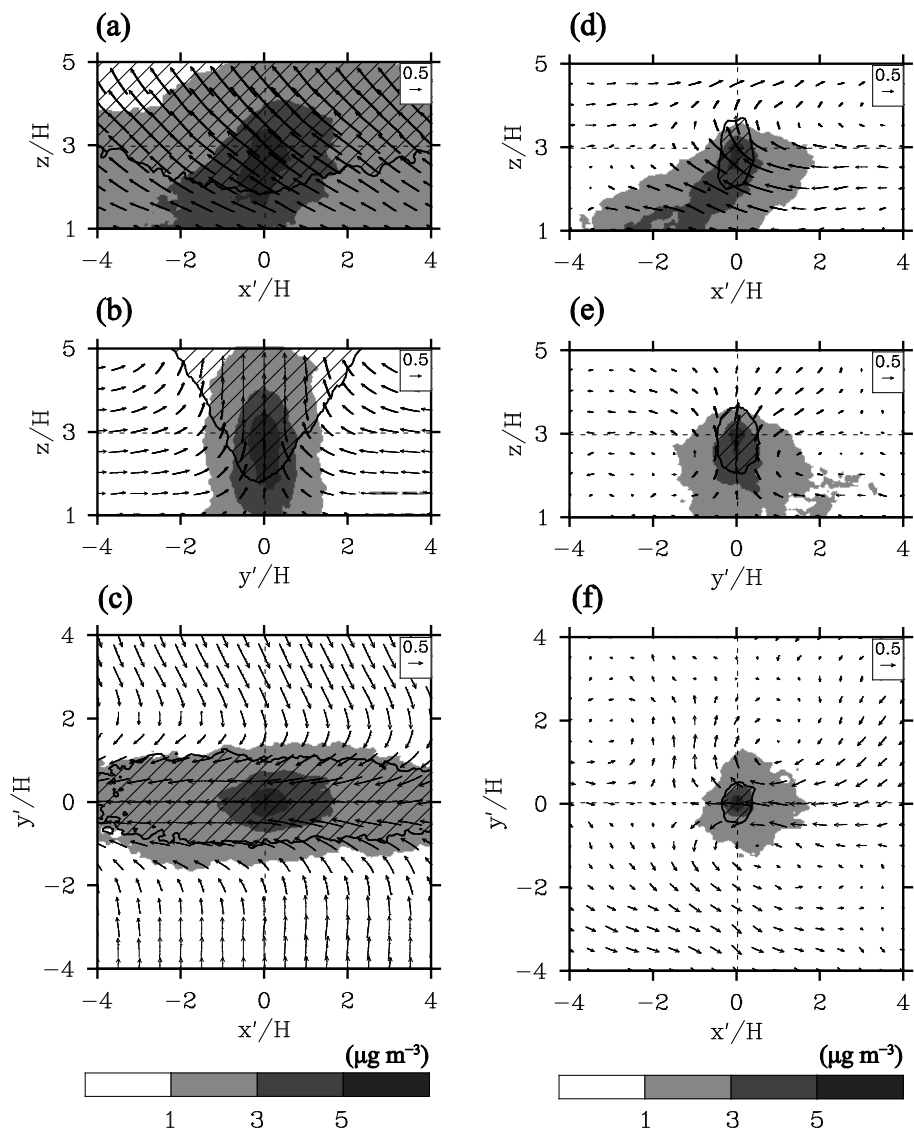


Figure 5.4. Conditionally averaged  $c'$  and velocity vector fields in the (a)  $x'$ - $z$  plane ( $y'/H = 0$ ), (b)  $y'$ - $z$  plane ( $x'/H = 0$ ), and (c)  $x'$ - $y'$  plane ( $z/H = 3$ ) below upper low-speed regions and those in the (d)  $x'$ - $z$  plane ( $y'/H = 0$ ), (e)  $y'$ - $z$  plane

( $x'/H = 0$ ), and (f)  $x'$ - $y'$  plane ( $z/H = 3$ ) below upper high-speed regions in the BH case. Conditionally averaged  $u'$  instead of  $u$  is used for plotting velocity vector fields, and the contours of equal conditionally averaged vertical velocity ( $0.7 \text{ m s}^{-1}$ ) are added. The hatched areas indicate the regions where the conditionally averaged vertical velocity is higher than  $0.7 \text{ m s}^{-1}$ .

below the upper high-speed regions seems to be isolated and the vertical size of the scalar ejections is limited by the upper high-speed flow.

### **5.3 Scalar dispersion in a building array**

To investigate thermal effects on overall scalar transport in the building array, mean and turbulent scalar fluxes summed over the windward, top, and leeward surfaces of a virtual box in Fig. 4.1b ( $11 \leq x/H \leq 13$ ,  $0 \leq y/H \leq 24$ ,  $0 \leq z/H \leq 1$ ) are calculated (Table 5.1). Rows in Table 5.1 indicate, in regular sequence, vertical scalar emission flux from the bottom surface, streamwise turbulent scalar flux at the windward surface, vertical turbulent scalar flux at the top surface, streamwise turbulent scalar flux at the leeward surface, streamwise mean scalar flux at the windward surface, vertical mean scalar flux at the top surface, streamwise mean scalar flux at the leeward surface, sum of all scalar fluxes, and the ratio of vertical turbulent scalar flux at the top surface to bottom scalar emission flux. The sign of the summed flux indicates the direction of the flux. Positive and negative fluxes indicate influx into the box and efflux from the box, respectively. Main sources of scalars in the box are scalar advection from upstream by streamwise mean flow and scalar emission from the bottom surface in both the NH and BH cases. Plenty of scalars in the box move downstream along the streamwise mean flow and part of scalars escape the box following

vertical turbulent motions at the top surface. In both the NH and BH cases, the magnitude of streamwise turbulent scalar flux summed over the windward or leeward surfaces is comparable in order with the magnitude of vertical turbulent scalar flux summed over the top surface. Owing to turbulent vertical motions strengthened by bottom heating, the ratio of vertical turbulent scalar flux at the top surface to the scalar emission flux at the bottom surface in the BH case is larger than the ratio in the NH case.

To compare the net contribution of surface-summed scalar fluxes to the mean scalar budget in the virtual box, the rates of scalar amount coming into the box and escaping the box by turbulent scalar advection ( $\overline{\Delta c'u'}$ ), mean scalar advection ( $\overline{\Delta cu}$ ), vertical turbulent scalar flux ( $\overline{c'w'}_{z=H}$ ), vertical mean scalar flux ( $\overline{cw}_{z=H}$ ) are plotted in Fig. 5.5. Streamwise mean scalar fluxes at the windward ( $x/H = 11$ ) and leeward ( $x/H = 13$ ) surfaces are large in magnitude (Table 5.1) but they balance each other, leading to net loss of scalar in the box. In the NH case, most of the scalar emission flux at the bottom surface is balanced by the mean streamwise scalar advection (the difference of streamwise mean scalar fluxes at the windward and leeward surfaces) and vertical turbulent scalar flux summed over the top surface. In the NH case, the vertical turbulent scalar flux is mainly composed of scalar ejection ( $\overline{c'_+w'_{+z=H}}$ ) and scalar sweep ( $\overline{c'_-w'_{-z=H}}$ ), and the contributions (to the mean scalar budget in the virtual box) of the two

Table 5.1. Scalar fluxes summed over the three surfaces of the virtual box (unit:  $\mu\text{g s}^{-1}$ ). Overbars represent time averages.

| cases   | NH      | BH      |
|---|---------|---------|
| $\int_0^{24H} \int_{11H}^{13H} (\overline{c'w'})_{z=0} dx dy$                               | 72000   | 72000   |
| $\int_0^{24H} \int_0^H (\overline{c'u'})_{x=11H} dz dy$                                     | -46842  | -31059  |
| $-\int_0^{24H} \int_{11H}^{13H} (\overline{c'w'})_{z=H} dx dy$                              | -51385  | -54423  |
| $-\int_0^{24H} \int_0^H (\overline{c'u'})_{x=13H} dz dy$                                    | 50458   | 30229   |
| $\int_0^{24H} \int_0^H (\overline{c\bar{u}})_{x=11H} dz dy$                                 | 226196  | 155436  |
| $-\int_0^{24H} \int_{11H}^{13H} (\overline{c\bar{w}})_{z=H} dx dy$                          | -4259   | -5514   |
| $-\int_0^{24H} \int_0^H (\overline{c\bar{u}})_{x=13H} dz dy$                                | -243122 | -164425 |
| sum   | 3047    | 2244    |
| $\int_0^{24H} \int_{11H}^{13H} (\overline{c'w'})_{z=H} / (\overline{c'w'})_{z=0} dx dy$ (%) | 71.4    | 75.6    |

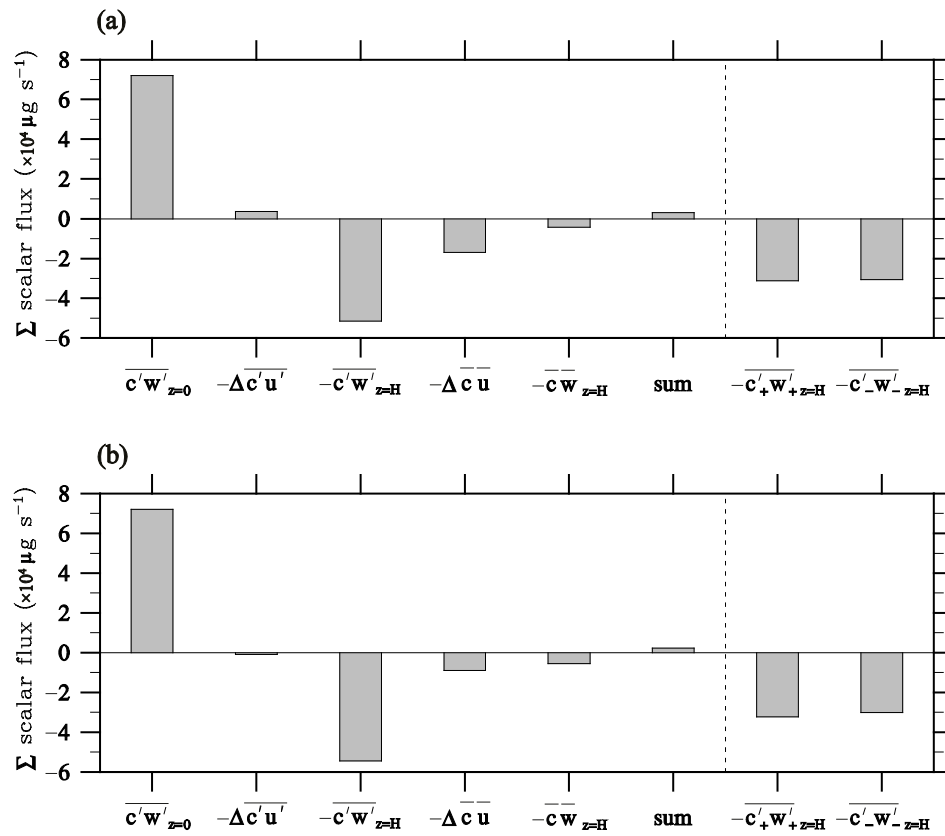


Figure 5.5. Scalar fluxes summed over the surfaces of the virtual box (Fig. 1b) in the (a) NH and (b) BH cases. Positive sign and negative sign indicate influx into the box and efflux from the box, respectively

scalar transport events are similar in magnitude. In comparison, in the BH case the vertical turbulent scalar flux summed over the top surface increases while the mean streamwise scalar advection decreases. This indicates that stronger vertical turbulent scalar transport decreases mean scalar concentration in the building array, reducing the amount of mean streamwise scalar advection. It is also noticeable that the contribution of scalar ejection is slightly larger than that of scalar sweep in the BH case.

Figure 5.6 shows time-averaged (for 1800 s) scalar concentration fields at  $z/H = 0.1$  and the contours of equal streamwise velocity magnitude ( $6 \text{ m s}^{-1}$ ) at  $z/H = 3$  in the NH and BH cases. Because low-speed flow structures passing above the building array do not move much in the spanwise direction as they move downstream, low-speed flow structures can be seen as streamwise elongated low-speed regions in the time-averaged streamwise velocity fields. This kind of low-speed flow structure might be associated with the steady secondary circulation, as also observed in the wind-tunnel experiment (Reynolds et al. 2007). Below the low-speed region at  $y/H \sim 5$ , scalars converge following the spanwise converging flow (Fig. 5.3) in the NH case. Actually, there exists another low-speed region at  $y/H \sim 16$  in the NH case and its existence can be confirmed by the weakly converging scalars. In the BH case, the scalar distribution pattern seems to be more dependent on the large-scale spanwise

motion. The large-scale secondary circular flow, developing above the bottom-heated building array, induces high scalar concentration below the rooftop height at  $y/H \sim 23$ . Scalar concentration fields at other heights ( $z/H \sim 0.5$ ) have similar distribution patterns (high below low-speed regions) in both the NH and BH cases, confirming the dominant influence of flow structures above the building array on scalar dispersion in the building canopy layer. The large-scale secondary circular flow in the BH case is closely related to the roll structure in the atmospheric boundary layer flow. Because of the limited spanwise domain size of the present simulation, only one secondary circular flow structure is simulated in the BH case. Several secondary circular flow structures appear in an additional simulation with a larger horizontal model domain and a capping inversion (not shown), and their spanwise scale is about two to three times the inversion height (Kim and Park 2003).

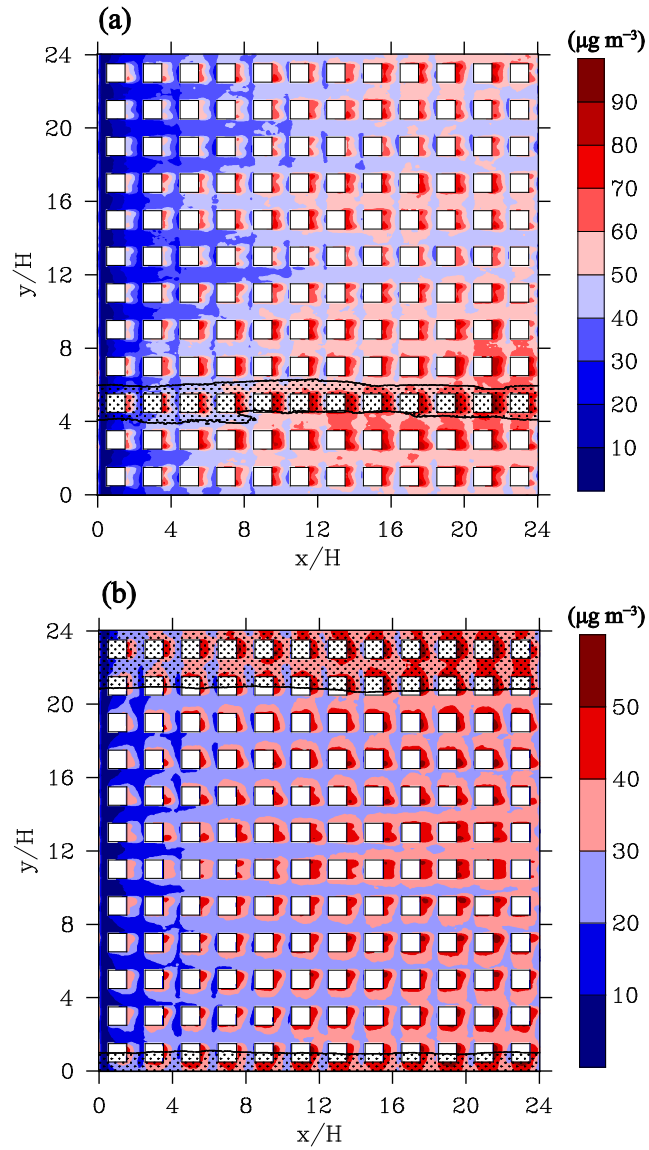


Figure 5.6. Time-averaged scalar concentration fields at  $z/H = 0.1$  and the contours of equal streamwise velocity magnitude ( $6 \text{ m s}^{-1}$ ) at  $z/H = 3$  in the (a) NH and (b) BH cases. The dotted areas indicate the regions where the mean streamwise velocity is lower than  $6 \text{ m s}^{-1}$  at  $z/H = 3$ .

As shown in Fig. 5.6, the scalar concentration in the building array is quite dependent on flow structures above the building array. The effects of the flow structures above the building array on scalar fields in the building array can be done across the interface that is usually located at the rooftop height. To examine characteristic scalar transport patterns, conditional averaging is done for the data sampled at local maximum points of instantaneous vertical turbulent scalar flux at the rooftop height. However, there are not any well-organized structures in the conditionally averaged fields (not shown) because two characteristic scalar transport events (scalar ejection and scalar sweep) are related to the flow structures in opposite vertical directions and they cancel each other out. Thus, the two kinds of events should be sampled separately to distinguish the two scalar transport patterns.

After applying additional criteria related to the sign of vertical velocity, two kinds of scalar transport patterns are obtained separately. Figure 5.7 shows scalar concentration perturbation and velocity vector fields conditionally averaged at  $z/H = 1$  with the criteria ( $c'w' > 15 \mu\text{g m}^{-2} \text{s}^{-1}$ ,  $w > 0 \text{ m s}^{-1}$ ) and those with other criteria ( $c'w' > 15 \mu\text{g m}^{-2} \text{s}^{-1}$ ,  $w < 0 \text{ m s}^{-1}$ ) in the NH case. In the NH case, scalar ejections occur with low-speed flow structures and scalar sweeps occur with high-speed flow structures. Scalar ejections seem to be well developed in the streamwise direction, and they tend to appear in the upstream

part of the streamwise elongated low-speed flow structures (Fig. 5.7c). On the contrary, high-speed flow structures, occurring with scalar sweeps, tend to be quite compact in the streamwise direction. Low- and high-speed flow structures above the building array induce scalar ejections and scalar sweeps at the rooftop height, respectively. Furthermore, they induce converging and diverging spanwise flow in the building array, leading to spanwise variation of mean scalar concentration therein (Fig. 5.6). The streamwise scale of high-speed flow structures is smaller than that of low-speed flow structures because some of the high-speed flow structures are locally generated by shear instability at the tops of cavity spaces and the size of scalar sweeps is also limited by the building blocks. In the BH case, similar structures (having a larger magnitude than those in the NH case) appear in the conditionally averaged fields (not shown).

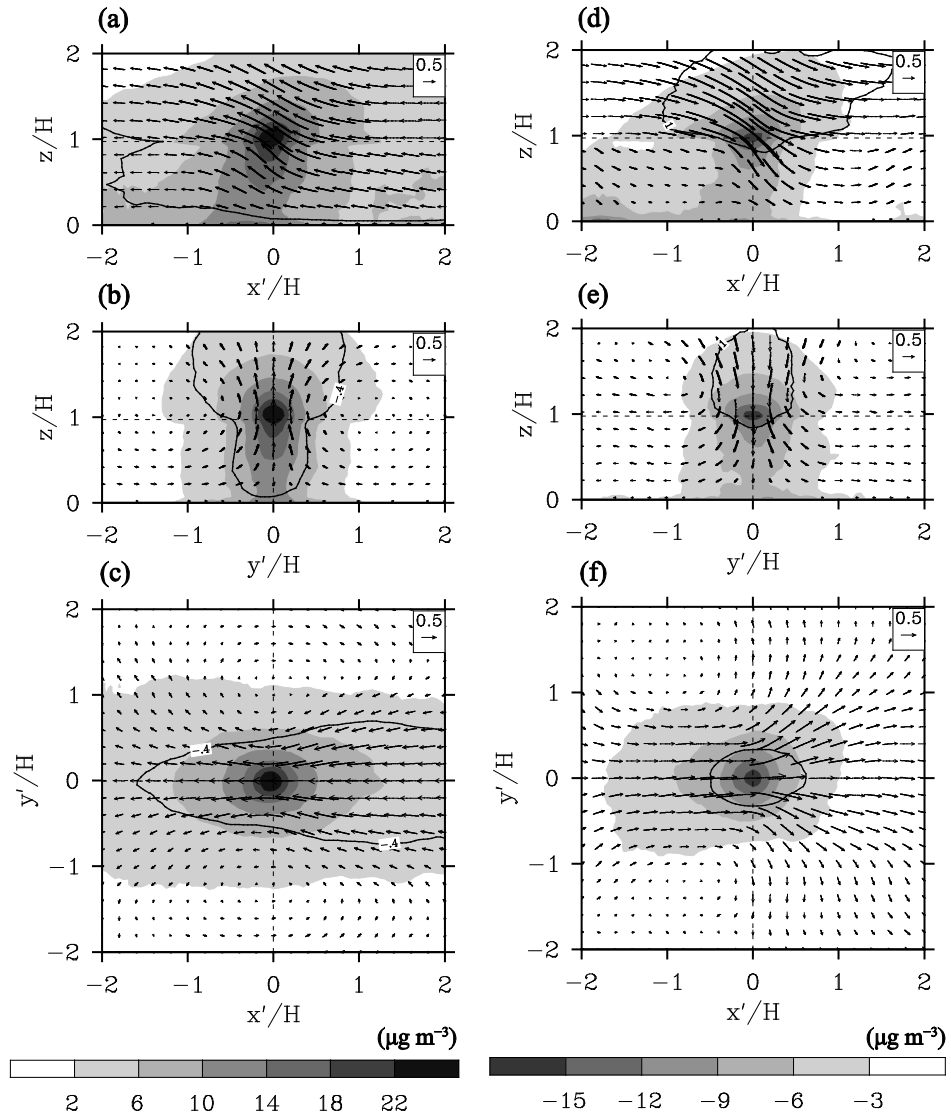


Figure 5.7. Conditionally averaged  $c'$  and velocity vector fields in the (a),(d)  $x'$ - $z$  plane ( $y'/H = 0$ ), (b),(e)  $y'$ - $z$  plane ( $x'/H = 0$ ), and (c),(f)  $x'$ - $y'$  plane ( $z/H = 1$ ) for (left) scalar ejection and (right) scalar sweep in the NH case. Conditionally averaged  $u'$  instead of  $u$  is used for plotting velocity vector fields, and the

contours of equal conditionally averaged streamwise velocity perturbation are added. ( $-0.4 \text{ m s}^{-1}$  for scalar ejection and  $1 \text{ m s}^{-1}$  for scalar sweep).

# 6 Convective boundary layers over flat and urban-like surfaces

## 6.1 Experimental design

To investigate the effects of urban-like surface with building blocks on turbulence structures of convective boundary layer (CBL), four cases are simulated: a free CBL over a flat surface (FF), a sheared CBL over a flat surface (SF), a sheared CBL over a block array (SB), and a strongly sheared CBL over a flat surface (SSF). In all cases, PALM is integrated for 2 h and the last 600-s simulation data are analyzed. The magnitude of bottom heat flux is  $0.2 \text{ K m s}^{-1}$  in all cases.

Figure 6.1 shows the computational domain and block configuration in the SB case. The computational domain size is 15360 m in the  $x$  (streamwise) direction, 15360 m in the  $y$  (spanwise) direction, and 1900 m in the  $z$  (vertical) direction. The grid size in both the  $x$  and  $y$  directions is 20 m. The grid size in the  $z$  direction is 5 m up to  $z = 80$  m and increases with an expansion ratio of 1.08 up to  $z \sim 155$  m, then being 10 m above that height. An idealized block array, which is composed of same-sized rectangular blocks (320 m wide, 320 m long, and 80 m high), is considered in the SB case. Due to the limited resolution, an array of blocks (imitating that each block represents a group of buildings) is considered

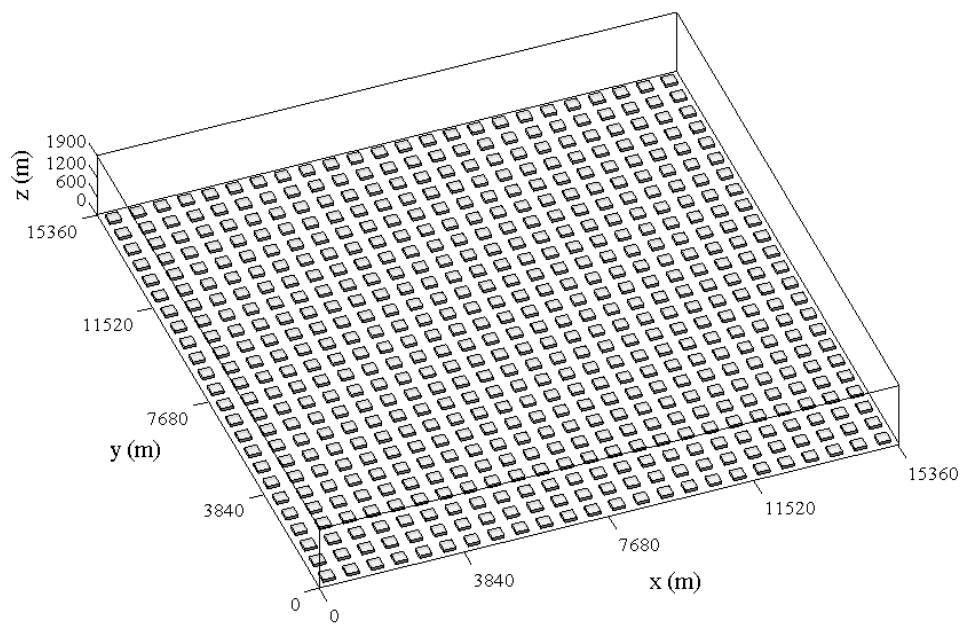


Figure 6.1. Illustrations of the computational domain and block configuration in the SB case.

and 16 grids are present in each block length to explicitly resolve flow around each block (Xie and Castro 2006). The blocks are arranged in lines with a constant spacing of 320 m in both the  $x$  and  $y$  directions. Therefore, the plan area density of the block array is 25% and the aspect ratio of street canyon is 0.25. The cyclic boundary condition is applied at the lateral boundaries for velocity components, temperature, and SGS TKE, and the Dirichlet boundary condition is applied at the top boundary. Westerly geostrophic wind ( $U_g = 10 \text{ m s}^{-1}$  in the SF and SB cases and  $15 \text{ m s}^{-1}$  in the SSF case) is initially imposed in the model domain, and the Coriolis parameter is evaluated at latitude  $37^\circ\text{N}$ . The Coriolis force induces anti-clockwise turning of mean wind direction downward in the CBL. At grid points closest to all the solid surfaces, the MO similarity is employed in the momentum equation, and the roughness length for momentum is 0.1 m.

## 6.2 Turbulence structures

Figure 6.2 shows the vertical profiles of horizontally averaged (mean) vertical turbulent heat flux  $\overline{\langle \theta'w' \rangle}$ , potential temperature  $\overline{\langle \theta \rangle}$ , vertical turbulent momentum flux  $\overline{\langle u'w' \rangle}$ , and streamwise velocity  $\overline{\langle u \rangle}$  in the FF, SF, and SB cases. Here,  $u$  is the streamwise velocity,  $w$  is the vertical velocity, and  $\theta$  is the

potential temperature and  $u'$ ,  $w'$ , and  $\theta'$  denote deviations from the horizontally averaged variables  $\langle u \rangle$ ,  $\langle w \rangle$ , and  $\langle \theta \rangle$ , respectively. In this study, overbars and angle brackets indicate temporal (600-s) and spatial averages. The vertical turbulent heat flux linearly decreases with height from the bottom surface (or block top height in the SB case) to the inversion height ( $z_i$ ) in all cases (Fig. 6.2a). The inversion height here is defined as the height where the vertical turbulent heat flux reaches a minimum value (the entrainment heat flux). The upper limit ( $z_{iu}$ ) and lower limit ( $z_{il}$ ) of the entrainment zone are determined as the heights where the magnitude of vertical turbulent heat flux are zero above and below the inversion height, respectively. Calculated quantities such as surface friction velocity and convective velocity in the four cases are listed in Table 6.1. The magnitude of entrainment heat flux is larger in the SB case ( $-0.039 \text{ K m s}^{-1}$ ) than in the FF and SF cases ( $-0.026$  and  $-0.028 \text{ K m s}^{-1}$ , respectively). Although the difference in entrainment heat flux magnitude between the FF and SF cases is very small, the thickness of entrainment zone ( $z_{iu} - z_{il}$ ) in the SF case (290 m) is larger than that in the FF case (250 m), indicating more active entrainment in the SF case.

In the mixed layer ( $0.1z_i < z < z_{il}$ ), the potential temperature is nearly constant because of active convective mixing (Fig. 6.2b). The magnitudes of entrainment heat flux in the FF, SF, and SB cases are related to the degree of the

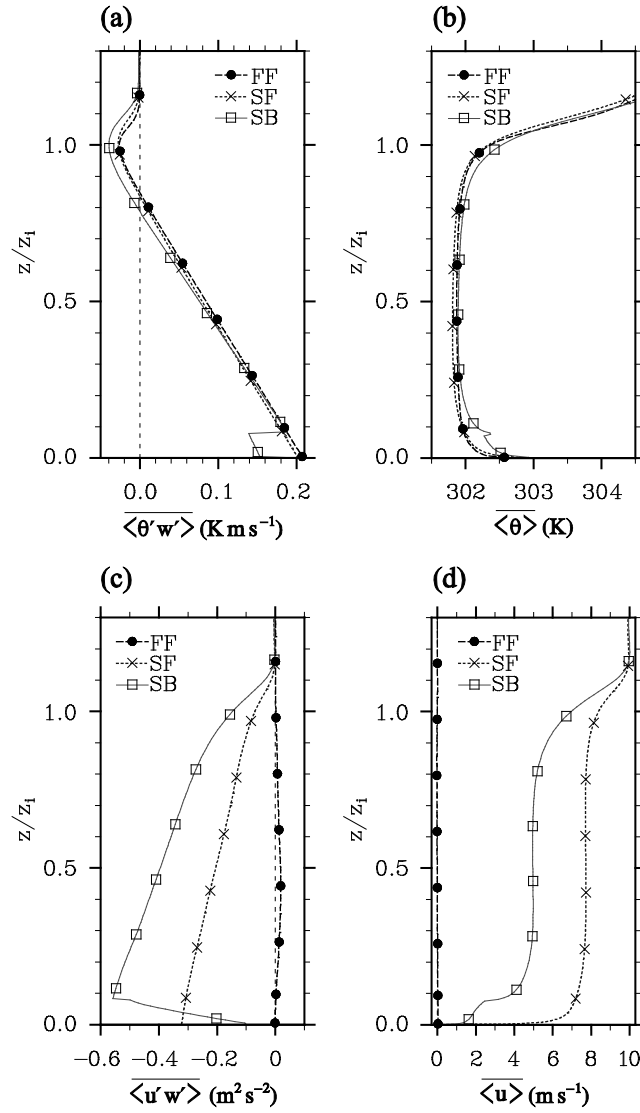


Figure 6.2. Vertical profiles of horizontally averaged (a) vertical turbulent heat flux, (b) potential temperature, (c) vertical turbulent momentum flux, and (d) streamwise velocity in the FF, SF, and SB cases.

Table 6.1. Bottom heat flux, geostrophic wind speed, friction velocity, convective velocity  $(gz_i Q_0/T)^{1/3}$  where  $g$  is the gravitational acceleration and  $T$  is the temperature, the ratio of friction velocity to convective velocity, inversion height, the ratio of inversion height to the Monin-Obukhov length, the thickness of entrainment zone, difference in streamwise velocity between the upper and lower limits of entrainment zone, turbulent heat flux at the inversion height, and the ratio of vertical turbulent heat flux at the inversion height to bottom heat flux in the FF, SF, SSF, and SB cases.

|  | FF      | SF     | SSF    | SB     |
|--|---------|--------|--------|--------|
| $Q_0$ (K m s <sup>-1</sup> )   | 0.2     | 0.2    | 0.2    | 0.2    |
| $U_g$ (m s <sup>-1</sup> )   | 0       | 10     | 15     | 10     |
| $u_*$ (m s <sup>-1</sup> )   | 0.03    | 0.57   | 0.74   | 0.76   |
| $w_*$ (m s <sup>-1</sup> )   | 1.87    | 1.87   | 1.87   | 1.88   |
| $u_*/w_*$  | 0.02    | 0.31   | 0.40   | 0.40   |
| $z_i$ (m)  | 1005    | 995    | 1005   | 1025   |
| $-z_i/L$   | 71416.8 | 14.1   | 6.4    | 6.1    |
| $z_{iu} - z_{il}$ (m)  | 250     | 290    | 360    | 400    |
| $\overline{\langle u \rangle}_{z_{iu}} - \overline{\langle u \rangle}_{z_{il}}$ (m s <sup>-1</sup> ) | 0.04    | 2.12   | 3.76   | 4.86   |
| $\overline{\langle \theta'w' \rangle}_{z_i}$ (K m s <sup>-1</sup> )                                  | -0.026  | -0.028 | -0.032 | -0.039 |
| $-\overline{\langle \theta'w' \rangle}_{z_i}/Q_0$ (%)  | 13.1    | 13.9   | 16.1   | 19.7   |

mixing of heat in the entrainment zone. More active mixing of heat (higher potential temperature between  $z_{il}$  and  $z_i$ ) in the SB case than in the other cases is distinct in Fig. 6.2b. The magnitude of vertical turbulent momentum flux is larger in the SB case than in the FF and SF cases (Fig. 6.2c) because of turbulent eddies generated by the blocks. Due to more turbulent surface layer in the SB case, the mean streamwise velocity is lower than that in the SF case (Fig. 6.2d). The deceleration in the SB case induces stronger wind shear in the entrainment zone than in the SF case. Note that the wind shear in the entrainment zone is  $0.0122 \text{ s}^{-1}$  in the SB case and  $0.0073 \text{ s}^{-1}$  in the SF case. Here, the wind shear in the entrainment zone is calculated by dividing the difference in streamwise velocity between the upper and lower limits of entrainment zone by the thickness of entrainment zone (Table 6.1).

Vertical velocity fields at  $z = 500 \text{ m}$  ( $\sim z_i/2$ ) and the same fields at  $z = 1000 \text{ m}$  ( $\sim z_i$ ) in the FF, SF, and SB cases at  $t = 6900 \text{ s}$  are plotted in Fig. 6.3. Convection cells occur in the FF case, and their cellular structure and the circular shape of each cell top are distinct in the  $x$ - $y$  planes at  $z = 500 \text{ m}$  and  $1000 \text{ m}$ , respectively (Figs. 6.3a,d). In the SF case, the ratio of friction velocity to convective velocity (0.31) is slightly smaller than 0.35 (Sykes and Henn 1989), the value at which HCRs occur, and intermediate structures of cells and rolls appear. In contrast, HCRs appear in the SB case with their axis slightly inclined

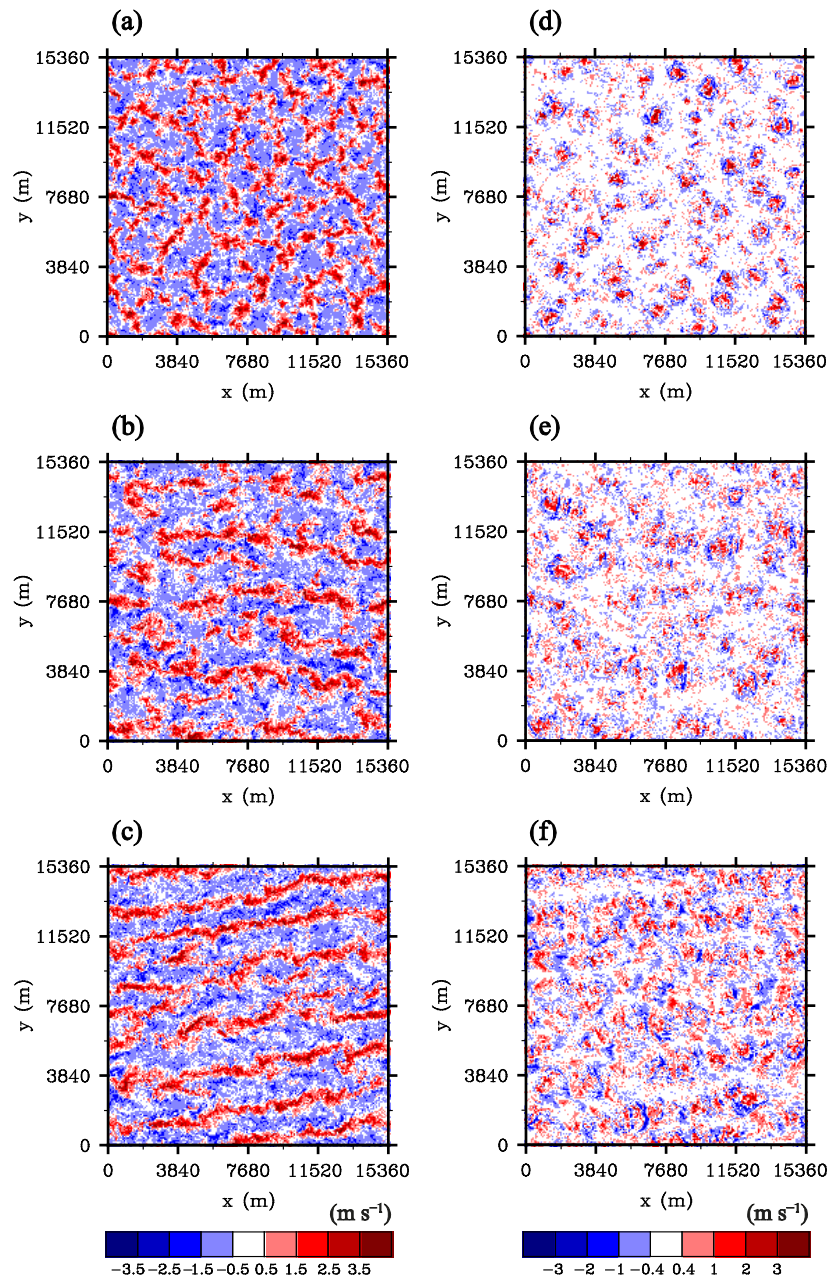


Figure 6.3 Vertical velocity fields in the (a),(d) FF, (b),(e) SF, and (c),(f) SB cases at (left)  $z = 500$  m and (right)  $z = 1000$  m at  $t = 6900$  s.

toward the north. Note that the ratio of friction velocity to convective velocity in the SB case is 0.40, exceeding the value at which HCRs occur (0.35). At  $z = 500$  m (in the mixed layer), HCRs are distinct and their spanwise spacing is about twice the inversion height. The spacing of convective rolls observed in this study ( $\sim 2z_i$ ) is similar to the value reported in Kim and Park (2003). At  $z = 1000$  m (near the inversion height), alternating updrafts and downdrafts appear mostly above the rising parts of HCRs. This pattern is similar to the wave-like motion occurring with strong wind shear (Sullivan et al. 1998; Kim et al. 2003). This kind of HCRs and wave-like motions at approximately the inversion height also appear in the SSF case where the ratio of friction velocity to convective velocity (0.40) is larger than 0.35.

Figure 6.4 shows the spectral density fields of vertical velocity at  $t = 6900$  s in the SF and SB cases. The spectral density of vertical velocity at each spanwise wavelength and height is calculated and plotted. The spectral density (or variance) of vertical velocity is high at  $(\lambda_y, z) \sim (2000 \text{ m}, 500 \text{ m})$ , indicating the dominance of HCRs in the SB case and the dominance of intermediate structures in the SF case. The value of the spectral density around the maximum is larger over a narrower range in the SB case than in the SF case. The spectral density above the inversion height is also higher in the SB case than in the SF case, indicating stronger fluctuations there. It is noticeable that the spectral

density below  $z \sim 160$  m is slightly high between  $\lambda_y \sim 600$  m and  $\lambda_y \sim 800$  m in the SB case. This might be related to turbulent eddies generated around the blocks.

Figure 6.5 shows the vertical profiles of spanwise averaged (at  $x = 7680$  m) TKE, skewness of streamwise velocity, and skewness of vertical velocity in the FF, SF, SB, and SSF cases. As the geostrophic wind speed increases from  $10$   $\text{m s}^{-1}$  (SF) to  $15$   $\text{m s}^{-1}$  (SSF), TKE increases and TKE in the upper mixed layer and entrainment zone is similar in magnitude to the SB case. The vertical profiles of streamwise velocity skewness indicate that strong negative perturbation events occur in the lower and upper parts of the CBLs in all cases except for in the FF case. Local minimum below  $z/z_i = 0.2$  is attributed to ejection eddies induced by the bottom surface (or blocks), and that in the entrainment zone might be related to turbulent eddies induced by shear instability in all sheared CBLs. Due to the existence of blocks and the large difference in streamwise velocity in the entrainment zone, negative perturbations occur more strongly in the SB case than in the other cases. The vertical profiles of vertical velocity skewness in all cases exhibit typical structures of the CBL (i.e., having maximum values at  $z/z_i \sim 0.5$ ). The vertical velocity skewness is nearly constant between  $z/z_i = 0.1$  and  $0.2$  in the SB case. This might be related to ejection eddies induced by blocks as is shown in Fig. 6.4b.

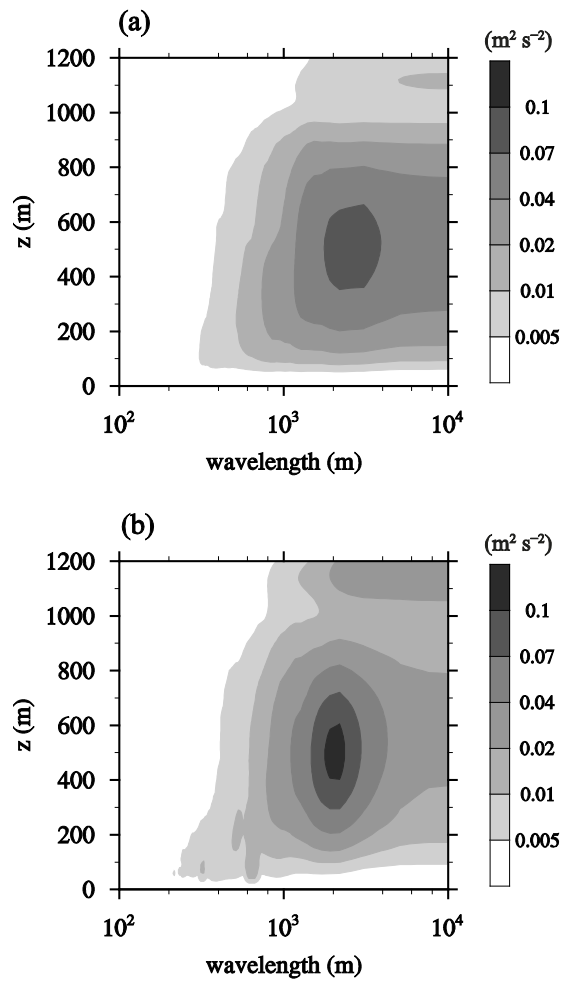


Figure 6.4. Spectrum density fields of vertical velocity in the  $\lambda_y$ - $z$  plane at  $t = 6900$  s in the (a) SF and (b) SB cases.

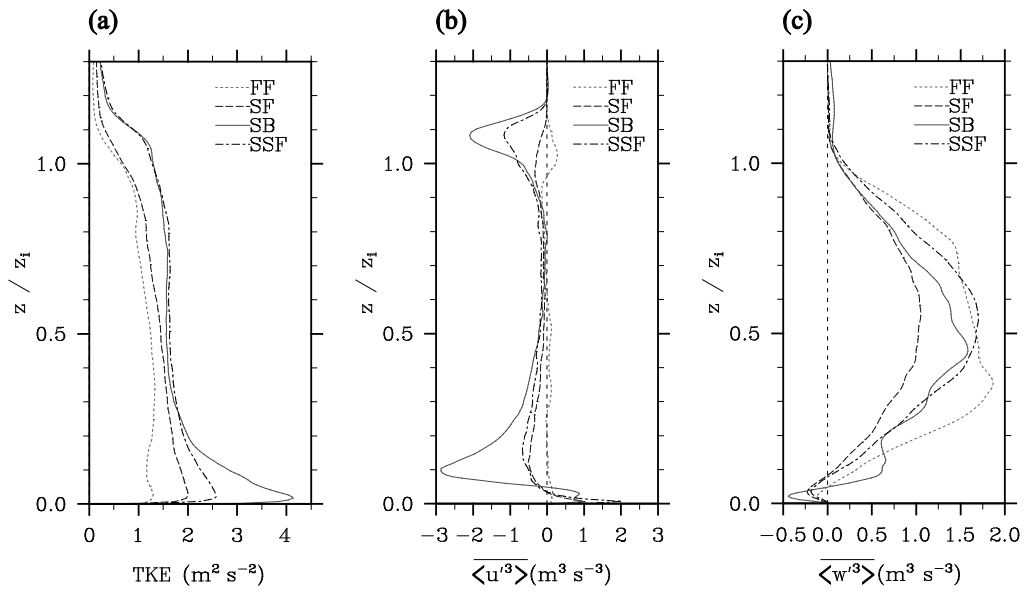


Figure 6.5. Vertical profiles of spanwise averaged (at  $x = 7680$  m) (a) TKE, (b) skewness of streamwise velocity, and (c) skewness of vertical velocity in the FF, SF, SB, and SSF cases.

### 6.3 Effects of blocks on the entrainment heat flux

Figure 6.6 shows the probability density functions (PDFs) of normalized streamwise velocity  $u/U_g$  at  $z = 500$  m and the PDFs at  $z = 1000$  m in the SF, SB, and SSF cases. Blocks induce turbulent eddies such as ejections, transporting momentum downward above the blocks and decelerating mean flow in the mixed layer. The PDF at  $z = 500$  m in the SB case is quite different from the PDFs in the other cases while the PDF in the SF case is quite similar to the PDF in the SSF case. The decelerated flow in the mixed layer over the block array also decelerates the flow in the entrainment zone. The deceleration in the SB case is distinct at  $z = 1000$  m (Fig. 6.6b).

The vertical profiles of vertical turbulent heat flux contributed by the four quadrant events are plotted in Fig. 6.7. The instantaneous vertical turbulent heat flux  $\theta'w'$  can be classified into the four quadrant events: warm air rising or ejection ( $Q_1: \theta'_+w'_+$ ), cool air rising ( $Q_2: \theta'_-w'_+$ ), cool air sinking or sweep ( $Q_3: \theta'_-w'_-$ ), and warm air sinking ( $Q_4: \theta'_+w'_-$ ) (Sullivan et al. 1998). Below the entrainment zone ( $z < z_{il}$ ), warm air raised by updrafts ( $Q_1$ ) and cool air sunk by downdrafts ( $Q_3$ ) contribute to most of the vertical turbulent heat flux in all cases. In the FF case, rising cool air ( $Q_2$ ) and sinking cool air ( $Q_3$ ) dominate turbulent heat transport in the entrainment zone (Fig. 6.7a). This kind of transport pattern

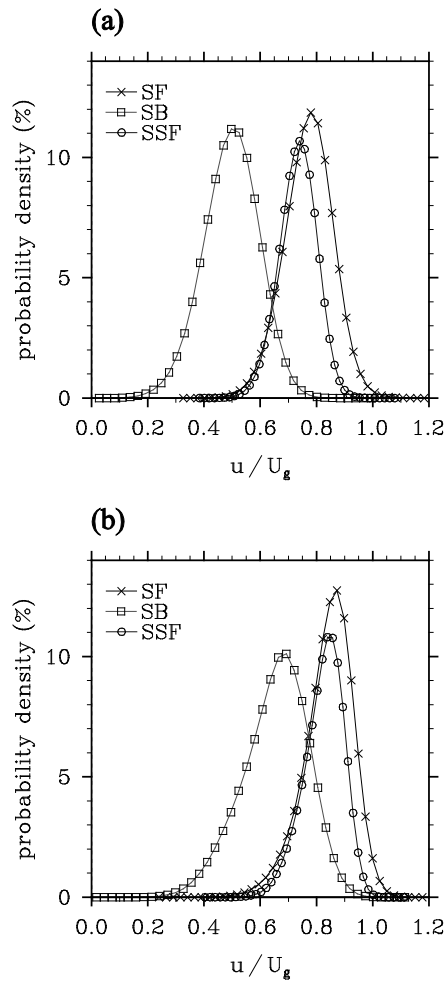


Figure 6.6. Probability density distributions of streamwise velocity at (a)  $z = 500$  m and (b)  $z = 1000$  m in the SF, SB, and SSF cases.

corresponds to the circular-shaped updrafts surrounded by downdrafts at  $z = 1000$  m in Fig. 6.3d. As the wind shear in the entrainment zone increases, the magnitudes of  $Q_1$  and  $Q_4$  increase and also the magnitude of vertical turbulent heat flux (the sum of fluxes contributed by all the quadrant events) increases in the entrainment zone (Fig. 6.7). In the SB case, the magnitudes of  $Q_1$  and  $Q_4$  in the entrainment zone increase more than those in the SF case because of the increased wind shear in the entrainment zone. This kind of increasing trend of  $Q_1$  and  $Q_4$  with increasing wind shear is closely related to the mixing of upper warm air by wave-like motions, and this corresponds to the breaking of Kelvin–Helmholtz waves, as reported in Kim et al. (2003).

The different heat transport patterns between the FF and SB cases are illustrated (Fig. 6.8). The fields of instantaneous heat flux  $\theta'w'$  at  $z = 1000$  m and  $t = 6900$  s in the FF and SB cases are plotted in Fig. 6.8. The contours of vertical velocity ( $0.5 \text{ m s}^{-1}$ ) represent the rising parts (at  $z = 500$  m) of convection cells in the FF case and those of HCRs in the SB case. In both cases, strong turbulent heat transport events are concentrated on the rising parts of convective flow structures. While the downward turbulent heat transport events (mainly composed of  $Q_2$ ) dominate over the upward turbulent heat transport events in the FF case, quite strong upward turbulent heat transport events intermittently occur with more frequent downward turbulent heat transport events in the SB case.

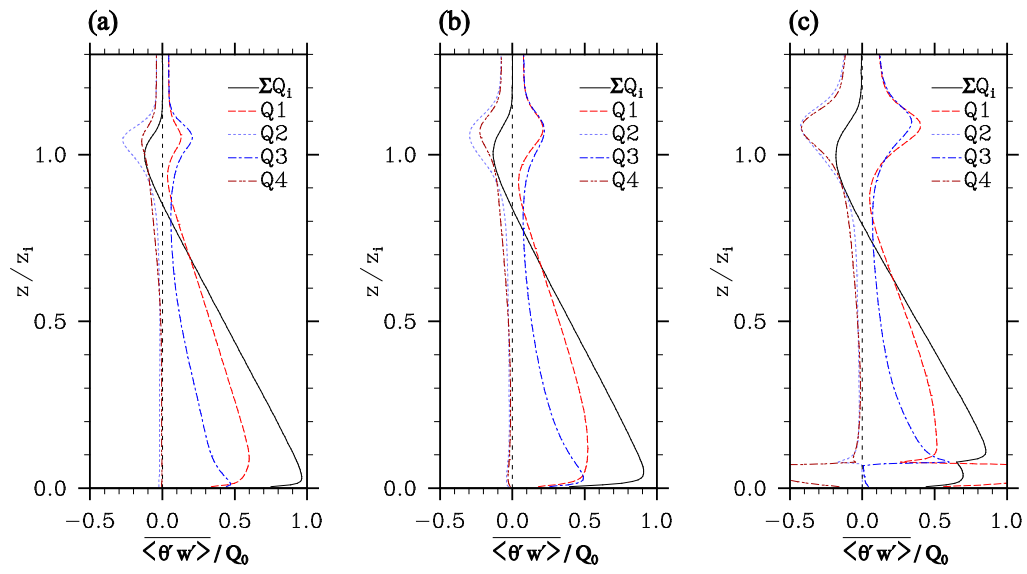


Figure 6.7. Vertical profiles of spanwise averaged (at  $x = 7680$  m) vertical turbulent heat flux contributed by the four quadrants in the (a) FF, (b) SF, and (c) SB cases.

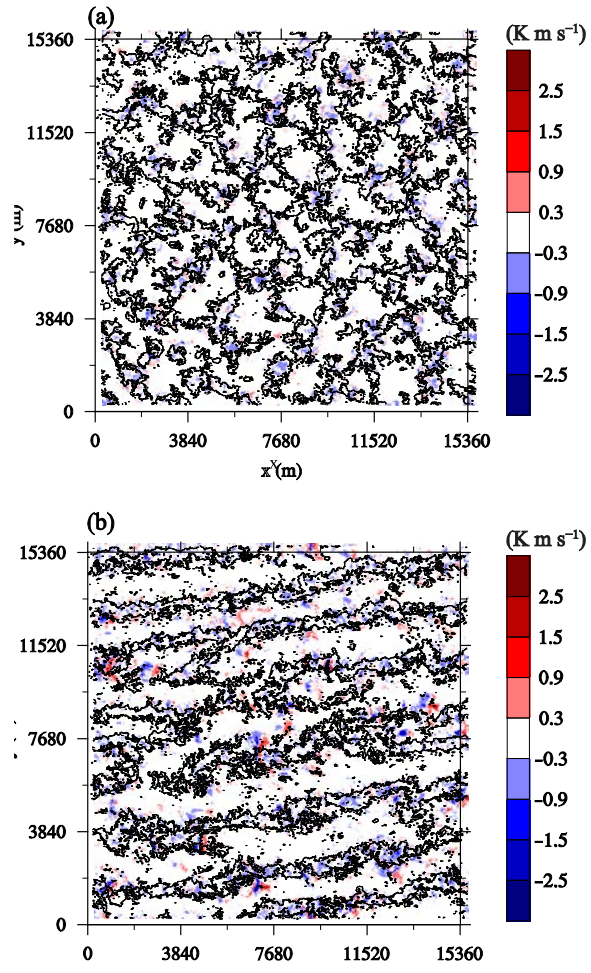


Figure 6.8. Fields of instantaneous heat flux  $\theta'w'$  at  $z = 1000$  m and  $t = 6900$  s in the (a) FF and (b) SB cases. The contours of vertical velocity ( $0.5 \text{ m s}^{-1}$ ) at  $z = 500$  m are added.

Figure 6.9 shows the cospectral density fields of vertical velocity and potential temperature at  $t = 6900$  s in the SF and SB cases. As in the spectrum fields of vertical velocity shown in Fig. 6.4, the cospectrum field in the SB case shows more compact shape, centered on  $(\lambda_y, z) \sim (2000 \text{ m}, 300 \text{ m})$ , than that in the SF case. Especially in the entrainment zone, negative cospectral density appears in a larger magnitude in the SB case than in the SF case, indicating stronger downward turbulent heat flux over the HCRs.

Figure 6.10 shows the ratio of entrainment heat flux to bottom heat flux with the difference in streamwise velocity between the upper and lower limits of the entrainment zone in all cases. As shown in Fig. 6.6, blocks in the SB case decelerate mixed-layer flow and increase wind shear in the entrainment zone. This kind of the indirect effect of blocks on the entrainment zone corresponds well to the indirect effect of surface shear reported by Conzemius and Fedorovich (2006). In the cases with constant bottom heat flux ( $0.2 \text{ K m s}^{-1}$ ), the ratio of entrainment heat flux to bottom heat flux tend to increase linearly with increasing streamwise velocity difference across the entrainment zone (Fig. 6.10). Also, a linear relation between the ratio of entrainment heat flux to bottom heat flux and wind shear in the entrainment zone is found. To confirm the linear relation, we simulated one more CBL over a flat surface with a geostrophic wind speed of  $20 \text{ m s}^{-1}$  (SSF2). In the SSF2 case, the ratio of the mixed-layer wind

speed to the geostrophic wind speed is similar to the ratios in the SF and SSF cases. However, the absolute value of the streamwise velocity difference across the entrainment zone in the SSF2 case is larger than that in the SB case and the ratio of entrainment heat flux to bottom heat flux in the SSF2 case is also larger than that in the SB case (Fig. 6.10). Thus, the magnitude of wind shear in the entrainment zone (or velocity jump at the inversion height) as well as the surface shear is important for parameterizing the entrainment heat flux (Conzemius and Fedorovich 2006).

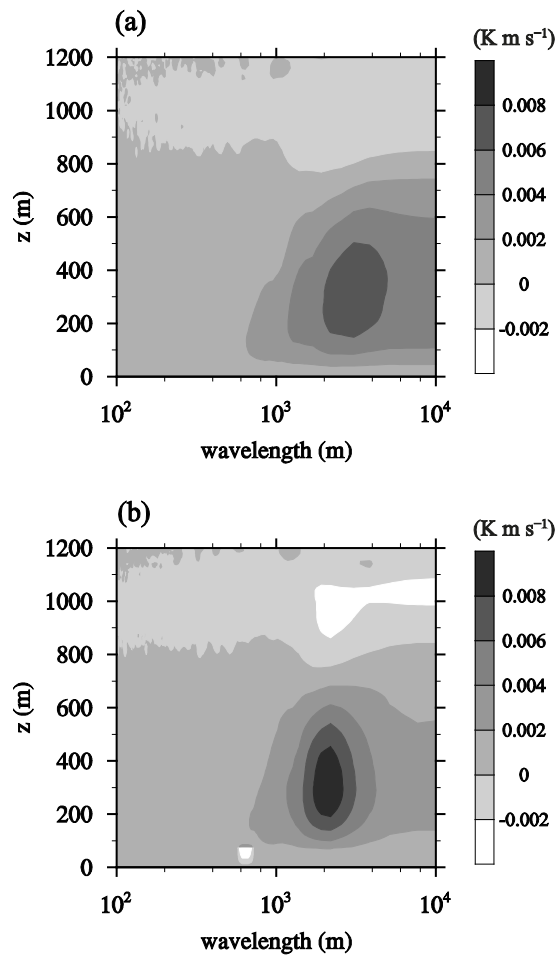


Figure 6.9. Cospectral density fields of vertical velocity and potential temperature in the  $\lambda_y$ - $z$  plane at  $t = 6900$  s in the (a) SF and (b) SB cases.

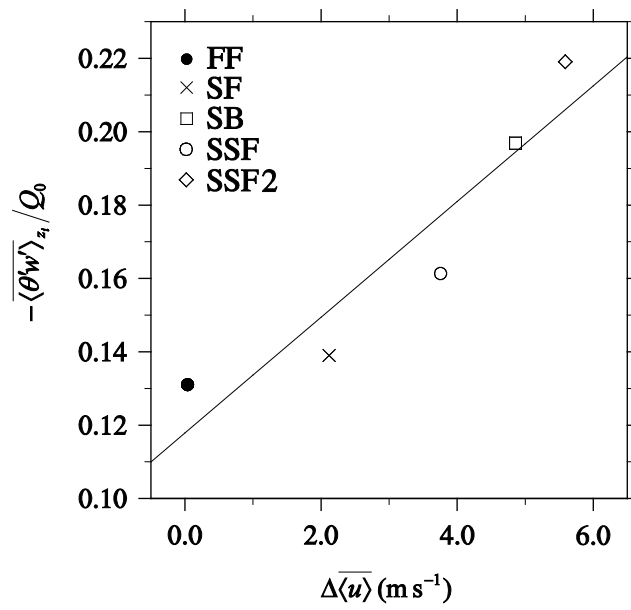


Figure 6.10. The ratio of entrainment heat flux to bottom heat flux ( $-\langle \theta'w' \rangle_{z_i} / Q_0$ ) with the difference in streamwise velocity between the upper and lower limits of the entrainment zone in all cases.

# 7 Turbulent flow in a densely built-up urban area

## 7.1 Experimental design

To simulate turbulent flow in an actual urban morphology, gridded elevation data of a densely built-up urban area are used as the bottom boundary of the LES model. Figure 7.1 shows the elevation field of ground and building top surfaces in the computational domain. A densely built-up area of Seoul, South Korea, is selected. The main domain ( $3840 \text{ m} \times 1920 \text{ m}$ , the inner rectangular region in Fig. 7.1) includes high-rise buildings, broad streets, residential areas, and a park. There are many high-rise buildings (two of them are higher than 150 m) on the Teheran Street from  $(x, y) \sim (4440 \text{ m}, 320 \text{ m})$  to  $(x, y) \sim (6720 \text{ m}, 1180 \text{ m})$  and apartment complexes around  $(x, y) = (3360 \text{ m}, 1320 \text{ m})$  and  $(3480 \text{ m}, 360 \text{ m})$ . There also exists one park (Samneung Park) around  $(x, y) = (6300 \text{ m}, 1560 \text{ m})$ . The airborne light detection and ranging (LIDAR) data with a 1-m grid resolution are used to create coarser gridded elevation data with a 5-m grid resolution. In the selected area, the ground elevation varies from  $\sim 30 \text{ m}$  to  $\sim 90 \text{ m}$ . The ground elevation is included in the gridded elevation data.

To apply a realistic boundary condition in the streamwise direction, the turbulence recycling method (Kataoka and Mizuno 2002; Lund et al. 1998) is

employed to generate turbulent inflow data for the main domain. A subdomain where turbulence is recycled is added in the upstream of the main domain. In the recycling domain, turbulent signals (perturbations from the horizontal average over the recycling domain) at the outflow boundary are repeatedly imposed at the inflow boundary, while initial mean vertical profiles (obtained from a precursor simulation) at the inflow boundary do not change during the simulation. In addition to the recycling domain, buffer regions are added around the lateral boundaries of the main domain. In the buffer regions, the variation of ground elevation is smoothed out toward the lateral boundaries of the computational domain to avoid a discontinuity in ground elevation and in-line arranged artificial buildings are located to prevent abrupt dissipation of turbulence there. The size of the computational domain is 7680 m in the  $x$  (east–west) direction, 2400 m in the  $y$  (south–north) direction, and 1020 m in the  $z$  (vertical) direction. The grid size in the  $x$  and  $y$  directions is 5 m. The grid size in the  $z$  direction is uniform with 5 m up to  $z = 250$  m and increases with an expansion ratio of 1.08 up to  $z \sim 325$  m, then being 10 m above that height. For velocity components and SGS TKE, the radiation boundary condition is applied at the east (outflow) boundary and the cyclic boundary condition is applied at the south and north boundaries. The Dirichlet boundary condition is applied at the top boundary. Westerly geostrophic wind ( $U_g = 10 \text{ m s}^{-1}$ ) is imposed in the model domain, and

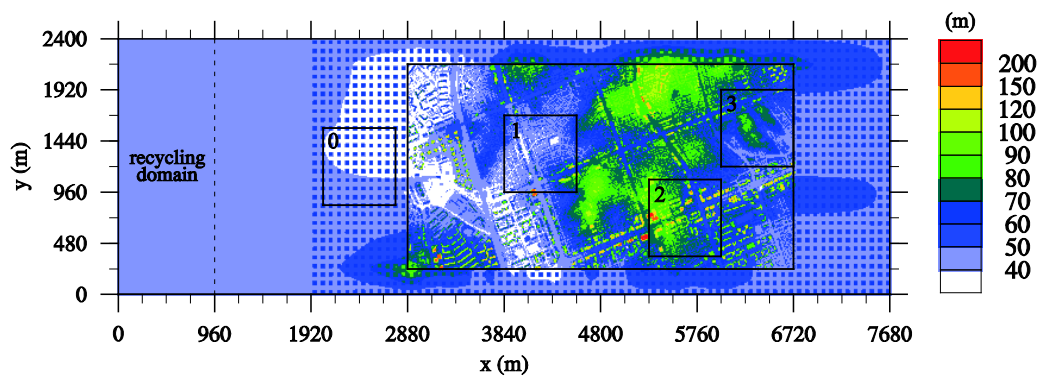


Figure 7.1. Elevation field of ground and building top surfaces in the computational domain. The main domain and the areas of interest are indicated by inner rectangle with a solid line and squares with solid lines, respectively.

the Coriolis force induces anti-clockwise turning of mean wind direction downward in the boundary layer. At grid points closest to all the solid surfaces, the MO similarity is employed in the momentum equation. The roughness length for momentum is 0.1 m. To obtain initial perturbations and mean vertical profiles in the recycling domain, a 2-h precursor simulation with a flat surface and cyclic boundary conditions at the lateral boundaries is conducted. Then, PALM is integrated for 2400 s and the last 30-min simulation data are used for analysis.

## 7.2 Turbulence statistics

Figure 7.2a shows the field of mean streamwise velocity  $\bar{u}$  at  $z = 100$  m. At  $z = 100$  m, large wakes appear behind apartment complexes and are located around  $(x, y) = (3600 \text{ m}, 1200 \text{ m})$ ,  $(3840 \text{ m}, 420 \text{ m})$ , and so on. An elongated area of low streamwise velocity, where small wakes are aligned and connected to each other, appears around the buildings on the Teheran Street. The mean streamwise velocity at  $z = 100$  m is high in the Samneung Park due to the absence of high-rise buildings. To find areas where momentum is actively transported downward by turbulence, the vertical turbulent momentum flux at every grid point in the main domain is vertically integrated from  $z_1 = 0$  m to  $z_2 = 600$  m and then divided by the height difference  $z_2 - z_1$ . Figure 7.2b shows the

field of column-averaged vertical turbulent momentum flux  $\frac{1}{(z_2 - z_1)} \int_{z_1}^{z_2} \overline{u'w'} dz$ .

$u'$  and  $w'$  denote deviations from the time-averaged (mean) streamwise velocity  $\bar{u}$  and vertical velocity  $\bar{w}$ , respectively. The magnitude of column-averaged vertical turbulent momentum flux is large behind apartment complexes and the two high-rise buildings on the Teheran Street. The two areas are selected as the areas of interest (denoted by area 1 and area 2, respectively). The regions of large-magnitude column-averaged vertical turbulent momentum flux extend downstream. Although there are no high-rise buildings in the Samneung Park area, the magnitude of column-averaged vertical turbulent momentum flux is quite large there. Thus, the area around the Samneung Park is also selected as the area of interest (denoted by area 3). One area located upstream of the main domain (denoted by area 0) is selected to compare turbulence statistics in the three areas of interest to upstream turbulence statistics (Fig. 7.1).

The vertical profiles of mean streamwise velocity, vertical velocity variance, and vertical turbulent momentum flux averaged over the four areas are plotted in Fig. 7.3. The mean streamwise velocity below  $z \sim 200$  m is higher in the upstream area (area 0) than in the other three areas (area 1, area 2, and area 3). The magnitudes of vertical velocity variance and vertical turbulent momentum flux in the three areas are overall much larger than those in the upstream area,

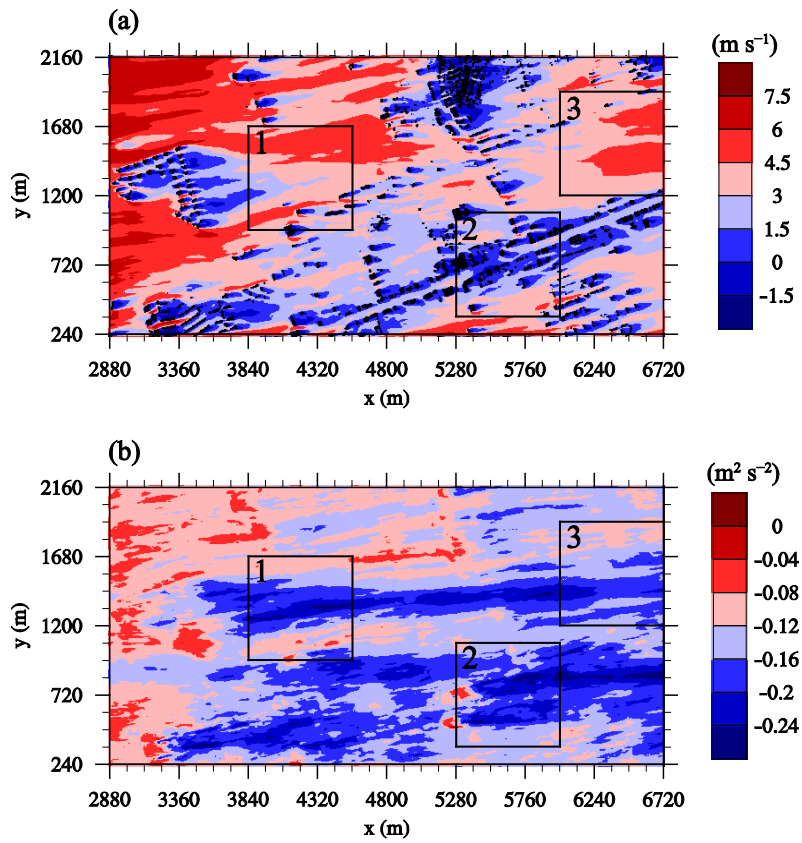


Figure 7.2. Fields of (a) mean streamwise velocity at  $z = 100$  m and (b) column-averaged vertical turbulent momentum flux. The areas of interest are indicated by squares with solid lines.

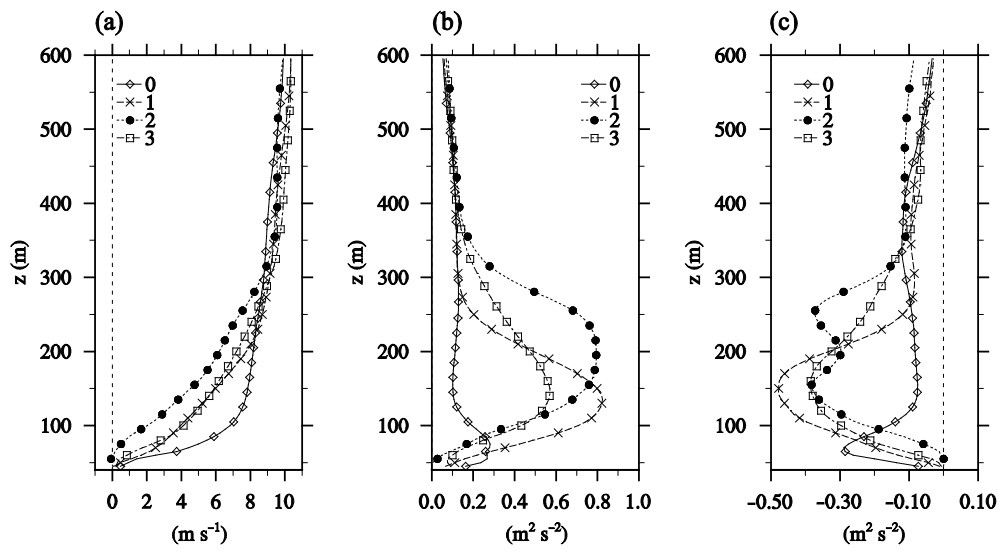


Figure 7.3. Vertical profiles of area-averaged (a) mean streamwise velocity, (b) vertical velocity variance, and (c) vertical turbulent momentum flux in the four areas.

indicating an enhancement of turbulence in a densely built-up urban area. The vertical velocity variance in area 1 has a maximum value at  $z \sim 130$  m, slightly above the average top height of upstream apartment buildings. The magnitude of vertical velocity variance in area 2 is also large around the top heights of high-rise buildings. The vertical turbulent momentum flux in area 1 has a maximum magnitude at  $z \sim 150$  m, and that in area 2 has two local maximum peaks at  $z \sim 150$  m and 250 m. The mean streamwise velocity below  $z \sim 300$  m is lower in area 2 than in the other areas due to dense high-rise buildings. In area 3, the vertical turbulent momentum flux has a maximum magnitude at  $z \sim 150$  m and the shape of the vertical profile is quite similar to that averaged over the main domain (not shown). Based on the analysis of turbulence statistics, three analysis heights (100 m for the main domain, 150 m for area 1, and 250 m for area 2) are selected.

Figure 7.4 shows the field of the joint probability density function (PDF) of  $u'$  and  $w'$  and the field of  $u'w'$  multiplied by the joint PDF at  $z = 100$  m in the main domain, 150 m in area 1, and 250 m in area 2. Dashed lines of equal  $|u'w'|$  ( $2 \text{ m}^2 \text{ s}^{-2}$ ) are added in Fig. 4 to indicate the strength of turbulent events. The joint PDF of  $u'$  and  $w'$  is calculated using the same expression in section 4  $f_{u',w'}(a_i, a_j) = P(a_i - 0.5\Delta a < u' \leq a_i + 0.5\Delta a, a_j - 0.5\Delta a < w' \leq a_j + 0.5\Delta a)$ . The number in each direction ( $N$ ) and spacing ( $\Delta a$ ) of bins used to calculate the joint

PDF are 50 and 0.2, respectively. Note that the sum of all joint PDFs

$\sum_{i=1}^N \sum_{j=1}^N f_{u',w'}(a_i, a_j)$  is 1. The joint PDF and  $u'w'$  multiplied by the joint PDF

illustrate the frequency of the four turbulent events and their contribution to vertical turbulent momentum flux, respectively.

The results at  $z = 100$  m in the main domain show a typical pattern, that is, momentum is transported downward mostly by ejections and sweeps in the atmospheric boundary layer (Fig. 7.4d). The results at other heights in the main domain show similar patterns. The field of joint PDF and the field of  $u'w'$  multiplied by the joint PDF at  $z = 150$  m in area 1 show that stronger turbulent events occur more frequently at all quadrants than the average pattern in the main domain, inducing stronger vertical turbulent momentum flux at that height (Fig. 7.3c). The joint PDF field at  $z = 250$  m in area 2 illustrates the effects of high-rise buildings and wakes behind them. The center of joint PDF moves from the origin to the fourth quadrant and the elliptical shape extends more to the second quadrant, indicating that sweeps occur more frequently and ejections become stronger than the average pattern in the main domain (Fig. 7.4a). The role of ejections in the vertical turbulent momentum transport can be confirmed again in the field of  $u'w'$  multiplied by the joint PDF (Fig. 7.4f). In the downstream of the apartment complex, all the quadrant events become stronger

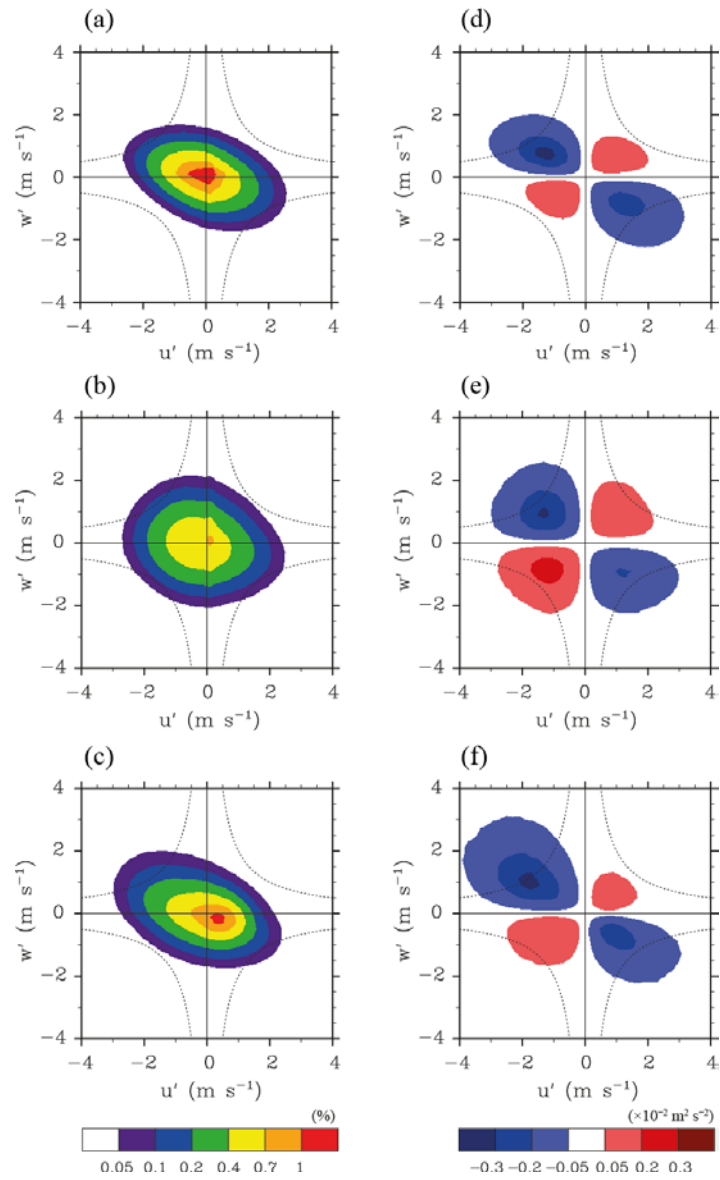


Figure 7.4. Fields of the joint probability density function of  $u'$  and  $w'$  at (a)  $z = 100$  m in the main domain, (b)  $z = 150$  m in area 1, and (c)  $z = 250$  m in area 2

and  $u'w'$  multiplied by the joint probability density function at (d)  $z = 100$  m in the main domain, (e)  $z = 150$  m in area 1, and (f)  $z = 250$  m in area 2. Dashed lines of equal  $|u'w'|$  ( $2 \text{ m}^2 \text{ s}^{-2}$ ) are added.

(Fig. 7.4e). In the area behind the high-rise buildings, on the other hand, only ejections become stronger (Fig. 7.4f). This seems to be related to the wakes and vortices that appear behind the high-rise buildings.

### 7.3 Turbulent flow behind an apartment complex

Figure 7.5 shows the fields of vertical turbulent momentum flux, instantaneous streamwise velocity at  $t = 1965$  s, and  $\text{sgn}(w') \cdot \max(0, -u'w')$  at  $t = 1965$  s in the  $x$ - $z$  plane ( $y = 1257.5$  m). The contours of mean or instantaneous streamwise velocity of  $5 \text{ m s}^{-1}$  are added. The quantity  $\text{sgn}(w') \cdot \max(0, -u'w')$  extracts ejection ( $u'_-w'_+$ ) and sweep ( $u'_+w'_-$ ) events among the four quadrant events, and ejection and sweep events correspond to positive and negative values of the quantity, respectively (subsection 3.3). The magnitude of vertical turbulent momentum flux is large just behind each apartment building due to locally generated turbulent eddies. There appears a large region of strong vertical turbulent momentum flux farther downstream of the apartment complex. Strong vertical momentum transport events usually occur around an interface between low-speed air and high-speed air, and the interface can be captured by plotting interfacial streamwise velocity. Even in this kind of complex turbulent flow, the interface between low-speed air and high-speed air can be captured simply by plotting the contours of streamwise velocity ( $5 \text{ m s}^{-1}$  in the present simulation)

and strong vertical momentum transport events such as ejections and sweeps occur along the interface (Fig. 7.5c). As going downstream from the apartment complex, an interfacial region around the interface (e.g.,  $2 \text{ m s}^{-1} < u < 6 \text{ m s}^{-1}$ ) extends downward and it also extends upward ( $x > 3840 \text{ m}$ ). In the vertically extended interfacial region, overall magnitude and scale of turbulent eddies increase and the increase might be related to the large region of strong vertical turbulent momentum flux farther downstream. It is also possible that the large wake (Fig. 7.2a), which appears as a result of combined smaller wakes, induces spanwise converging flow around the wake and the converging flow results in strong vertical turbulent momentum flux above the wake.

Conditionally averaged streamwise velocity perturbation and velocity perturbation vector fields corresponding to ejections and sweeps in area 1 are shown in Fig. 7.6. Local minimum points of  $u'w'$  in the  $x$ - $y$  plane ( $z = 150 \text{ m}$ ) satisfying a certain criterion (e.g.,  $u'w' < -2 \text{ m}^2 \text{ s}^{-2}$ ) are collected, and the data around the minimum points are transformed to a new coordinate ( $x', y', z$ ) and averaged to extract characteristic flow structures of turbulent eddies (subsection 4.3). At  $z = 150 \text{ m}$  in area 1, ejections and sweeps are comparable in frequency and magnitude (Fig. 7.4e) and the conditionally averaged fields composed of ejections and sweeps do not show distinct structures due to their opposite directions. To see distinct structures, samples of ejections and those of sweeps

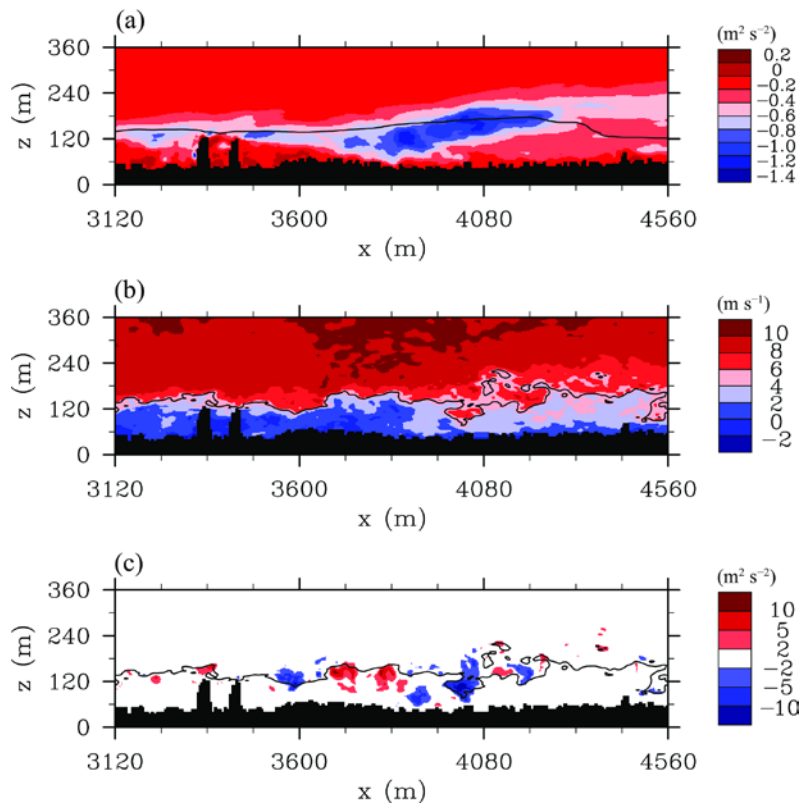


Figure 7.5. Fields of (a) vertical turbulent momentum flux, (b) instantaneous streamwise velocity at  $t = 1965$  s, and (c)  $\text{sgn}(w') \cdot \max(0, -u'w')$  at  $t = 1965$  s in the  $x$ - $z$  plane ( $y = 1257.5$  m). The contours of streamwise velocity ( $5 \text{ m s}^{-1}$ ) are added.

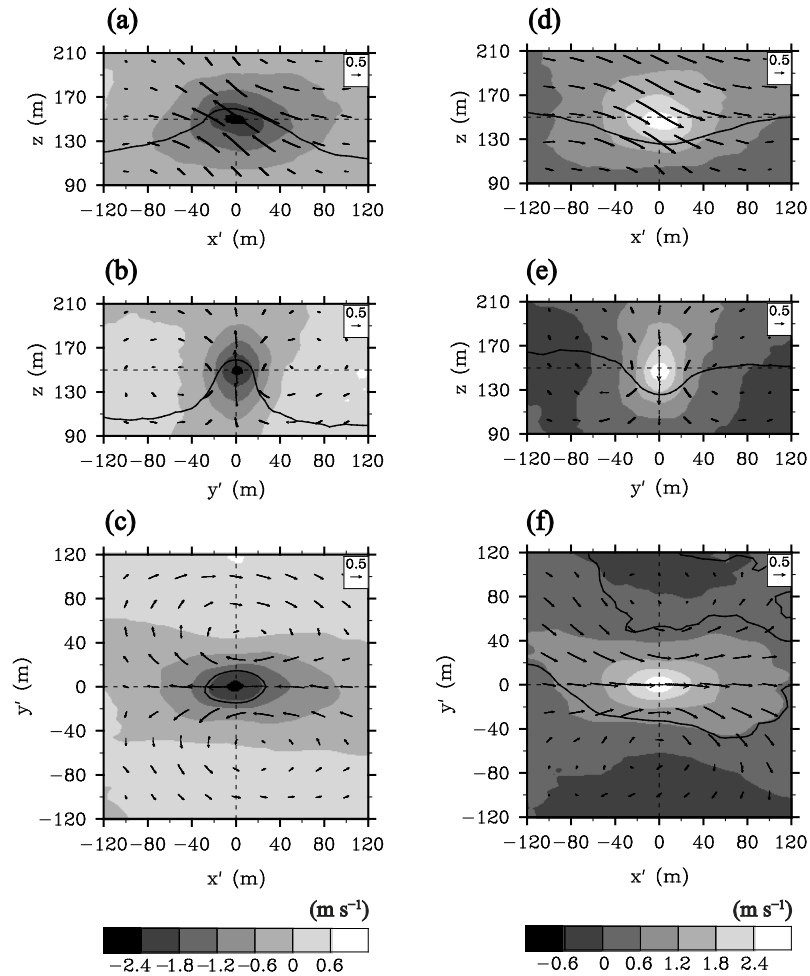


Figure 7.6. Conditionally averaged  $u'$  and velocity perturbation vector ( $u'$ ,  $v'$ ,  $w'$ ) fields of ejections in the (a)  $x'$ - $z$  plane ( $y' = 0$  m), (b)  $y'$ - $z$  plane ( $x' = 0$  m), and (c)  $x'$ - $y'$  plane ( $z = 150$  m) and the same fields of sweeps in the (d)  $x'$ - $z$  plane ( $y' = 0$  m), (e)  $y'$ - $z$  plane ( $x' = 0$  m), and (f)  $x'$ - $y'$  plane ( $z = 150$  m). These are for area 1. The contours of streamwise velocity ( $4 \text{ m s}^{-1}$  for ejections and  $6 \text{ m s}^{-1}$  for sweeps) are added.

are collected and averaged separately by applying an additional criterion (a sign of vertical velocity perturbation). The velocity perturbation vector  $(u', v', w')$  instead of  $(u, v, w)$  are plotted to illustrate the relative motion of turbulent eddies with respect to the mean flow. The conditionally averaged flow fields show that negative and positive streamwise velocity perturbations are well correlated with updrafts (ejections) and downdrafts (sweeps), respectively. The flow structure of ejections is quite similar to the typical turbulence coherent structure above cubical building arrays (Coceal et al. 2007).

## 7.4 Turbulent flow behind high-rise buildings

Figure 7.7 shows the fields of vertical turbulent momentum flux in the  $x$ - $z$  plane ( $y = 552.5$  m), instantaneous vertical velocity at  $t = 2385$  s in the  $x$ - $y$  plane ( $z = 250$  m), streamwise vorticity at  $t = 2385$  s in the  $x$ - $y$  plane ( $z = 250$  m), and  $\text{sgn}(w') \cdot \max(0, -u'w')$  at  $t = 2385$  s in the  $x$ - $y$  plane ( $z = 250$  m). The contours of mean or instantaneous streamwise velocity of  $5 \text{ m s}^{-1}$  are added. Wakes behind the high-rise buildings and their fluctuating (south and north) features are captured by the contours of streamwise velocity. The fluctuating turbulent wakes are well-known fluid phenomena (usually occurring behind a cylinder), and they seem to be related to downstream ejections. At  $z = 250$  m (near the top height of the tallest building), turbulent eddies that penetrate into

the building wakes induce spanwise and vertical vortices behind the buildings and parts of the vortices become streamwise vortices due to wind shear (Fig. 7c). Strong updrafts appear with the streamwise vortices in the streamwise-elongated wakes and parts of the wakes are detached and advected downstream. Ejections are dominant in both the building-connected wakes and detached wakes, contributing to vertical turbulent momentum transport in the downstream of the buildings (Fig. 7.7d).

Conditionally averaged vertical velocity and velocity perturbation vector fields in area 2 are shown in Fig. 7.8. As shown in Fig. 7.4f, ejections are dominant over sweeps at  $z = 250$  m in area 2. Thus, ejections are distinct in the conditionally averaged fields without any additional criterion. In contrast to ejections in area 1 (Fig. 7.6a–c), ejections in area 2 exhibit a vertically extended shape with strong updrafts, indicating that updraft-induced flow structures behind the high-rise buildings are dominant in transporting momentum downward. The structure of wakes behind the high-rise buildings is also well captured by the contours of streamwise velocity  $5 \text{ m s}^{-1}$  in Fig. 7.8a.

Figure 7.9 shows the fields of turbulent kinetic energy and mean velocity vector and instantaneous wind speed and velocity vector ( $t = 2105$  s) at  $z = 90$  m. In area 2, the west part of the Teheran Street has high ground elevation ( $\sim 80$  m) and the mean velocity there is low at  $z = 90$  m. Except for the high ground

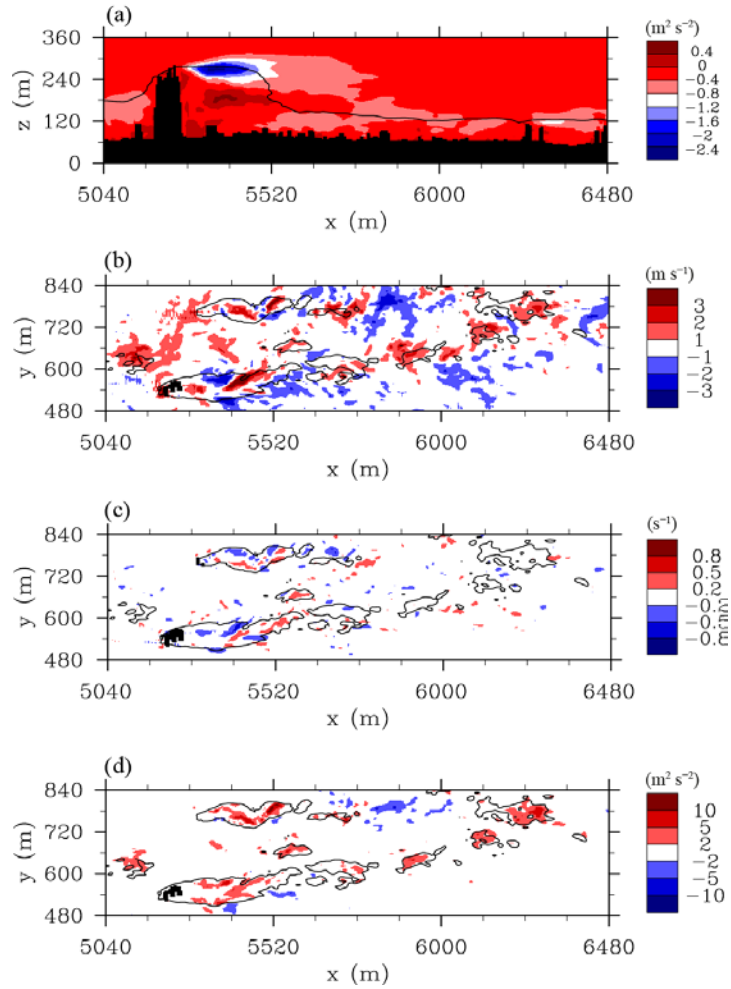


Figure 7.7. Fields of (a) vertical turbulent momentum flux in the  $x$ - $z$  plane ( $y = 552.5$  m), (b) instantaneous vertical velocity at  $t = 2385$  s in the  $x$ - $y$  plane ( $z = 250$  m), (c) streamwise vorticity at  $t = 2385$  s in the  $x$ - $y$  plane ( $z = 250$  m), and (d)  $\text{sgn}(w') \cdot \max(0, -u'w')$  at  $t = 2385$  s in the  $x$ - $y$  plane ( $z = 250$  m). The contours of streamwise velocity ( $5 \text{ m s}^{-1}$ ) are added.

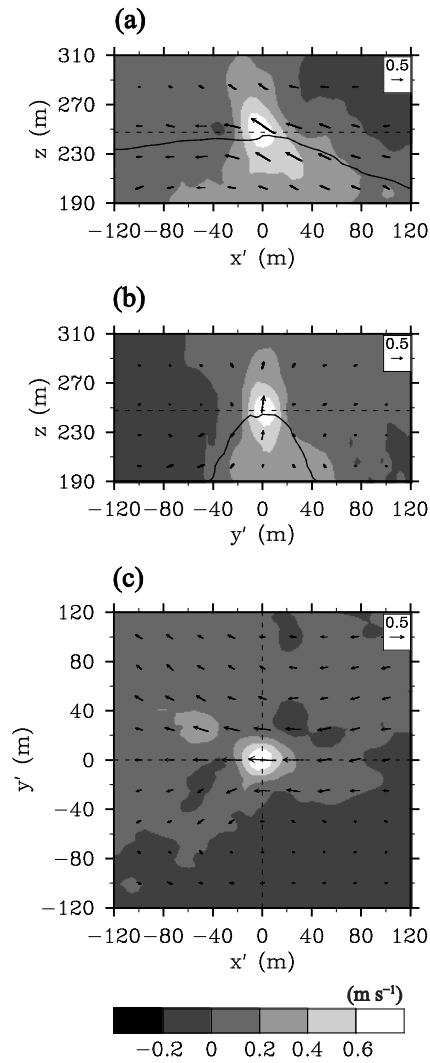


Figure 7.8. Conditionally averaged  $w$  and velocity perturbation vector ( $u'$ ,  $v'$ ,  $w'$ ) fields in the (a)  $x'$ - $z$  plane ( $y' = 0$  m), (b)  $y'$ - $z$  plane ( $x' = 0$  m), and (c)  $x'$ - $y'$  plane ( $z = 250$  m). These are for area 2. The contours of streamwise velocity ( $5 \text{ m s}^{-1}$ ) are added.

elevation region, the mean flow on the Teheran Street blows in the street direction. On the Teheran Street, high-rise buildings exist and they induce downdrafts along their windward walls and updrafts along their leeward walls. The downdrafts along the windward walls induce winding flow and high turbulent kinetic energy near the ground surface, and the momentum transported by the downdrafts is transported into nearby streets (Fig. 7.9a). This kind of flow system is more distinct in the instantaneous flow field. Around the building at  $(x, y) \sim (5670 \text{ m}, 870 \text{ m})$ , a high wind speed pattern, which is mostly induced by downdrafts at the windward wall of the building, and an extension of high wind speed to the Teheran Street are distinct (Fig. 7.9b). Thus, not only the direction of street but also the arrangement of high-rise buildings on the street is important to the direction and strength of wind on the street.

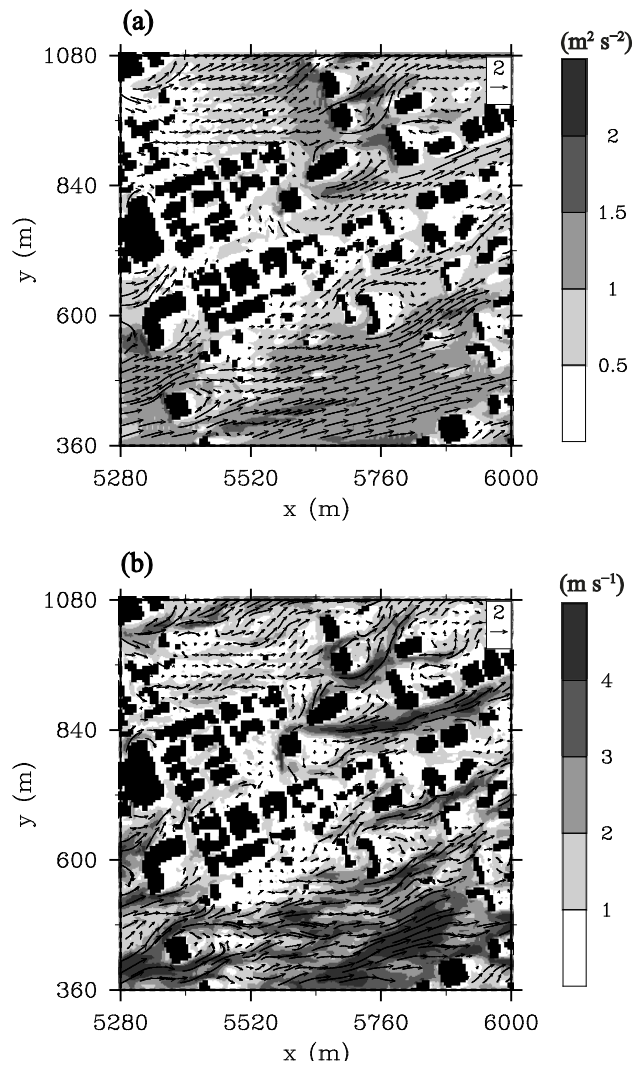


Figure 7.9. Fields of (a) turbulent kinetic energy and mean velocity vector and (b) instantaneous wind speed and velocity vector ( $t = 2105$  s) at  $z = 90$  m.

## 7.5 Turbulent flow in a park area

As indicated by the streamwise-directed band (at  $y \sim 1440$  m) in Fig. 7.2b, the column-averaged vertical turbulent momentum flux in area 3 is not negligible despite the absence of high-rise buildings. This is attributed to the vertical growth of internal boundary layer. Figure 7.10 shows the fields of vertical turbulent momentum flux, instantaneous streamwise velocity at  $t = 2065$  s, and  $\text{sgn}(w') \cdot \max(0, -u'w')$  at  $t = 2065$  s in the  $x$ - $z$  plane ( $y = 1440$  m). The contours of streamwise velocity of  $5 \text{ m s}^{-1}$  and those of  $8 \text{ m s}^{-1}$  are added. As going to downstream, the magnitude of vertical turbulent momentum flux decreases near the ground but the internal boundary layer develops upward as indicated by the vertical turbulent momentum flux field. As a result, the magnitude of vertical turbulent momentum flux at high levels increases toward downstream (Fig. 7.10a). As the internal boundary layer extends vertically toward downstream, the interface between low-speed air and high-speed air becomes less distinct while the interfacial region (e.g.,  $5 \text{ m s}^{-1} < u < 8 \text{ m s}^{-1}$ ) broadens in the vertical direction. As shown in Fig. 7.10c, ejections and sweeps appear at higher levels than those in the upstream area (Fig. 7.5c). Some ejections and sweeps appear around the interface of streamwise velocity  $5 \text{ m s}^{-1}$ , and others appear around the new higher interface of streamwise velocity  $8 \text{ m s}^{-1}$ . Figure 7.10c indicates that

the distribution of turbulent eddies in area 3 is complex despite the absence of high-rise buildings.

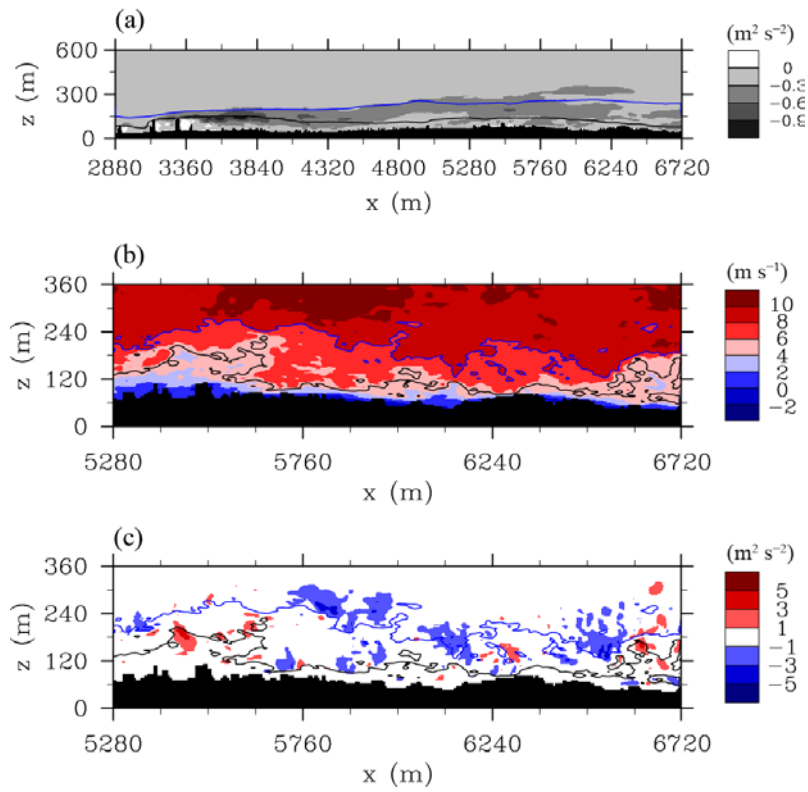


Figure 7.10. Fields of (a) vertical turbulent momentum flux, (b) instantaneous streamwise velocity at  $t = 2065$  s, and (c)  $\text{sgn}(w') \cdot \max(0, -u'w')$  at  $t = 2065$  s in the  $x$ - $z$  plane ( $y = 1440$  m). The contours of streamwise velocity of  $5 \text{ m s}^{-1}$  (black) and those of  $8 \text{ m s}^{-1}$  (blue) are added.

# **8 Impact of mesoscale wind on turbulent flow in a densely built-up urban area**

## **8.1 Experimental design**

To simulate turbulent flow in a densely built-up area of Seoul for 0900–1500 LST 31 May 2008, wind data from the Advanced Research Weather Research and Forecasting (WRF) model (Skamarock et al. 2008) are used as the lateral boundary conditions of the LES model. Here, WRF model version 3.2 with the Seoul National University Urban Canopy Model (SNUUCM; Ryu et al. 2011) is used. The experimental setup and physical parameterization options are summarized in Table 8.1. Five two-way nested computational domains are considered (Fig. 8.1a), and the horizontal grid sizes are 27, 9, 3, 1, and 0.333 km. The innermost domain covers Seoul metropolitan area and includes the main domain of the LES model (Fig. 8.1b). There are 43 vertical layers below the model top (20 hPa), and 16 vertical layers exist below 2 km to better resolve the lower atmosphere (close to the surface). A clear day with a slight variation of wind direction is considered here, and the day 31 May 2008 is selected as the case. The WRF model is integrated for 48 h, starting from 0000 UTC 30 May 2008. The National Centers for Environmental Prediction (NCEP) final analysis

data with  $1^\circ \times 1^\circ$  horizontal resolution and 6-h interval are used as the initial and boundary conditions in the WRF simulation. WRF single-moment 6-class microphysics scheme (Hong and Lim 2006) is used to represent the cloud processes, and the updated Kain-Fritsch convective scheme (Kain 2004) as a cumulus parameterization scheme is applied for the first and second domains. Radiative processes are represented with the Dudhia shortwave radiation scheme (Dudhia 1989) and the Rapid Radiative Transfer Model longwave radiation scheme (Mlawer et al. 1997). The planetary boundary layer processes are represented with the Yonsei University planetary boundary layer scheme (Hong et al. 2006), and the Noah land surface model (Chen and Dudhia 2001) is used.

A similar experimental setup (except turbulent inflow data) applied in section 7 is adopted here. As in section 7, a turbulence-recycling subdomain is added in the upstream (west) of the main domain and turbulent signals at the outflow boundary of the subdomain are repeatedly imposed at the inflow boundary. In the present LES simulation, interpolated velocity components  $u$  and  $v$  from the WRF model (instead of fixed mean velocities from the precursor simulation) are added to the recycled turbulent signals and the combined data are used as turbulent inflow data (at the west boundary). The cyclic boundary condition is applied at the south and north lateral boundaries as in section 7. PALM is integrated for 6 h starting from 0000 UTC 31 May 2008,

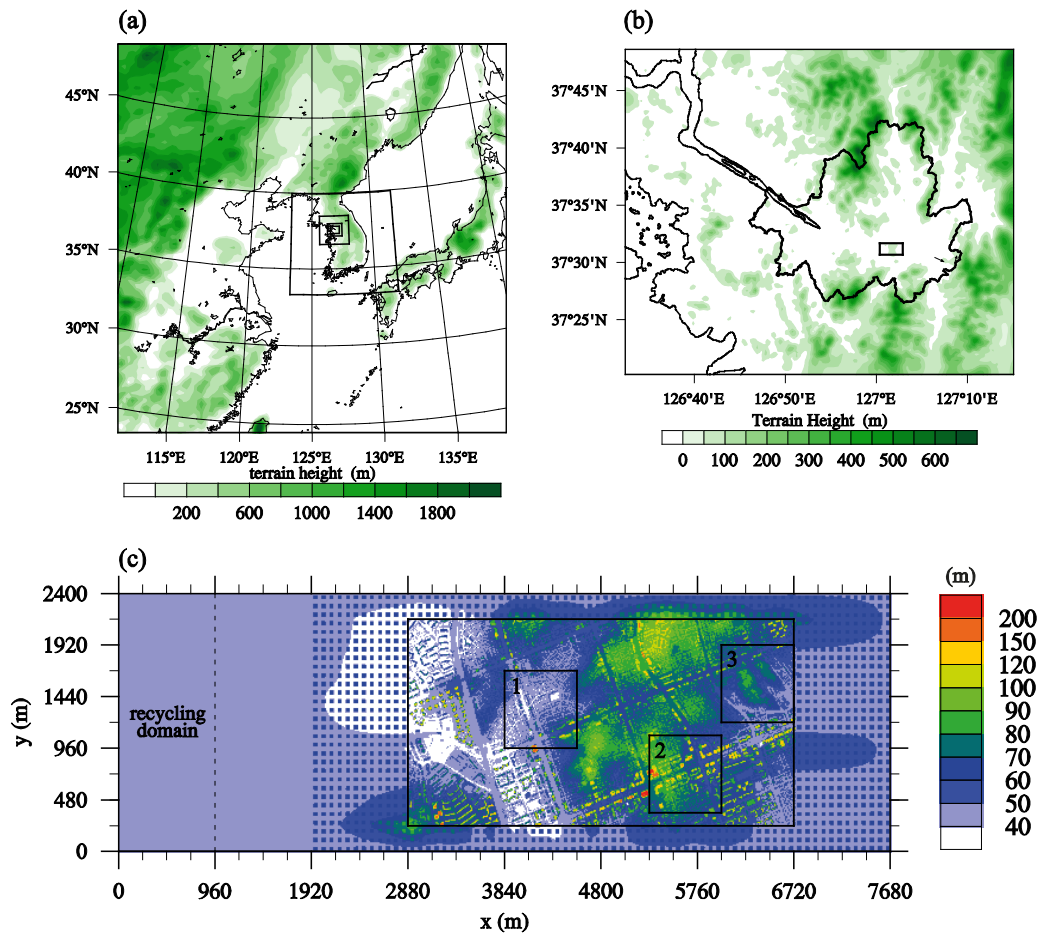


Figure 8.1. (a) Five domains and (b) innermost domain in the WRF-SNUUCM simulation with terrain height (shaded). (c) Elevation field of ground and building top surfaces in the LES domain. The main domain is indicated by inner rectangle with solid lines in (b) and (c), and the areas of interest are indicated by squares with solid lines in (c).

Table 8.1. Experimental design in the WRF simulation.

|                              | Domain 1  | Domain 2 | Domain 3 | Domain 4 | Domain 5 |
|------------------------------|---|----------|----------|----------|----------|
| Horizontal grids             | 108×108   | 81×81    | 69×69    | 102×90   | 189×159  |
| Vertical layers              | 43  |          |          |          |          |
| Horizontal grid spacing (km) | 27  | 9        | 3        | 1        | 0.333    |
| Time integration (h)         | 48 (from 00 UTC 30 May 2008)                                |          |          |          |          |
| Time step (s)                | 60  | 20       | 6.7      | 2.2      | 0.7      |
| Microphysics                 | WRF single-moment 6-class                                   |          |          |          |          |
| Cumulus                      | Kain-Fritsch  |          | none     |          |          |
| LW radiation                 | RRTM  |          |          |          |          |
| SW radiation                 | Dudhia shortwave radiation                                  |          |          |          |          |
| PBL                          | YSU PBL   |          |          |          |          |
| LSM                          | Noah LSM  |          |          |          |          |
| Initial/boundary conditions  | NCEP final analysis data (6-h interval, 1° × 1° resolution) |          |          |          |          |

and 600-s simulation data during seven periods (0900–0910 LST, 1000–1010 LST, 1100–1110 LST, 1200–1210 LST, 1300–1310 LST, 1400–1410 LST, and 1450–1500 LST 31 May 2008) are analyzed.

The WRF-simulated surface air temperature and wind are validated by calculating hit rates. Hit rates of WRF-simulated 2-m temperature, 10-m wind speed, and 10-m wind direction are calculated using the observation data from 9 AWS stations in Seoul. The accuracy ranges of temperature, wind speed, and wind direction are  $\pm 2^{\circ}\text{C}$ ,  $\pm 1 \text{ m s}^{-1}$ , and  $\pm 30^{\circ}$  (Ries and Schlünzen 2009). The calculated hit rates of temperature, wind speed, and wind direction are 87.1%, 56.4%, and 56.4%, respectively. Figure 8.2 shows the time series of observed and WRF-simulated wind speed and that of wind direction at the Gangnam AWS station. The simulated wind speed in the daytime is little higher than the observed one, and the change of wind direction ( $\sim 60^{\circ}$ ) around 0900 LST 31 May 2008 is not simulated in the WRF model. Despite the discrepancies, the diurnal cycles of wind speed and temperature (not shown) and overall flow direction are well simulated.

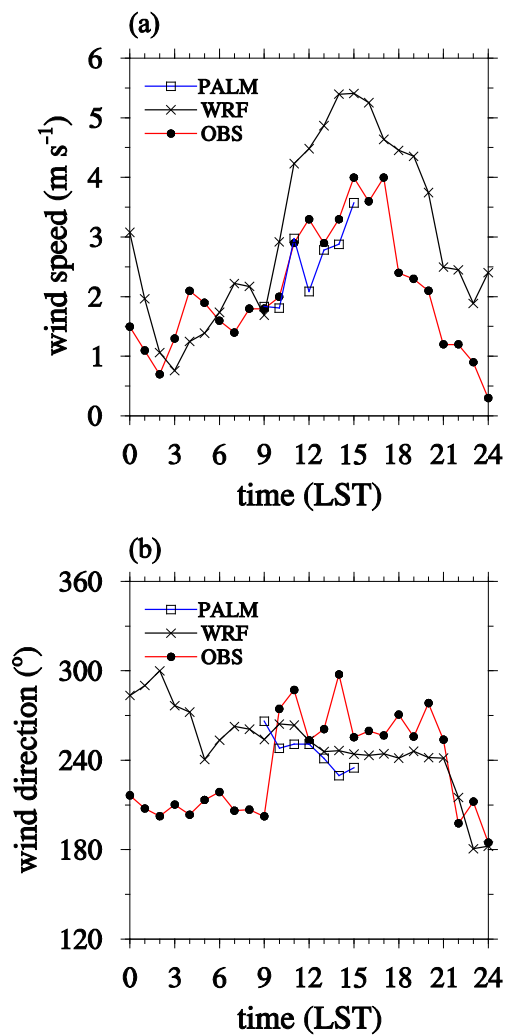


Figure 8.2. Diurnal variations of observed and WRF-simulated (a) wind speed and (b) wind direction near the surface on 31 May 2008. The observation was made at the Gangnam AWS station, and the PALM-simulated data are added.

## 8.2 Turbulent flow in a densely built-up urban area

Figure 8.3 shows the vertical profiles of mean streamwise velocity, mean spanwise velocity, and vertical turbulent momentum flux averaged over the main domain for 0900–0910 LST, 1100–1110 LST, 1300–1310 LST, and 1450–1500 LST 31 May 2008. The magnitude of streamwise velocity increases during the 6-h simulation period, and the vertical gradient of streamwise velocity above  $z \sim 200$  m decreases as planetary boundary layer (PBL) develops in the daytime. While the wind direction near the surface changes a little during the period (Fig. 8.2b), wind direction above  $z \sim 200$  m changes more than that near the surface. As time goes on, the vertical gradient of spanwise velocity above  $z \sim 200$  m also decreases due to strengthened PBL mixing. It is noticeable that the magnitude of vertical turbulent momentum flux for 0900–0910 LST increases with height (Fig. 8.3c). This indicates that turbulence induced by mesoscale wind (above the surface layer) can be stronger than that induced by buildings in the building canopy layer. As time goes on, the turbulence in the building canopy layer strengthens while that above the building canopy layer weakens.

Figure 8.4 shows the fields of the joint PDFs of  $u'$  and  $w'$  for 0900–0910 LST and 1450–1500 LST and  $u'w'$  multiplied by the joint PDFs for 0900–0910

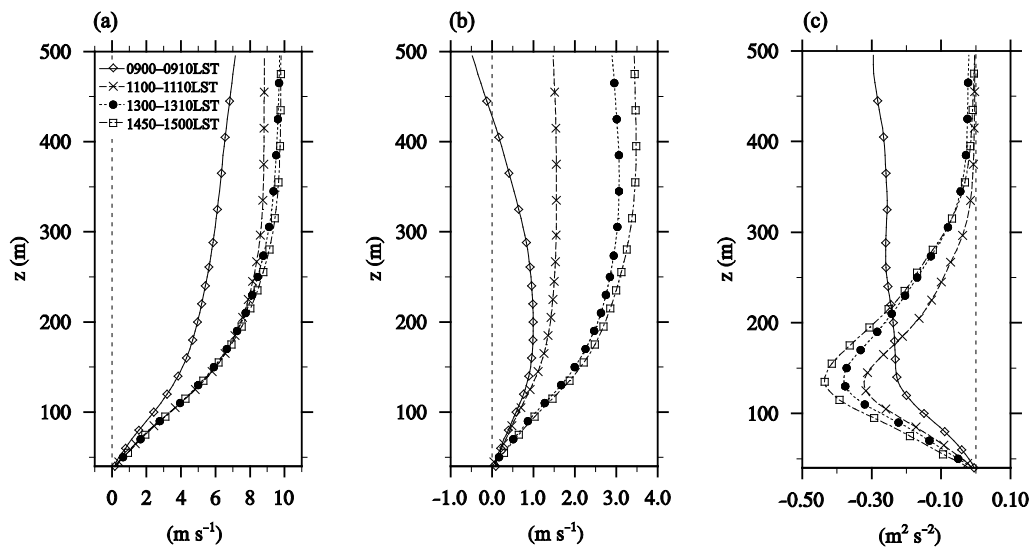


Figure 8.3. Vertical profiles of area-averaged (a) mean streamwise velocity, (b) mean spanwise velocity, and (c) vertical turbulent momentum flux in the main domain for 0900–0910 LST, 1100–1110 LST, 1300–1310 LST, and 1450–1500 LST 31 May 2008.

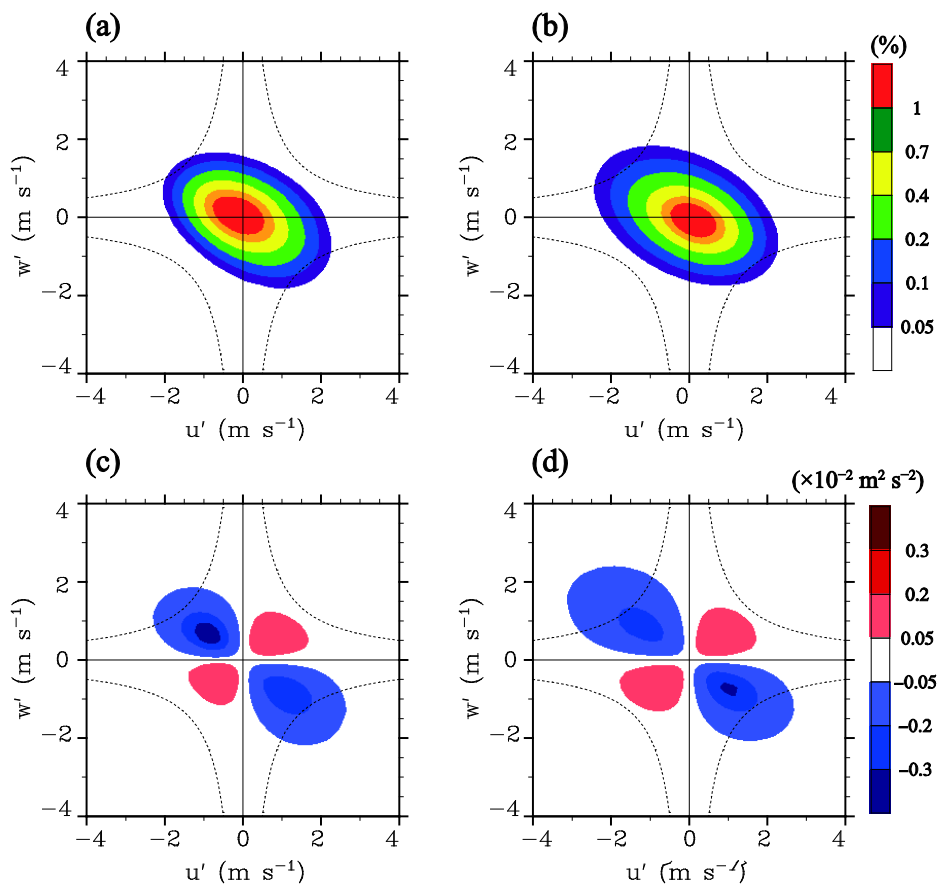


Figure 8.4. Fields of the joint probability density function of  $u'$  and  $w'$  at  $z = 200$  m in the main domain for (a) 0900–0910 LST and (b) 1450–1500 LST and  $u'w'$  multiplied by the joint probability density function at  $z = 100$  m in the main domain for (c) 0900–0910 LST and (d) 1450–1500 LST. Dashed lines of equal  $|u'w'|$  (2 m<sup>2</sup> s<sup>-2</sup>) are added

LST and 1450–1500 LST at  $z = 200$  m in the main domain. It seems that the center of PDFs moves from the second quadrant (ejection) to fourth quadrant (sweep) with time, indicating that sweeps occur more frequently for 1450–1500 LST than for 0900–0910 LST at  $z = 200$  m. The fields of  $u'w'$  multiplied by the joint PDFs also indicates that strong ejections and weaker sweeps play a dominant role in transporting momentum downward for 1450–1500 LST while strong sweeps and weaker ejections play a dominant role in transporting momentum downward for 0900–0910 LST (Figs. 8.4c,d).

Figure 8.5 shows conditionally averaged vertical velocity perturbation and velocity perturbation vector fields for 0900–0910 LST and 1450–1500 LST. Data around the local minimum points of  $u'w'$  in the  $x$ - $y$  plane ( $z = 200$  m), satisfying a certain criterion (e.g.,  $u'w' < -2 \text{ m}^2 \text{ s}^{-2}$ ), are sampled and averaged to extract the dominant turbulence coherent structures during each period. As shown in Fig. 8.4, sweeps induced by upper flow and ejections (that might be induced by buildings) are dominant for 0900–0910 and 1450–1500 LST, respectively. The coherent structure for 0900–0910 LST is inclined toward the south, and its scale is quite large. In contrast, the coherent structure for 1450–1500 LST does not show any directional tendency in spanwise direction and its scale is less than 100 m. The coherent structure for 1450–1500 LST seems to be induced by buildings or building-induced flow in the roughness sublayer.

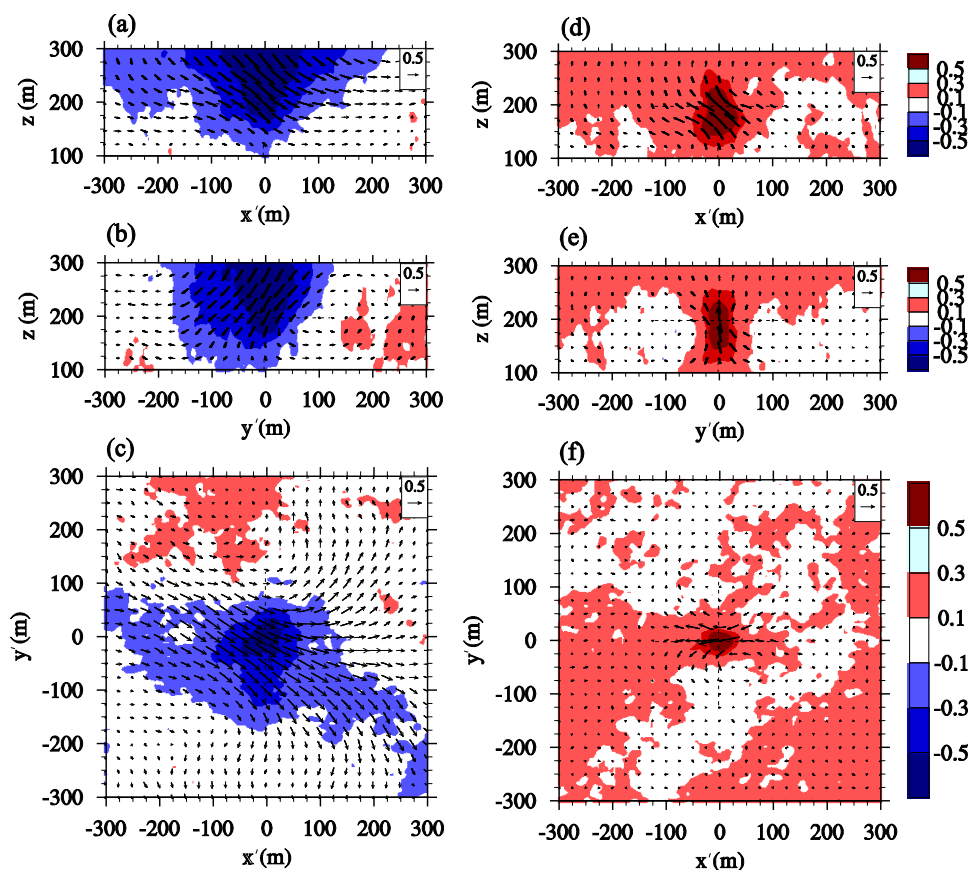


Figure 8.5. Conditionally averaged  $w'$  and velocity perturbation vector ( $u'$ ,  $v'$ ,  $w'$ ) fields for 0900–0910 LST in the (a)  $x'$ - $z$  plane ( $y' = 0$  m), (b)  $y'$ - $z$  plane ( $x' = 0$  m), and (c)  $x'$ - $y'$  plane ( $z = 200$  m) and the same fields for 1450–1500 LST in the (d)  $x'$ - $z$  plane ( $y' = 0$  m), (e)  $y'$ - $z$  plane ( $x' = 0$  m), and (f)  $x'$ - $y'$  plane ( $z = 200$  m).

## 8.3 Ventilation

To illustrate ventilation of the densely built-up urban area, the ratio of wind speed at pedestrian level to wind speed at  $z = 500$  m (where flow is not affected by individual surface roughness elements) is calculated (Letzel et al. 2012) and shown in Fig. 8.6. First, the urban area are classified into the area occupied by buildings and the area occupied by streets or a park (without buildings). Wind speed at 2.5 m (pedestrian level) above the bottom surface ( $V_p$ ) in the area without buildings is calculated. Then, the wind speed at pedestrian level is divided by horizontally and temporally (for 600 s) averaged wind speed at  $z = 500$  m ( $V_{500\text{m}}$ ).

Figure 6 shows the velocity ratio field averaged over the total simulation period (6 h). The velocity ratio is high on broad streets (especially on southeast-northwest directed streets) and intersections. High velocity ratio on broad streets might be induced by the mean street-canyon flow (e.g., canyon vortex) or sweeps that occur at the canyon top (over the streets). The velocity ratio is also high around an apartment complex  $((x, y) \sim (3120 \text{ m}, 1200 \text{ m}))$ , but the high ratio might be due to the absence of upstream buildings. In contrast to high velocity ratio on broad streets, the velocity ratio in a dense building district is quite low due to blockage of pedestrian wind.

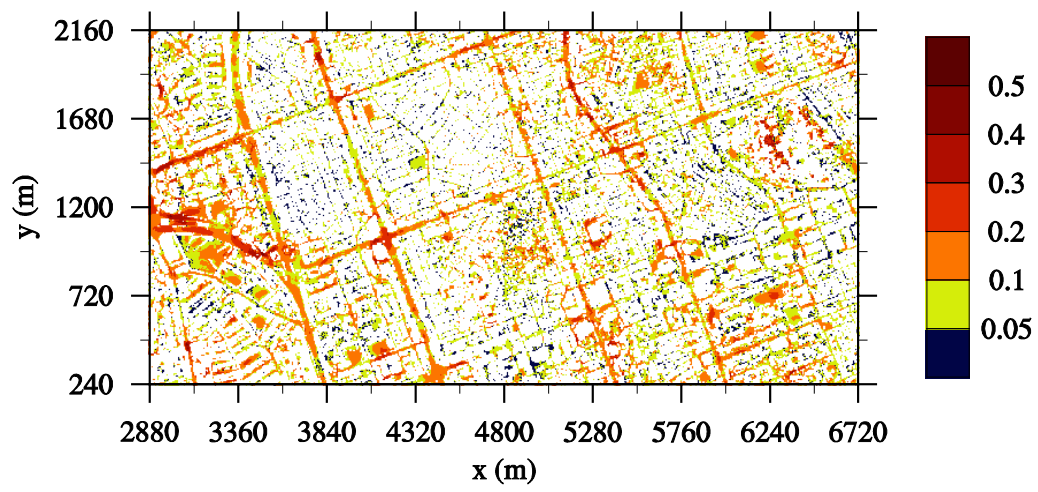


Figure 8.6. Field of time-averaged velocity ratio ( $V_p/V_{500m}$ ) in the main domain.

Figure 8.7 shows area- and time-averaged (for 600 s) velocity ratio, TKE,  $\text{TKE}/(V_{500\text{m}})^2$ , and  $u_{\text{RMS}}/V_{500\text{m}}$ . The velocity ratio averaged over the main domain shows increasing and decreasing trend for 0900–1000 LST. Then, the velocity ratio increases again and decreases from 1030 LST to 1430 LST. In contrast, TKE at the pedestrian level continuously increases from 1010 LST to 1500 LST because of strengthened mesoscale wind. The decrease of the velocity ratio for 1030–1430 LST is partially due to the increased magnitude of mesoscale wind speed (e.g.,  $V_{500\text{m}}$ ), but TKE divided by the square of  $V_{500\text{m}}$  is proportional to the velocity ratio. Instead of TKE, RMS of  $u$  is highly correlated to the velocity ratio during the simulation period (Fig. 8.7d). RMS of  $v$  and that of  $w$  are also highly correlated to the velocity ratio in the main domain (not shown).

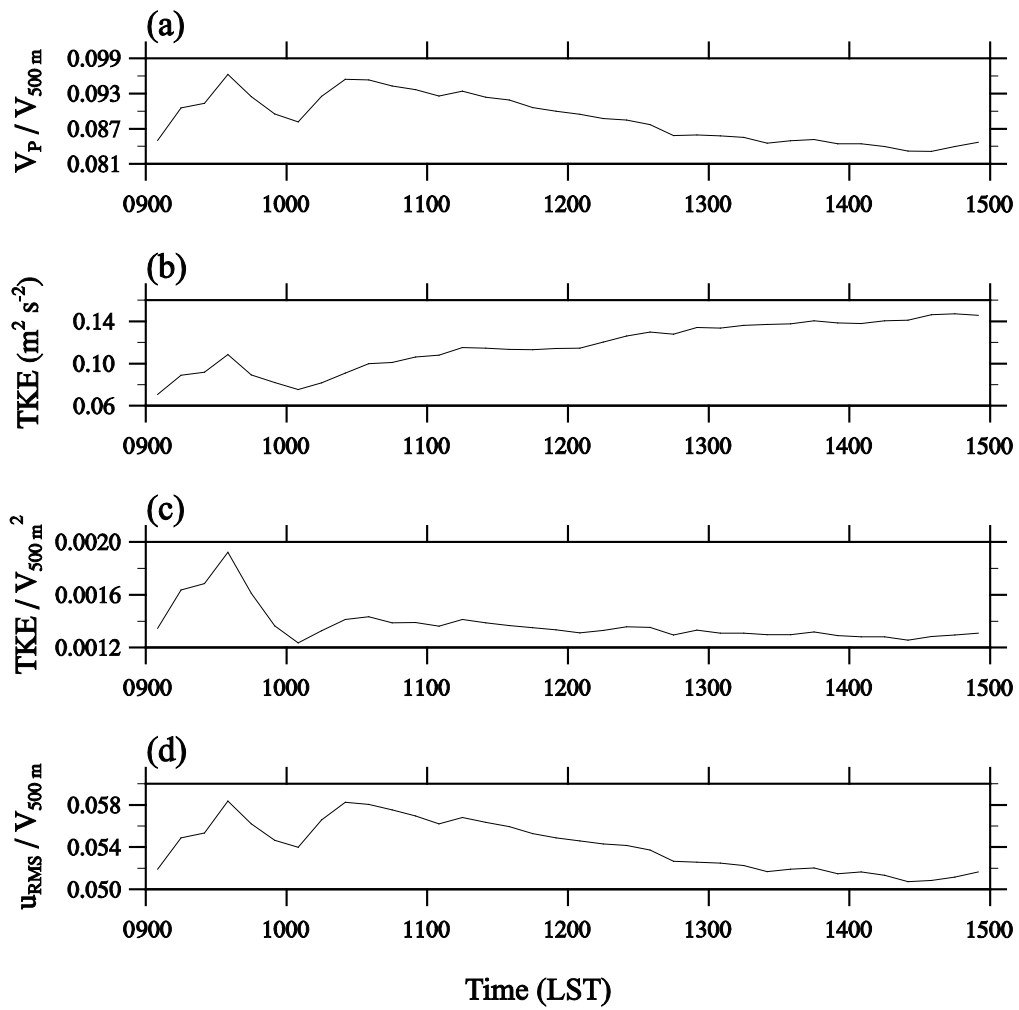


Figure 8.7. Area- and time-averaged (for 600 s) (a) velocity ratio ( $V_P/V_{500\text{m}}$ ), (b) TKE, (c)  $\text{TKE}/(V_{500\text{m}})^2$ , and (d)  $u_{\text{RMS}}/V_{500\text{m}}$ .

## 9 Summary and conclusions

Using an LES model that includes a temperature wall function, turbulent flow and scalar dispersion over heated urban surfaces were investigated. Thermal effects on turbulent flow and scalar dispersion in and above a street canyon with a street aspect ratio of one were examined. Four numerical simulations were performed: no heating (neutral), upwind building wall heating, street bottom heating, and downwind building wall heating cases. A stronger primary vortex in the street canyon appears in the upwind building wall and street bottom heating cases than in the neutral case, and the downwind building wall heating produces an interesting in-canyon flow pattern with a shrunken primary vortex and a winding flow. The differential heating produces higher turbulent kinetic energy and stronger turbulent fluxes at the rooftop height. In the differential heating cases, buoyancy-generated turbulent eddies as well as shear-generated turbulent eddies contribute to the turbulent transport of momentum and scalar and band-shaped or lump-shaped perturbation patterns appear at the rooftop height. At the rooftop height, in the neutral and upwind building wall heating cases, sweep events are less frequent but contribute more to turbulent momentum flux than ejection events. In the street bottom and downwind building wall heating cases, ejection and sweep events are similar in occurrence and their contributions to

turbulent momentum flux are comparable. It was found that these differences are not distinct at a height well above the rooftop.

Thermal effects on turbulent flow in and above an idealized building array were investigated using the LES model. No heating (neutral) and bottom heating cases were simulated and compared to each other. Streaky structures of low-speed regions appear above the isothermal building array, while plume-shaped structures appear with the low-speed streaks above the bottom-heated building array. Ejections appear on low-speed regions and weaker sweeps appear on high-speed regions, both transporting momentum downward. In the bottom heating case, bottom heating induces reduction of the area occupied by the low-speed flow structures and stronger vertical turbulent momentum flux over the reduced area compared with the neutral case. In the conditionally averaged fields, elliptical structures of negative streamwise velocity perturbation and vortical structures similar to hairpin vortices appear and the head part of the vortical structure is vertically expanded when the bottom is heated. High-speed flow structures are more distinct below  $z/H = 3$ , and they tend to descend to the top surfaces of the street canyons or even into the bottom surfaces of the intersections inducing sweeps there. Thus, sweeps are dominant over the street canyons and in the intersections, and they play a dominant role in transporting momentum downward. In the bottom heating case, the magnitude of vertical

turbulent momentum flux increases due to more active mixing of air in and above the building array. In contrast to the intersections, momentum is transported into the street canyons by sweeps appearing at the rooftop height or by spanwise turbulent motions. The spanwise turbulent motions are induced by the sweeps passing through the intersections or by the large secondary circulation strengthened by the bottom heating. The secondary circulation in the BH case induces much stronger updrafts below the low-speed regions and much stronger converging flow below the updrafts compared to the neutral case.

Thermal effects on scalar dispersion in and above the building array were examined. Above the building array, scalar transport events related with updrafts (ejections) are concentrated on the low-speed regions in both cases. Conditionally averaged structures of scalar concentration perturbation are tilted downstream and the bottom heating decreases the spanwise sizes of the coherent structures by inducing spanwise converging flow around them. Both ejection and sweep contribute to the scalar transport at the rooftop height. Ejections pull scalar out of the street canyons and the relevant coherent structures are in a similar shape, especially above the building array. Sweeps put above-canyon air (low in scalar concentration) into the street canyons and the relevant coherent structures are much influenced by the adjacent buildings. Below the rooftop height, the distribution of time-averaged scalar concentration is dependent upon

the turbulence structures appearing above the building array. Below the low-speed regions, scalar concentration (averaged for 1800 s) is high due to the spanwise converging flow induced by the upper structures. This pattern confirms the dominant influence of the upper turbulence structures on scalar dispersion in the urban canopy.

The effects of urban-like surface with a block array on the dry convective boundary layer were investigated using an LES model. A free CBL (FF), a sheared CBL (SF), and a strongly sheared CBL (SSF) over flat surfaces and a sheared CBL over a block array (SB) were simulated. The magnitudes of entrainment heat flux and vertical turbulent momentum flux in the SB case are larger than those in the other cases. Due to the increased surface shear in the SB case, flow in the mixed layer is markedly decelerated and HCRs appear in the mixed layer. In contrast, convection cells occur in the FF case and intermediate structures between cells and rolls occur in the SF case. Large-scale flow structures in the mixed layer also appear in the spectrum density fields of vertical velocity having a spanwise wavelength of  $\sim 2z_i$ . Along with the large-scale secondary circulations, traces of block-induced turbulent eddies are detected in the same spectrum density fields and the profiles of vertical velocity skewness. Decelerated mixed-layer flow in the SB case induces strong wind shear in the entrainment zone and changes the turbulence structures there, resulting in

stronger entrainment heat flux at the inversion height. The magnitude of the entrainment heat flux in the CBLs linearly increases with increasing wind shear in the entrainment zone in all cases, and the indirect effect of blocks on the entrainment heat flux can be explained again by the linear relationship.

Turbulent flow in a densely built-up area of Seoul was simulated using an LES model with urban elevation data. Based on streamwise velocity and column-averaged vertical turbulent momentum flux, three areas of interest were selected: a downstream area of an apartment complex, an area behind high-rise buildings, and a park area. In the downstream area of the apartment complex, all the four quadrant events at  $z = 150$  m become stronger and contribute more to the vertical turbulent momentum transport than the averages in the main domain. Wakes behind apartment buildings are combined to form a large wake, and a large region of strong vertical turbulent momentum flux appears above the wake. Conditionally averaged fields show typical structures of ejections and sweeps. In the area behind the high-rise buildings, fluctuating wakes and vortices appear. Streamwise vortices occur with strong updrafts behind the high-rise buildings and updrafts-induced ejections are dominant in the building-connected and detached wakes. The joint PDF field at  $z = 250$  m shows dominant ejections. Conditionally averaged fields also show strong ejections combined with updrafts along the leeward walls of the high-rise buildings. The high-rise buildings induce

strong downdrafts along their windward walls and the downdrafts transport momentum downward. Mean and instantaneous fields show high turbulent kinetic energy and strong winding flow around the high-rise buildings near the ground surface. The downdrafts induce intermittent flow into nearby streets, resulting in mean flow directed to the street direction. In the park area, the internal boundary layer is developed more vertically than in the upstream area, inducing non-negligible vertical turbulent momentum flux at high levels. As turbulent eddies appear at higher levels, the distribution pattern of ejections and sweeps in the park area becomes complex despite the absence of high-rise buildings.

Turbulent flow in a densely built-up area of Seoul for 0900–1500 LST 31 May 2008 was simulated using the LES model coupled to a mesoscale model (WRF). Time-varying inflow boundary condition (sum of mesoscale wind and recycled turbulent signals) induces quite different turbulence structures depending on time. While strong sweeps and weaker ejections are dominant for 0900–0910 LST, strong ejections and weaker sweeps are dominant for 1450–1500 LST at  $z = 200$  m and the ejections seem to be induced by buildings or building-induced flow structures. The velocity ratio of pedestrian wind speed to ambient wind speed (at  $z = 500$  m) indicates ventilation in the urban area and it is high on broad streets, intersections. The velocity ratio also shows time

dependency but the temporal variation is partially dependent on mesoscale wind environment during this simulation period.

This study investigated turbulent flow and scalar dispersion over several kinds of urban surfaces (from heated street canyon and building array to an actual urban morphology) and the findings in this study would help to understand turbulent flow and scalar dispersion in variably stratified urban environments. To more realistically simulate/predict turbulent flow and scalar dispersion over real urban areas with surface heating, this study will be extended to implement radiation and surface heat exchange processes in the LES model of a coupled LES-mesoscale model.

## References

- Adrian, R. J., C. D. Meinhart, and C. D. Tomkins, 2000: Vortex organization in the outer region of the turbulent boundary layer. *J. Fluid Mech.*, **422**, 1–54.
- Baik, J.-J., and J.-J. Kim, 2002: On the escape of pollutants from urban street canyons. *Atmos. Environ.*, **36**, 527–536.
- Belcher, S. E., 2005: Mixing and transport in urban areas. *Phil. Trans. R. Soc. A*, **363**, 2947–2968.
- Brown, M. J., R. E. Lawson, D. S. DeCroix, and R. L. Lee, 2000: Mean flow and turbulence measurements around a 2-D array of buildings in a wind tunnel. *11th Joint Conference on the Applications of Air Pollution Meteorology with AMS/AWMA*, Long Beach, CA, USA., 35–40.
- Caton, F., R. E. Britter, and S. Dalziel, 2003: Dispersion mechanisms in a street canyon. *Atmos. Environ.*, **37**, 693–702.
- Cheng, H., and I. P. Castro, 2002: Near wall flow over urban-like roughness. *Bound.-Layer Meteor.*, **104**, 229–259.
- Christen, A., E. V. Gorsel, and R. Vogt, 2007: Coherent structures in urban roughness sublayer turbulence. *Int. J. Climatol.*, **27**, 1955–1968.
- \_\_\_\_\_, M. W. Rotach, and R. Vogt, 2009: The budget of turbulent kinetic energy in the urban roughness sublayer. *Bound.-Layer Meteor.*, **131**, 193–222.

- Coceal, O., A. Dobre, and T. G. Thomas, 2007: Unsteady dynamics and organized structures from DNS over an idealized building canopy. *Int. J. Climatol.*, **27**, 1943-1953.
- Conzemius, R. J., and E. Fedorovich, 2006: Dynamics of sheared convective boundary layer entrainment. Part I: Methodological background and large-eddy simulations. *J. Atmos. Sci.*, **63**, 1151–1178.
- Cui, Z., X. M. Cai, and C. J. Baker, 2004: Large-eddy simulation of turbulent flow in a street canyon. *Quart. J. Roy. Meteor. Soc.*, **130**, 1373–1394.
- Deardorff, J. W., 1972: Numerical investigation of neutral and unstable planetary boundary layers. *J. Atmos. Sci.*, **29**, 91–115.
- \_\_\_\_\_, 1980: Stratocumulus-capped mixed layers derived from a three-dimensional model. *Bound.-Layer Meteor.*, **18**, 495–527.
- Dubief Y., and F. Delcayre, 2000: On coherent-vortex identification in turbulence. *J. Turbulence*, **1**, 1-22.
- Dudhia, J., 1989: Numerical study of convection observed during the winter monsoon experiment using a mesoscale two-dimensional model. *J. Atmos. Sci.*, **46**, 3077– 3107.
- Fitzmaurice, L., R. H. Shaw, K. T. Paw U, and E. G. Patton, 2004: Three-dimensional scalar microfront systems in a large-eddy simulation of vegetation canopy flow. *Bound.-Layer Meteor.*, **112**, 107–127.

- Hong, S.-Y., and J.-O. Lim, 2006: The WRF single-moment 6-class microphysics scheme (WSM6). *J. Korean Meteor. Soc.*, **42**, 129–151.
- Inagaki, A., and M. Kanda, 2008: Turbulent flow similarity over an array of cubes in near-neutrally stratified atmospheric flow. *J. Fluid Mech.*, **615**, 101–120.
- \_\_\_\_\_, and \_\_\_\_\_, 2010: Organized structure of active turbulence over an array of cubes within the logarithmic layer of atmospheric flow. *Bound.-Layer Meteor.*, **135**, 209–228.
- \_\_\_\_\_, M. C. L. Castillo, Y. Yamashita, M. Kanda, and H. Takimoto, 2012: Large-eddy simulation of coherent flow structures within a cubical canopy. *Bound.-Layer Meteor.*, **142**, 207–222.
- Kain, J. S., 2004: The Kain-Fritsch convective parameterization: An update. *J. Appl. Meteor.*, **43**, 170–181.
- Kanda, M., R. Moriwaki, and F. Kasamatsu, 2004: Large-eddy simulation of turbulent organized structures within and above explicitly resolved cube arrays. *Bound.-Layer Meteor.*, **112**, 343–368.
- \_\_\_\_\_, 2006: Large-eddy simulations on the effects of surface geometry of building arrays on turbulent organized structures. *Bound.-Layer Meteor.*, **118**, 151–168.
- \_\_\_\_\_, A. Inagaki, T. Miyamoto, M. Gryschka, and S. Raasch, 2013: A new

- aerodynamic parametrization for real urban surfaces. *Bound.-Layer Meteor.*, doi: 10.1007/s10546-013-9818-x
- Kataoka, H., and M. Mizuno, 2002: Numerical flow computation around aeroelastic 3D cylinder using inflow turbulence. *Wind Struct.*, **5**, 379–292.
- Katul, G., G. Kuhn, J. Schieldge, and C.-I Hsieh, 1997: The ejection-sweep character of scalar fluxes in the unstable surface layer. *Bound.-Layer Meteor.*, **83**, 1–26.
- Kim, J.-J., and J.-J. Baik, 1999: A numerical study of thermal effects on flow and pollutant dispersion in urban street canyons. *J. Appl. Meteor.*, **38**, 1249–1261.
- \_\_\_\_\_, and \_\_\_\_\_, 2004: A numerical study of the effects of ambient wind direction on flow and dispersion in urban street canyons using the RNG  $k-\varepsilon$  turbulence model. *Atmos. Environ.*, **38**, 3039-3048.
- Kim, S.-W., and S.-U. Park, 2003: Coherent structures near the surface in a strongly sheared convective boundary layer generated by large-eddy simulation. *Bound.-Layer Meteor.*, **106**, 35–60.
- \_\_\_\_\_, \_\_\_\_\_, and C.-H. Moeng, 2003: Entrainment processes in the convective boundary layer with varying wind shear. *Bound.-Layer Meteor.*, **108**, 221–245.

- Kovar-Pankus, A., L. Moulinneuf, E. Savory, A. Abdelqari, J.-F. Sini, J.-M. Rosant, A. Robins, and N. Toy, 2002: A wind tunnel investigation of the influence of solar-induced wall-heating on the flow regime within a simulated urban street canyon. *Water, Air, Soil Poll.: Focus*, **2**, 555–571.
- Kropfli, R. A., and N. M. Kohn, 1978: Persistent horizontal rolls in the urban mixed layer as revealed by dual-Doppler radar. *J. Appl. Meteor.*, **17**, 669–676.
- Letzel, M. O., 2007: High resolution large-eddy simulation of turbulent flow around buildings with thermal effects. Ph.D. thesis, University of Hannover, Germany, 110 pp.
- \_\_\_\_\_, M. Krane, and S. Raasch, 2008: High resolution urban large-eddy simulation studies from street canyon to neighbourhood scale. *Atmos. Environ.*, **42**, 8770–8784.
- \_\_\_\_\_, C. Helmke, E. Ng, X. An, A. Lai, and S. Raasch, 2012: LES case study on pedestrian level ventilation in two neighbourhoods in Hong Kong. *Meteor. Z.*, **21**, 575–589.
- Li, X.-X., C.-H. Liu, D. Y. C. Leung, and K. M. Lam, 2006: Recent progress in CFD modelling of wind field and pollutant transport in street canyons. *Atmos. Environ.*, **40**, 5640–5658.

- Louka, P., S. E. Belcher, and R. G. Harrison, 2000: Coupling between air flow in streets and the well-developed boundary layer aloft. *Atmos. Environ.*, **34**, 2613-2621.
- \_\_\_\_\_, G. Vachon, J.-F. Sini, P. G. Mestayer, and J.-M. Rosant, 2002: Thermal effects on the airflow in a street canyon-Nantes'99 experimental results and model simulations. *Water, Air, Soil Poll.: Focus*, **2**, 351–364.
- Lund, T. S., X. Wu, and T. S. Squires, 1998: Generation of turbulent inflow data for spatially-developing boundary layer simulations. *J. Comput. Phys.*, **140**, 233–258.
- Macdonald, R. W., R. F. Griffiths, and S. C. Cheah, 1997: Field experiments of dispersion through regular arrays of cubic structures. *Atmos. Environ.*, **31**, 783–795.
- Martilli, A., and J. L. Santiago, 2007: CFD simulation of airflow over a regular array of cubes. Part II: Analysis of spatial average properties. *Bound.-Layer Meteor.*, **122**, 635–654.
- Marusic I, R. Mathis, and N. Hutchins, 2010: Predictive model for wall-bounded turbulent flow. *Science*, **329**, 193–196.
- Meroney, R. N., M. Pavageau, S. Rafailidis, and M. Schatzmann, 1996: Study of line source characteristics for 2-D physical modeling of pollutant

- dispersion in street canyon. *J. Wind Eng. Ind. Aerodyn.*, **62**, 37–56.
- Mlawer, E. J., S. J. Taubman, P. D. Brown, M. J. Iacono, and S. A. Clough, 1997: Radiative transfer for inhomogeneous atmospheres: RRTM, a validated correlated-k model for the longwave. *J. Geophys. Res.*, **102**, 16663–16682.
- Moeng, C.-H., and P. P. Sullivan, 1994: A comparison of shear- and buoyancy-driven planetary boundary layer flows. *J. Atmos. Sci.*, **51**, 999–1022.
- Nakayama, H., T. Takemi, and H. Nagai, 2011: LES analysis of the aerodynamic surface properties for turbulent flows over building arrays with various geometries. *J. Appl. Meteor. Climatol.*, **50**, 1692–1712.
- \_\_\_\_\_, \_\_\_\_\_, and \_\_\_\_\_, 2012: Large-eddy simulation of urban boundary-layer flows by generating turbulent inflows from mesoscale meteorological simulations. *Atmos. Sci. Lett.*, **13**, 180–186.
- Offerle, B., I. Eliasson, C. S. B. Grimmond, and B. Holmer, 2007: Surface heating in relation to air temperature, wind and turbulence in an urban street canyon. *Bound.-Layer Meteor.*, **122**, 273–292.
- Piacsek, S. A., and G. P. Williams, 1970: Conservation properties of convection difference schemes. *J. Comput. Phys.*, **6**, 392–405.
- Raasch, S., and M. Schröter, 2001: PALM—A large-eddy simulation model performing on massively parallel computers. *Meteor. Z.*, **10**, 363–372.

- Raupach, M. R., 1981: Conditional statistics of Reynolds stress in rough-wall and smooth-wall turbulent boundary layers. *J. Fluid Mech.*, **108**, 363–382.
- \_\_\_\_\_, J. J. Finnigan, and Y. Brunet, 1996: Coherent eddies and turbulence in vegetation canopies: The mixing-layer analogy. *Bound.-Layer Meteor.*, **78**, 351–382.
- Reynolds, R. T., P. Hayden, I. P. Castro, and A. G. Robins, 2007: Spanwise variations in nominally two-dimensional rough-wall boundary layers. *Exp. Fluids*, **42**, 311–320.
- Ries, H., and K. H. Schlünzen, 2009: Evaluation of a mesoscale model with different surface parameterizations and vertical resolutions for the Bay of Valencia. *Mon. Wea. Rev.*, **137**, 2646–2661.
- Robinson, S. K., 1991: Coherent motions in the turbulent boundary layer. *Annu. Rev. Fluid Mech.*, **23**, 601–639.
- Rossi, R., D. A. Philips, and G. Iaccarino, 2010: A numerical study of scalar dispersion downstream of a wall-mounted cube using direct simulations and algebraic flux models. *Int. J. Heat Fluid Flow*, **31**, 805–819.
- Rotach, M. W., 1993: Turbulence close to a rough urban surface, Part I: Reynolds stress. *Bound.-Layer Meteor.*, **65**, 1–28.
- \_\_\_\_\_, 1995: Profiles of turbulence statistics in and above an urban street canyon. *Atmos. Environ.*, **29**, 1473–1486.

- Ryu, Y.-H., J.-J. Baik, and S.-H. Lee, 2011: A new single-layer urban canopy model for use in mesoscale atmospheric models. *J. Appl. Meteor. Climatol.*, **50**, 1773–1794.
- Salizzoni, P., M. Marro, L. Souhac, N. Grosjean, and R. J. Perkins, 2011: Turbulent transfer between street canyons and the overlying atmospheric boundary layer. *Bound.-Layer Meteor.*, (in press).
- Shaw, R. H., J. Tavangar, and D. P. Ward, 1983: Structure of the Reynolds stress in a canopy layer. *J. Clim. Appl. Meteor.*, **22**, 1922–1931.
- Shen, S., and M. Y. Leclerc, 1997: Modelling the turbulence structure in the canopy layer. *Agric. For. Meteorol.*, **87**, 3–25.
- Sini, J.-F., S. Anquetin, and P. G. Mestayer, 1996: Pollutant dispersion and thermal effects in urban street canyons. *Atmos. Environ.*, **30**, 2659–2677.
- Skamarock, W. C., and Coauthors, 2008: A description of the Advanced Research WRF version 3. NCAR Tech. Note NCAR/TN-475+STR, 113 pp.
- Stull, R. B., 1988: *An Introduction to Boundary Layer Meteorology*, Kluwer Academic Publishers, 666 pp.
- Sullivan, P. P., C.-H. Moeng, B. Stevens, D. H. Lenschow, and S. D. Mayor, 1998: Structure of the entrainment zone capping the convective

- atmospheric boundary layer. *J. Atmos. Sci.*, **55**, 3042–3064.
- Sykes, R. I., and D. S. Henn, 1989: Large-eddy simulation of turbulent sheared convection. *J. Atmos. Sci.*, **46**, 1106–1118.
- Uehara, K., S. Murakami, S. Oikawa, and S. Wakamatsu, 2000: Wind tunnel experiments on how thermal stratification affects flow in and above urban street canyons. *Atmos. Environ.*, **34**, 1553–1562.
- Walton, A., and A. Y. S. Cheng, 2002: Large-eddy simulation of pollution dispersion in an urban street canyon-Part II: idealised canyon simulation. *Atmos. Environ.*, **36**, 3615–3627.
- Watanabe, T., 2004: Large-eddy simulation of coherent turbulence structures associated with scalar ramps over plant canopies. *Bound.-Layer Meteor.* **112**, 307–341.
- Xie, X., C.-H. Liu, D. Y. C. Leung, and M. K. H. Leung, 2006: Characteristics of air exchange in a street canyon with ground heating. *Atmos. Environ.*, **40**, 6396–6409.
- Xie, Z.-T., and I. P. Castro, 2006: LES and RANS for turbulent flow over arrays of wall-mounted obstacles. *Flow Turbul. Combust.*, **76**, 291–312.

## 초 록

병렬화된 큰에디모사 모형을 이용하여 가열된 도시 표면 위에서의 난류 흐름과 스칼라 분산을 조사하였다. 도시 표면 가열이 난류 흐름과 스칼라 분산에 미치는 영향을 조사하기 위하여 Monin-Obukov 상사성 이론을 바탕으로 하여 건물 벽에서의 열플럭스를 계산하는 방법을 개발하였다.

풍상측 건물 벽, 도로 바닥, 풍하측 건물 벽이 각각 가열되는 협곡 외관비 (canyon aspect ratio)가 1인 이상적인 도로 협곡에서 가열이 난류 흐름 및 분산에 미치는 영향을 조사하였다. 풍하측 건물 벽의 가열은 수축된 주소용돌이 흐름과 소용돌이와 풍하측 건물 벽 사이에서의 휘어진 흐름을 유도하는 반면, 풍상측 건물 벽 또는 도로 바닥의 가열은 도로 협곡의 주소용돌이 흐름을 강화시킨다. 가열되지 않는 경우에는 시어 불안정에 의해 발생한 난류 에디가 협곡 꼭대기에서의 혼합 과정을 주도하며 순간적인 난류 운동량 플럭스와 난류 스칼라 플럭스의 시공간 분포 그림에서 띠 형태의 요동으로 나타난다. 부력에 의해 발생한 난류 에디 역시 시어에 의해 발생한 난류 에디와 마찬가지로 가열되는 모든 경우에서 연직 난류 운동량 그리고 스칼라 플럭스에 기여하며 덩어리

형태의 요동으로 나타난다. 사분원 분석 결과에 따르면, 가열되지 않는 또는 풍상측 건물 벽이 가열되는 경우에는 스윕 (sweep)이 이젝션 (ejection)보다 낮은 빈도로 발생하지만 연직 운동량 플럭스에 더 많이 기여한다. 반대로 도로 바닥 그리고 풍하측 건물 벽이 가열되는 경우에는 이젝션이 스윕과 유사한 빈도로 발생하며 유사한 정도로 연직 운동량 플럭스에 기여한다.

큰에디모사 모형을 이용하여 이상적인 빌딩 배열에서의 난류 흐름과 스칼라 분산을 조사하였다. 가열되지 않는 그리고 바닥이 가열되는 두 경우를 고려하였다. 빌딩 배열 위에서는 저속의 스트리크 (streak) 구조와 이젝션이 운동량을 아래로 수송하는데 중요한 역할을 한다. 바닥면이 가열되는 경우에는 플룸 형태의 구조가 스트리크 구조와 같이 나타나며 저속 지역에서 평균된 연직 난류 운동량 플럭스의 강도가 증가한다. 조건평균한 속도장과 압력장에서 확인된 저속요동 구조와 헤어핀 소용돌이 구조는 바닥면이 가열되는 경우 연직으로 잘 발달하였다. 빌딩 꼭대기 높이에서는 하강하는 고속의 스트리크 구조와 그로 인해 유도되는 스윕이 빌딩 배열 내부로 운동량을 수송하는데 주도적인 역할을 하는 것으로 나타났다. 빌딩 배열 내부에서는 운동량 수송에 중요한 스핀와이즈 방향의 난류 흐름이 스윕에 의해 또는 바닥면 가열에 의해 강화된 큰

이차순환에 유도되는 것으로 나타났다.

큰 규모의 난류 운동은 빌딩 배열의 안팎에서 스칼라의 연직 수송에도 중요한 역할을 하는 것으로 나타났다. 빌딩 배열 위에서는 스칼라 수송 패턴이 이젝션이 우세한 저속의 스트리크 구조에서 주로 나타났다. 바닥면이 가열되는 경우에는 스칼라 농도 요동의 고유 구조 (coherent structure)가 스팬와이즈 방향으로 수렴하는 흐름과 맞물려 나타났다. 빌딩 꼭대기 높이에서는 이젝션과 스윙 모두 스칼라 수송에 중요한 것으로 나타났으며 패턴 각각의 구조는 가열보다는 위치에 따른 차이가 크게 나타났다. 빌딩 배열 내부에서는 저속의 스트리크 구조와 고속의 스트리크 구조 아래에서 각각 스칼라 농도가 높게 그리고 낮게 나타났으며 이는 상층의 난류 고유 구조가 빌딩 배열 내부에서의 스칼라 분산에 주도적인 역할을 함을 보여준다. 이와 같은 패턴은 특히 바닥면이 가열되는 경우에 더 뚜렷하게 나타났다.

블록 배열로 이루어진 도시 구조가 건조한 대류 경계층에 미치는 영향을 큰에디모사 모형을 이용하여 조사하였다. 블록 배열은 지표층에서의 시어를 강화하여 (대류 경계층에 포함되는) 혼합층에서의 평균 흐름을 감속시킨다. 블록 배열이 없는 대류 경계층에서는 대류셀 (convection cell)이 나타나는 반면, 블록 배열 위에서는 대류롤 (convective

roll) 구조가 나타나며 스펙트럼장에서 대류롤의 스펙와이즈 방향 간격은 대류 경계층 높이의 2배로 나타났다. 블록 배열을 포함하는 대류 경계층에서는 혼합층 평균 흐름이 감소되어 대류 경계층의 꼭대기에 위치한 유입 지역에서의 연직 시어가 증가하였으며, 그로 인해 난류 활동이 강화되어 유입 열플럭스의 크기가 증가하였다.

큰에디모사 모형을 이용하여 서울 도심 지역에서의 난류 흐름을 조사하였다. 칼럼 평균한 난류 플럭스 크기를 비교하여 아파트 풍하측, 고층빌딩 풍하측, 그리고 공원 세 관심 지역을 선택하였다. 아파트 풍하측에서는 큰 웨이크와 웨이크 상층에서 난류 플럭스가 강한 지역이 나타났다. 고층빌딩 풍하측에서는 요동치는 웨이크와 소용돌이 구조가 빌딩 꼭대기 높이에서 이젝션 패턴으로 나타났고, 고층빌딩 전면의 하강기류가 도로 바닥 부근에서는 강한 난류 그리고 테헤란로와 같은 큰 도로를 따르는 흐름을 유도하는 것으로 나타났다. 공원 지역에서는 높은 빌딩이 존재하지 않더라도 풍상측의 난류 활동에 의해 어느 정도의 난류 활동이 유지되는 것으로 나타났다.

중규모 모형과 결합된 큰에디모사 모형을 이용하여 서울 도심 지역에서의 2008년 5월 31일 오전 9시부터 오후 3시까지의 난류 흐름을 수치모사하고 분석하였다. 시간에 따라 변화하는 중규모 바람은 서울 도심

지역의 난류 구조를 변화시켰다. 오전 9시 경에는 상층 흐름에 의해 스윙이  
그리고 오후 3시 경에는 주로 빌딩에 의해 유도된 이젝션이 뚜렷하게  
나타났다. 도심 지역에서의 환기 (ventilation)을 나타내는 인도에서의  
풍속과 상층 500 m에서의 풍속의 비를 계산하였으며 그 비는 넓은  
도로에서 높게 그리고 빌딩이 밀집한 지역에서는 낮게 나타났다. 풍속의 비  
결과에서 공간적인 패턴이 뚜렷하게 나타나는 반면, 중규모 바람의 영향은  
다소 복잡하게 나타났다.

**주요어:** 난류 흐름, 스칼라 분산, 가열, 큰에디모사, 고유 구조, 이젝션, 스윙,  
대류 경계층, 중규모 바람

**학 번:** 2007-30101